ERUPTIVE PROCESSES OF MAFIC ARC VOLCANOES – SUBAERIAL AND SUBMARINE PERSPECTIVES

by

NICHOLAS D. DEARDORFF

A DISSERTATION

Presented to the Department of Geological Sciences
and the Graduate School of the University of Oregon
in partial fulfillment of the requirements
for the degree of
Doctor of Philosophy

September 2011

DISSERTATION APPROVAL PAGE

Student: Nicholas D. Deardorff

Title: Eruptive Processes of Mafic Arc Volcanoes – Subaerial and Submarine Perspectives

This dissertation has been accepted and approved in partial fulfillment of the requirements for the Doctor of Philosophy degree in the Department of Geological Sciences by:

Dr. Katharine V. Cashman	Chair
Dr. Joshua J. Roering	Member
Dr. Paul J. Wallace	Member
Dr. Patricia F. McDowell	Outside Member
Dr. William W. Chadwick	Outside Member

and

Kimberly Andrews Espy	Vice President for Research & Innovation/Dean of the Graduate School

Original approval signatures are on file with the University of Oregon Graduate School.

Degree awarded September 2011

DISSERTATION ABSTRACT

Nicholas D. Deardorff

Doctor of Philosophy

Department of Geological Sciences

September 2011

Title: Eruptive Processes of Mafic Arc Volcanoes – Subaerial and Submarine Perspectives

Approved: _____
Dr. Katharine V. Cashman

Mafic arc volcanoes have eruption styles that range from explosive to effusive. In a broad sense, eruption style is controlled by the rate of magma supply to the vent. In this dissertation I examine relationships between eruption rate and style in two separate studies: (1) an investigation of ongoing activity at NW Rota-1, a submarine volcano in the Mariana arc, and (2) a morphologic study of the Collier Cone lava flow field in the Central Oregon Cascades.

The eruptions of NW Rota-1 range from effusive to moderately explosive; eruptions are effusive when mass eruption rate (MER) is low and explosive when MER increases. The explosivity of submarine eruptions is suppressed by seawater because of increased hydrostatic pressure, rapid cooling, and the high viscosity of water relative to air (which limits expansion). The combination of seawater and relatively low MERs limit pyroclast deposition to within meters to tens of meters of the vent. In fact, many pyroclasts fall back into the vent and are recycled. Evidence for recycling includes microcrystalline inclusions within erupted pyroclasts and elevated Cl and Na

concentrations in matrix glass. Enrichment of Cl and Na suggests that seawater assimilation provides a geochemical signature of recycling. Recycling is limited to low MER explosive eruptions and is not observed in either effusive lava or deposits from high MER explosions.

Direct observations of eruptions allow measurements of eruption rate. However, it is more challenging to estimate MERs of eruptions that were not observed. To address this problem, I develop and test methods of constraining the eruption rate (and duration) of the c. 1600 year old Collier Cone lava flow using the flow morphology. To quantify flow morphology I combine field observations with GIS analysis of Lidar-derived digital topography. Channel dimensions constrain emplacement rates; dominant wavelengths and amplitudes of surface folds constrain spatial and temporal changes in flow rheology.

Three videos of eruption activity accompany this dissertation as supplemental files.

This dissertation includes both previously published and unpublished co-authored material.

CURRICULUM VITAE

NAME OF AUTHOR: Nicholas D. Deardorff

GRADUATE AND UNDERGRADUATE SCHOOLS ATTENDED:

University of Oregon, Eugene
University of Miami, Coral Gables, FL

DEGREES AWARDED:

Doctor of Philosophy, Geological Sciences, 2011, University of Oregon
Bachelor of Science, Marine Science and Geology, 2003, University of Miami

AREAS OF SPECIAL INTEREST:

Physical Volcanology
Submarine Volcanism

PROFESSIONAL EXPERIENCE:

Teaching assistant, Department of Geological Sciences, University of Oregon, Eugene, 2005-2011

GRANTS, AWARDS, AND HONORS:

Graduate Teaching Fellowship, Psychology, 2005 to present

Staples Fellowship, Geological Sciences, University of Oregon, 2008

Good Citizen Award, Dept. of Geological Science, University of Oregon

Staples Fellowship, Dept. of Geological Science, University of Oregon

Member of Sigma Xi National Science Honor Society, 2002-2003

Member of Golden Key International Honor Society, 2001-2003

PUBLICATIONS:

Deardorff, N., Cashman, K., Chadwick, W. (2011) Observations of eruptive plume and pyroclastic deposits from submarine explosive eruptions at NW Rota-1, Mariana Arc, J. Volcanol. Geotherm. Res. 202: 47-59. doi:10.1016/j.jvolgeores.2011.01.003

Deardorff, N., Cashman, K. (2010) Post-eruptive magma mixing: recycling in volcanic vents. Eos, AGU. 91(52), Fall Meet. Suppl., Abstract V43C-2391.

Deardorff, N., Cashman, K., Chadwick, W. (2009) Anomalous Chlorine Concentrations Indicate Recycling of Submarine Pyroclasts at NW Rota-1, Mariana Arc. Eos, AGU 90 (52) Fall Meet. Suppl., Abstract V44B-04.

Deardorff, N., Cashman, K. (2009) Morphologic Measurements on an Intermediate Composition Blocky Lava Flow Field in Central Oregon Using High Resolution (~1m) Lidar DEMs- a Technical Approach, Geological Society of America *Abstracts with Programs*. 41(7): 432.

Chadwick, Jr., W. W., Cashman, K. V., Embley, R. W., Matsumoto, H., Dziak, R. P., de Ronde, C. E. J., Lau, T. K., Deardorff, N. D., Merle, S. G. (2008) Direct video and hydrophone observations of submarine explosive eruptions at NW Rota-1 volcano, Mariana arc, J. Geophys. Res. 113(B08S10): 1-23, doi:10.1029/2007JB005215.

Deardorff, N., Cashman, K. (2008) Morphologic Measurements on an Intermediate Composition Blocky Lava Flow Field in Central Oregon Using High Resolution (~1m) Lidar Dems, IAVCEI 2008 *Conference Programme* (Abstract) p. 49.

Deardorff, N., Cashman, K., Chadwick, W., Embley, R. (2007) Plume and Pyroclast Dynamics Observed During a Submarine Explosive Eruption at NW Rota-1, Mariana Arc, Eos Trans. AGU. 88(52), Fall Meet. Suppl., Abstract V24B-07.

Deardorff, N., Emerson, L., Soule, A., Belien, I., Gottesfeld, E., Johnson, E., Mckay, D., Wisely, B. (2007) Implementation of Ground-Based Lidar, Total Station, and GPS in an Advanced Geophysical Study of Basaltic Cinder Cone Morphology, Four Craters Volcanic Field, Oregon, Geological Society of America *Abstracts with Programs*. 39 (6): 123.

Deardorff, N., Cashman, K., Chadwick, W., Embley, R. (2006) Submarine Explosive Eruptions: Physical Volcanology of NW Rota-1, Marianas, Eos Trans. AGU, 87(52), Fall Meet. Suppl., Abstract V23B-0609.

ACKNOWLEDGEMENTS

There are many people who have contributed to the completion of my graduate student career and the work involved in this dissertation. First, and foremost, I would like to thank my advisor, Kathy Cashman, who contributed the lioness's share of my graduate education and has groomed me into the scientist that I am today. Thank you for your patience and guidance, the knowledge that you have passed on, your creative input, and your generosity in funding and in life. Thank you for your enthusiasm for my research and for science in general; it is infectious. And thank you for two spectacular research projects; I could not have asked for more interesting research topics.

I would like to thank everyone who helped me with field research. During multiple field seasons in the Oregon Cascades I was assisted by Dan Ruscitto, Daniele Mckay, Natalia Deligne, Kathy Cashman, Paul Wallace, my wife Jenna, and the fantastic mules who hauled all of our gear and samples in and out of camp. Very special thanks go out to Natalia Deligne for tramping over blocky lava for days in the hot sun and being a perfect 152cm scale. I would also like to thank Bill Chadwick and Bob Embley for including me on three research cruises to the Marianas [funded by the NOAA Vents and Ocean Exploration Programs and the National Science Foundation (award OCE-0751776)]. These cruises have not only provided me with a dissertation, but have undoubtedly shaped my future career, as I am clearly hooked on submarine volcanism. In addition, I need to thank all members of the science crews and the ship crews for the research vessels *Thompson*, *Melville*, and *Kilo Moana*. I must also thank the crew from Woods Hole Oceanographic Institute who operated the remotely operated vehicle *Jason*,

without which, the collection of video and samples within this dissertation would not have been possible.

Thank you to an incredible group of graduate students who have made my time in Eugene memorable beyond belief. Thank you for the camping and Sunriver trips, thank you for the Friday afternoons at Rennies (particularly Stephanie Weaver and Ben Mackey), and thank you for the crazy mustache, French, Easter brunch, thumb wrestling, ugly sweater, and Halloween parties. I would like to thank all of the Cashman lab members who allowed me to discuss research ideas and concepts with a colleague, made me laugh and enjoy the day-to-day work that is grad school, and who have helped me feel like less of an idiot at times. Thank you to all members, past and present, of the Glenwood breakfast club for accompanying me for delicious Friday morning breakfasts and for your contributions to conversations that almost never revolved around geology.

Thank you to the UO Geology Department in general for having such a wonderful blend of prestige, intellect, kindness, and generosity. I cannot imagine a more open and fun department producing such an assortment of interesting, high quality research. A special thank you to the office staff (Vicki, Dave, and Shari) for deadline reminders, and for your kindness, support and sports talk.

I would like to thank my family for all of their support over the many years I have been a student, regardless of how far from home I may be and how infrequently I am able to visit. Finally, I would like to thank my beautiful wife, Jenna, for agreeing (while on the Collier lava flows) to marry me. I sincerely appreciate your understanding, support, and patience with me as I worked long hours and continuously slip into geology-speak when talking to friends and colleagues.

This dissertation is dedicated to all the young boys and girls in Indiana who have never seen a mountain, or a volcano, or an ocean. See the world, it might just change yours.

TABLE OF CONTENTS

Chapter Page

Chapter Page

Chapter Page

LIST OF FIGURES

Figure Page

Figure Page

LIST OF TABLES

Table Page

CHAPTER I

INTRODUCTION

Most volcanoes are located along the boundaries of tectonic plates at divergent (mid-ocean ridges) and convergent (i.e. subduction zones) margins. Mid-ocean ridges are dominated by effusive, mafic volcanism created by upwelling magma from the spreading center. Subduction zone volcanism is driven by the release of volatiles from the down-going plate as pressure and temperatures increase. Hydrous fluids released into the overlying mantle reduce the melting temperature and produce melt that rises through the mantle and overlying crust to erupt. Because of the complicated pathways of magma ascent, arcs produce a large range of eruption compositions (basalt to rhyolite) and eruption styles that range from effusive to explosive.

Many explosive volcanoes in the subaerial environment occur within arc settings. When thinking of explosive volcanoes most people think of large silicic stratovolcanoes with plinian style eruptions, such as Mt. St. Helens or Montserrat. However, most explosive volcanism occurs as mafic cinder cone eruptions, making cinder cones the most abundant subaerial volcanic feature (Valentine and Gregg, 2008). Mafic eruptions are, however, not exclusively explosive, but are often accompanied by effusive activity that can produce large lava flow fields. Although small and not usually life threatening, the frequency of mafic eruptions produces significant hazards to local populations, particularly through fire, floods, and property damage.

Volcanic arcs are not exclusive to the subaerial environment. In fact, >30% of known arc volcanoes are submarine (Wright, 1999). Therefore, it is not unreasonable to think the submarine environment may also be dominated by both effusive and explosive mafic volcanism. Island arc volcanoes are often composite volcanoes, similar to subaerial stratovolcanoes. However, island arc volcanoes represent the small visible fraction of the volcanic arc after it has breached the ocean surface. Before subaerial exposure each volcano must build its edifice vertically several kilometers from the seafloor. The submarine portion of the volcanic edifice is constructed by a combination of effusive and explosive volcanism and (often simultaneous) mass wasting events.

This dissertation focuses on mafic volcanism in arc settings and includes analysis of both a submarine explosive volcanic vent (**Chapters II, III**) and a subaerial lava flow field (**Chapter IV**). In the submarine setting, I quantify the observable features of effusive and explosive eruptions at the submarine volcano, NW Rota-1, Mariana arc (**Chapter II**) and compare submarine explosive episodes to their subaerial counterparts. In **Chapter IV**, I discuss the emplacement conditions of an intermediate composition subaerial lava flow as preserved in flow morphology, which I analyze using GIS-based techniques.

The explosivity of submarine volcanic eruptions depends on the magmatic volatile content, magma-water interactions, and the depth below sea level (bsl). Elevated confining hydrostatic pressures and inevitable magma-water interactions in the submarine environment raise questions about the depths at which explosive eruptions are possible and what pyroclast morphologies are expected. Observations of active submarine

volcanism provide new insight into the dynamics of submarine eruptions and allow us to test existing theories. **Chapter II** focuses on the submarine strombolian eruptions observed at NW Rota-1 over one week in 2006 and discusses the effect of seawater on the eruption dynamics, eruption velocities, pyroclast deposition and clast morphologies. Eruption dynamics are characterized from video collected by a remotely operated vehicle (ROV) and by geochemical and textural analysis of samples. Many pyroclasts were observed to fall back into the erupting vent, providing the opportunity for recycling and re-ejection. **Chapter III** focuses on pyroclast recycling, discussing textural and geochemical evidence and a proposed model for the recycling process. The timescales required for recycling are explored using crystallization experiments and modeling of chlorine diffusion in the matrix glass. Recycling efficiency is evaluated for the full range of eruption rates and styles at NW Rota-1, including observed (for the 2006-2010 time period) and inferred (from hydrophone data) activity.

Explosive mafic eruptions are often accompanied by the effusion of lava flows, particularly when gas and magma segregate because rising bubbles ascend more rapidly than surrounding melt (Pioli et al., 2008). One such lava flow field emerged from a cinder cone on the north flank of North Sister, Oregon. Collier Cone is a Holocene cinder cone that produced both violent strombolian explosions and lava flows. Since this eruption was not observed during emplacement, the lava rheology (e.g. lava viscosity, flow velocity, yield strength, etc.) and emplacement conditions (effusion rate and eruption duration) are unknown. Understanding emplacement conditions is critical for volcanic hazard assessment in the central Oregon Cascades. My work shows that the flow field includes

four geochemically distinct units that were mapped using a combination of field work and high resolution (~1m) Light Detection and Ranging (Lidar) data. The lava flows were analyzed using a GIS-based technique that extracts simple morphologic measurements from the Lidar-generated DEM (**Chapter IV**). These measurements were then used to estimate the effusion rates and emplacement times for this prehistoric lava flow. The complex lava flow field produced by Collier Cone suggests an eruption duration of at least weeks to months. Flow surface morphologies were analyzed using profiles from the Lidar data and Fourier transform signal processing.

I am the first author of all work presented in this dissertation, although the main body chapters (II, III, IV) were co-authored. I was responsible for all sample analyses, other than bulk chemical analyses, which were performed by the Washington State University GeoAnalytical Lab, Pullman, WA. Chapter II is published (2011) in the *Journal of Volcanology and Geothermal Research* and was coauthored by Kathy Cashman (advisor) and Bill Chadwick (Hatfield Marine Science Center, Oregon State University, Newport, OR); each contributed to the editorial process and conceptual research. Chapter III is in preparation for submission to the journal of *Geology*. Coauthors include Kathy Cashman, Bill Chadwick and Bob Dziak (Hatfield Marine Science Center). Kathy Cashman contributed to the editorial process. Bill Chadwick contributed figure 3.3, which shows hydrophone data collected and processed by himself and Bob Dziak. Chapter IV is co-authored with my advisor, Kathy Cashman who shared editorial responsibilities. This chapter is in preparation for submission to *Bulletin of*

Volcanology. Chapter V is a summary of the ideas and concepts of this dissertation and is my work.

CHAPTER II

OBSERVATIONS OF ERUPTIVE PLUMES AND PYROCLASTIC DEPOSITS FROM SUBMARINE EXPLOSIVE ERUPTIONS AT NW ROTA-1, MARIANA ARC

This chapter was published April 2011 in volume 202, issue 1-2, of the *Journal of Volcanology and Geothermal Research*. Coauthors include Kathy Cashman and Bill Chadwick who assisted with the editorial process. I performed all sample analyses and was the primary author.

1.0. Introduction

Terrestrial arc volcanism has been observed and recorded for centuries, but far less is known about eruptions in the submarine environment. Recent exploration of submarine volcanic arcs shows that volcanic activity in these environments is diverse in both time and space (e.g., Fiske et al., 2001; Yuasa and Kano, 2003; Embley et al., 2007). Particularly exciting has been the discovery of volcanically active seamounts along the Mariana arc, with extensive hydrothermal fields (Baker et al., 2008), molten sulfur flows and ponds (Butterfield et al., 2007), and explosive eruptive activity (Chadwick et al., 2008; Embley et al., 2006; Walker et al., 2008).

We focus here on observations of activity at NW Rota-1 volcano made during a single week in April 2006. During this time period, volcanic activity evolved from diffuse gas venting and lava effusion to energetic magmatic eruptions that emitted S-rich

plumes, CO_2 bubbles, and scoria of basaltic andesite composition. In the subaerial environment this activity would be described as strombolian, that is, continuous degassing and mild, intermittent explosions caused by gas accumulation and release within the shallow conduit (Harris and Ripepe, 2007a,b; Parfitt, 2004; Vergniolle and Mangan, 2000). The observations made at NW Rota-1 in 2004 and 2006 were the first ever of submarine explosive eruptions.

The activity at NW Rota-1 in 2006 allows us to extend existing models of submarine explosive activity (e.g., Kokelaar, 1986; Head and Wilson, 2003) through video observations and sample analysis. Specifically, we use close-range remotely operated vehicle (ROV) video to analyze and interpret the dynamics of small submarine eruption plumes. We link observed changes in eruption dynamics to shallow conduit processes using both physical and chemical characteristics of the pyroclasts. We demonstrate that seawater strongly suppresses eruption plumes, which affects both transport and deposition of larger clasts, and causes rapid clast cooling and fragmentation ('quench granulation'). Additionally, we show that quenched material that falls back into the vent can be identified in thin section and may comprise a substantial proportion (≤15%) of the magma erupted during any one event.

2.0. Activity at NW Rota-1 in April 2006

NW Rota-1 is a basaltic andesite volcano with a summit at 517 m below sea level (bsl) located about 100 km north of Guam (Fig. 2.1). Research cruises using ROVs have documented volcanic activity at NW Rota-1 in 2004, 2005, 2006, 2009, and 2010 (e.g.,

Embley et al., 2006; Chadwick et al., 2008; Walker et al., 2008; Chadwick et al., 2009). This paper focuses on activity witnessed in 2006 when the active vent, Brimstone, was located on the steep southern slope of the volcano, about 30 m south of and below the summit. The timing of the 2006 cruise – apparently shortly after a substantial collapse of the vent area – allowed us to witness the vent re-establish activity.

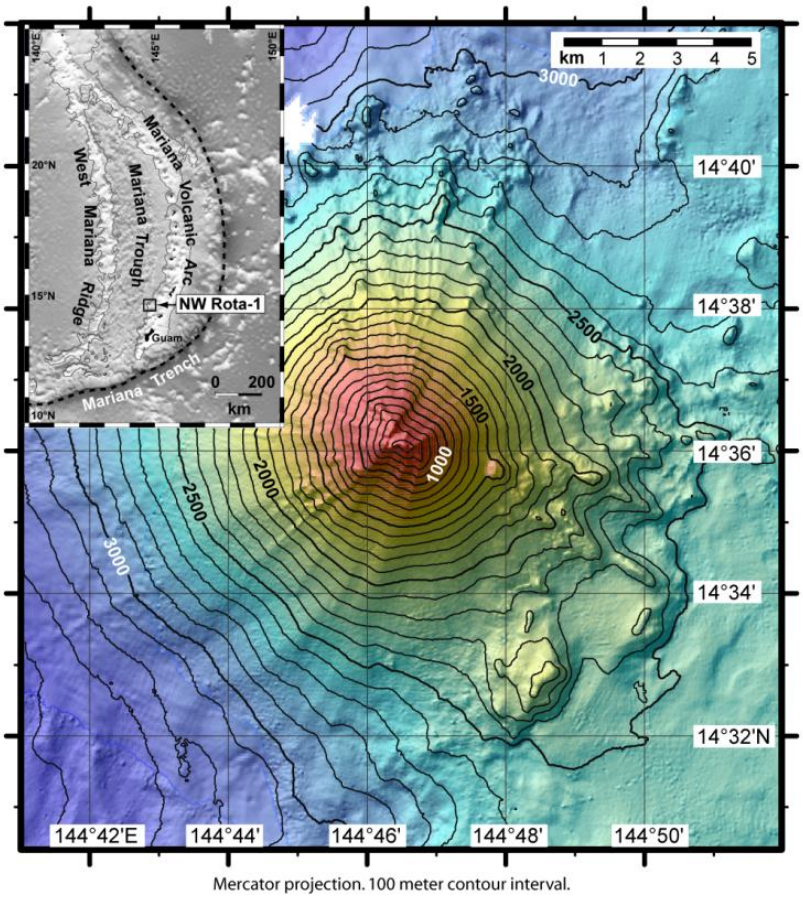

Fig. 2.1. Bathymetric map of NW Rota-1 volcano, Mariana arc with 100 m contours. Inset shows location of NW Rota-1, ~100 km north of Guam. Modified from Chadwick et al., 2008.

Detailed descriptions of eruptive activity, vent locations and acoustic data collected during the April 2006 cruise are presented in Chadwick et al. (2008) and are summarized here (Table 1). During one week of observations, activity evolved from effusive to explosive as the mass eruption rate (MER) increased from <5 m^3/hr to ~100 m^3/hr (Fig. 2.2). Explosive activity also evolved from intermittent and infrequent gas bursts from multiple vent locations to nearly continuous emissions from a well-focused vent. Fluidal pyroclast morphologies and incandescence at the vent during the most vigorous eruptive phases indicate the presence of high temperature magma within the vent. Additionally, a magmatic source for the gas is suggested by observations of strong degassing of SO_2 and CO_2 (Resing et al., 2007; Lupton et al., 2008). Chadwick et al. (2008) concluded that magmatic H_2O was the primary driver of the explosive activity, and that seawater contributions to explosivity were minimal. Here we explore the eruption dynamics in more detail, with the specific goal of linking direct observations to the physical and chemical characteristics of the erupted pyroclasts.

Table 1 - Description of changes in the vent, pyroclasts, eruption rate and eruption plume with time.

Date	Dive #	Vent description and activity observed	Range in block sizes at vent	Estimated MER m^3/hr	Sample description	Plume description	Interpretation
4/22/06	J2-186	N/A (could not appproach due to poor visibility)	N/A	N/A	N/A	White cloud enveloping volcano, zero visibility. Top of cloud/plume ~470m b.s.l.	ROV arrived just after large volcanic event, possibly large sector collapse removing part of the cone.
4/23/06	J2-187	Initially a rubble heap abutting a steep shear wall, with some intermittent lava extrusion and moderate degassing	4 - 13 cm	~1 - 5 m^3/hr	Scoop J2-187-31; collected 40m downslope (south) of Brimstone Pit.	No plume present. Intermittent passive degassing in vent area.	Partial collapse of cone left shear wall and rubble pile where vent used to be. Passive degassing and some lava extrusion indicates vent still active.
4/24/06	J2-188	Intermittent low level bursting from two unfocused vent locations	<1 - 12 cm	~1 - 5 m^3/hr	Scoop J2-188-4; collected at site of future activity. Passive degassing through loose pyroclasts during collection.	Dispersed discontinuous plume fed by intermittent low level activity.	Vent was choked with loose pyroclastics. Degassing increased but was widely dispersed.
4/25/06	J2-189	Range in activity from low level bursting to strong explosive bursts from 2-3 vents through loose pyroclastic deposits.	1.5 - 22 cm	5 - 100 m^3/hr	Scoop sample J2-189-1: collected at actively building cone ~2-3m across of loose pyroclastic deposits. Juvenile and altered clasts present.	Semi-continuous white and occasionally sulfurous billowing plume from multiple locations.	Activity and degassing increased. Rising volatiles began to coalesce creating gas pockets able to push aside pyroclastic deposits. Conduit began to clear it's throat with overpressured bursts.
4/27/06	J2-191	Intermittent low to mid level explosive bursting with sporadic discrete large bursts from multiple locations along scarp wall.	2 - 67 cm	10 - 100 m^3/hr	J2-191-7 'volunteers' erupted onto ROV, mostly clasts ~1-5cm with larger clasts up to 30cm. Mostly juveniles with some altered clasts. Larger clasts show evidence of ductility and some have entrained lithics/altered.	Intermittent plume from 2-3 m section of scarp wall. Sporadic degassing in multiple locations in areas.	Gas flux is starting to increase within the conduit, leading to an increase in eruption intensity and block sizes; establishing the upper conduit and vent.
4/27/06 4/28/06	J2-192	Well focused vent, ~0.2-1m in diameter, producing cyclical activity of sustained explosive bursts for several minutes followed by 10s of seconds of quiescence and quenched lava cap.	3 - 99 cm	10 - 100 m^3/hr	N/A	Sustained and nearly continuous white billowing plume, occasionally turning yellow with sulfur.	Focused vent allows cyclical activity due to volatile separation in conduit. Quiescence created by gaps between volatile clusters allowing rapid invasion of seawater and quenching lava in top of conduit. Pressure must build up to breach quenched lava cap.

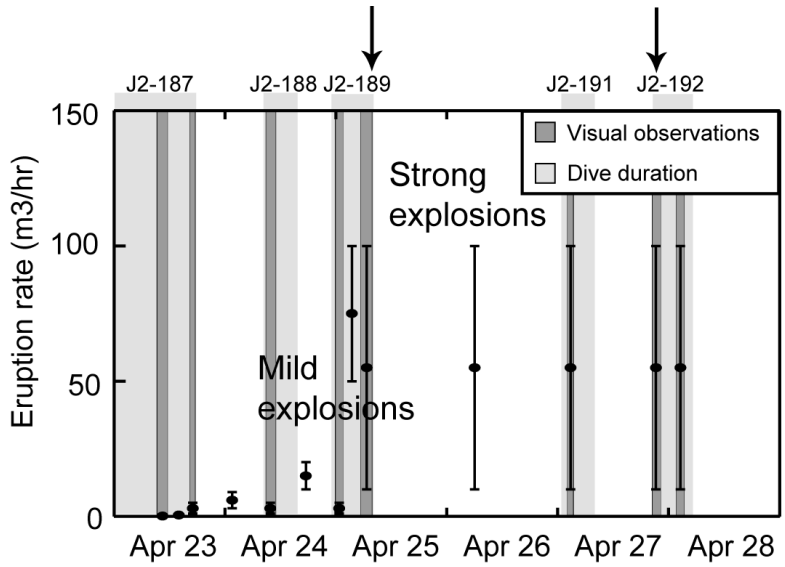

Fig. 2.2. Eruption rate vs. time (black dots) during week of observations in 2006. Data points show increase in activity with time from mild explosions, early, to strong explosions later in the week. Eruption rates were calculated by estimating the volume of the erupted deposits during and between each visit to the vent. Light grey areas indicate bottom time for each ROV dive. Dark grey bars indicate time spent making visual observations at Brimstone. Arrows indicate times of plume measurements during dives J2-189 and J2-192. Image modified from and eruption rates calculated by Chadwick et al., 2008.

3.0. Methods

This study focuses on a combination of video analysis and examination of tephra samples collected using the *Jason II* ROV during dives J2-189, J2-191, and J2-192. Video observations of the eruptions at NW Rota-1 were used to quantify plume behavior and infer eruption dynamics. To link eruption dynamics to conduit processes, we analyzed tephra samples that were collected from the active vent during both early and late eruptive periods (Table 1).

3.1. Video analysis

To analyze the eruptive plumes we made frame-by-frame measurements from *Jason* dive video. Dual parallel-mounted lasers spaced 10 cm apart provided a scale for image analysis. Eruption sequences were chosen for analysis based on water clarity, vehicle stability, camera angle, and the presence of the 10 cm laser scale. Analyzed video sequences included both early plumes erupted through loose pyroclastic deposits (end of dive J2-189) and late focused plumes (dive J2-192). Plume height was measured every 1-5 frames (0.04-0.18 sec) from the point at which the plume was first visible above the vent until the plume left the field of view, the view was obstructed, or plume motion had ceased (Fig. 2.3). Plume rise velocity and acceleration were calculated using the measured plume height and known time between frames. Measurements from dives J2-189 and J2-192 differ in that during the early eruptions (J2-189), plumes formed as discrete bursts, while during later eruptions plumes (J2-192) were nearly continuous, fed by intermittent (rejuvenating) bursts. Continuous degassing prevented accurate measurements of the onset of individual plumes during the most energetic late stage eruptions.

Clasts were measured from still frames within ~1-2 m from the vent and ≤0.5 m from the 10 cm laser scale. The clast visibility was dependent on camera resolution, ROV distance from the vent, and water clarity. Therefore, the minimum clast size measurable is estimated at ~1 cm.

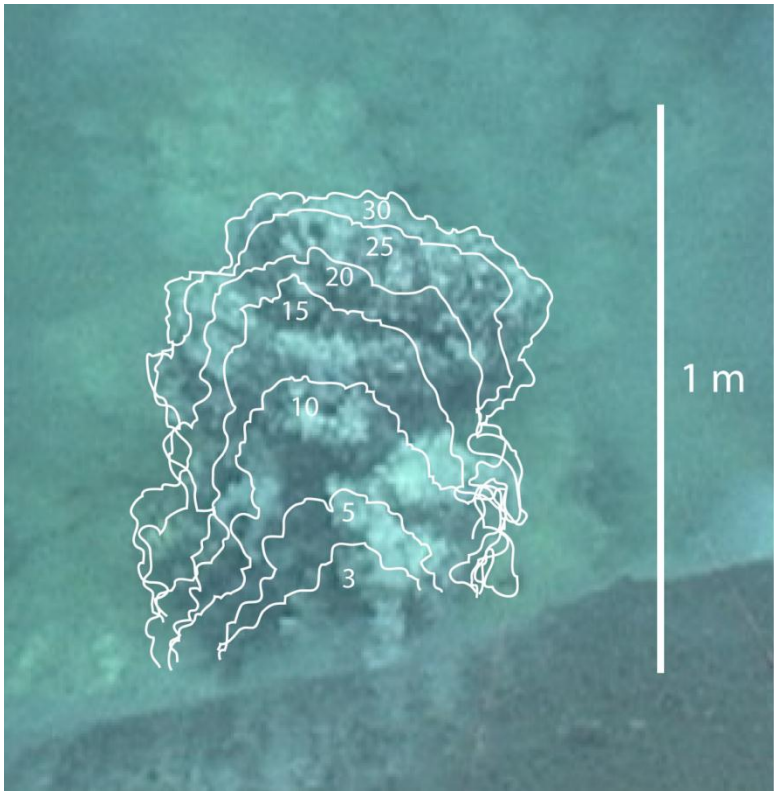

Fig. 2.3. Early plume erupting through loose pyroclastic deposits (dive J2-189). Overlays indicate digitized plume extents used to measure plume heights and calculate rise velocity. Numbers represent the frame grabs used to digitize plume extents. 30 frames equal ~1s of time.

3.2. Sample analysis

Individual rock samples were collected using the *Jason* manipulators, while bulk (scoop) pyroclastic samples were collected in canvas sacks. Clasts in sample J2-191-7 were deposited onto the undercarriage of the ROV while the cameras were observing the vent.

Grain size distributions of the scoop samples were measured by dry sieving at 1ϕ intervals from -4 to 3ϕ. Clasts >0ϕ (1 mm) were separated into components defined by the degree of surface alteration, the amount of fresh glass, and clast surface

morphologies. Densities of 12 clasts (2-10 cm diameter) from dive J2-189 and 50 clasts from dive J2-191 were measured by weighing the clasts in air and in water. For measurements in water, the clasts were first coated in liquid cellulose acetate, which formed a thin film upon drying that prevented water from penetrating interior vesicles. Vesicularities were calculated using a bulk rock density of 2700 kg/m^3 measured by He pycnometry of a powdered sample.

Thin sections of 15 representative clasts were analyzed for both microscopic features and geochemistry. Full thin section scans permitted evaluation of sample heterogeneity, phenocryst populations, and the contribution of large vesicles to the overall vesicularity. Details of groundmass textures were provided by back-scattered electron (BSE) images obtained using a FEI Quanta 200 SEM at the University of Oregon. Analysis of BSE images allowed us to quantify observed variations in plagioclase microlite textures both within and between samples.

Microprobe analyses were completed on groundmass glass in four samples using a Cameca SX100 microprobe at the University of Oregon run at 12 keV, with a beam current of 20 nA and beam size of 2.5 um. The elements analyzed include major and minor elements (Na_2O, K_2O, Al_2O_3, MgO, FeO, TiO_2, MnO, P_2O_5, SiO_2, CaO, and NiO) and the volatile elements F, S and Cl. Total count times for each beam location was >200 seconds. The most volatile elements (i.e. Na) were analyzed first to limit loss.

4.0. Results

Key features of the April 2006 activity at NW Rota-1 include concurrent changes in vent structure and eruptive vigor (Chadwick et al., 2008). Here we examine this relationship through both qualitative and quantitative observations of plumes generated by the evolving eruptive activity. We then turn to the pyroclastic material produced by the eruptions to evaluate its origin (are they magmatic or resulting from seawater interaction?). We end by examining textural features contained within the pyroclasts that shed new light on processes active within the NW Rota-1 vent.

4.1. Eruption plumes

4.1.1. Plume observations

Volcanic plumes emitted from NW Rota-1 are composed primarily of condensed sulfur particles, formed as magmatic SO_2 mixes with the surrounding seawater (Butterfield et al., 2007). Non-condensable gases, such as CO_2, emerge as bubbles that either precede and/or accompany individual eruptive bursts.

Early phases of explosive activity (dives J2-188, J2-189) consisted of intermittent activity over an area of ~5 x 12 m at the base of a steep scarp. Activity was dominated by billowing plumes, with basal diameters of ~1-2 m, produced by passive magmatic degassing and small intermittent gas bursts (basal diameters 10-20 cm) from a more localized source that entrained loose pyroclastic material from the seafloor. The entrained clasts typically fell out of the plume after an initial rapid rise to ≤50 cm, but the cloudy sulfur-rich plume rose much higher (generally <50 m). At the end of dive J2-189, ground

shaking and deformation of the seafloor preceded each small explosion. Individual plumes produced by these explosions had basal diameters of 0.5 to >1 m, and emissions from multiple locations defined a vent region of 3-5 m in diameter. When multiple gas pulses emerged in quick succession from a single location, a compound plume formed (Video 1; Fig. 2.4). These compound plumes rose higher than plumes formed by single bursts before slowing and depositing entrained material (typically within ≤3 m of the vent).

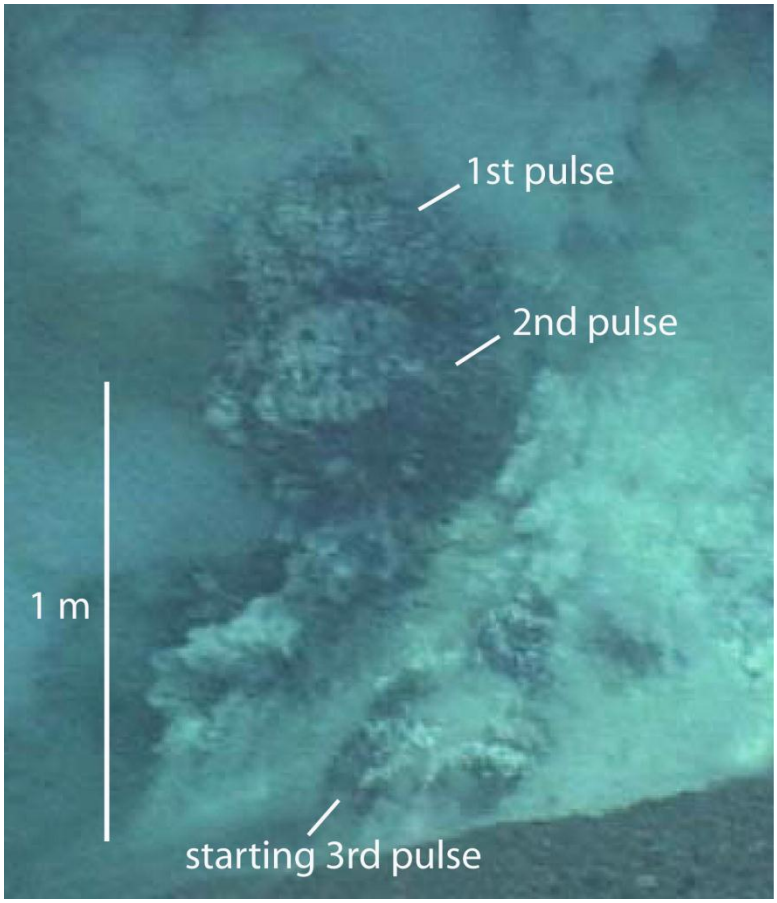

Fig. 2.4. Compound plume resulting from sequential gas bursts following similar pathway. Early in the week of observations erupting bursts occurred over a diffuse area of loose pyroclastic deposits. Plume bursts are dark in color due to entrained material.

Video 1 (viewed as online supplementary material) shows early eruptive activity consisting of momentum-driven jets that transition to buoyant plumes. The transition to buoyant plumes is visible as particle fallout and change in plume color from dark to light. Multiple gas pulses following a similar pathway in quick succession are present in the second sequence. Ground deformation (shaking) is visible before pulses emerge. Scale is provided by red laser dots 10 cm apart.

Late eruptive activity (dives J2-191 and J2-192) was characterized by nearly continuous gas emissions from a focused vent. By dive J2-191, the vent had constructed an elongate scoria cone >5 m high of juvenile clasts ≥5-10 cm in diameter. Discrete explosions carried clasts (coarse ash, lapilli, and bombs) to ≤1.5 m above the vent before they were deposited on the growing cone. One such discrete eruption deposited sample J2-191-7 onto the ROV undercarriage. The vent had shifted by the final dive (J2-192) to form a new crater located ~0.5-1 m from the sulfur wall that formed the northern limit of the vent region (Fig. 2.5). Activity was modulated by the periodic formation and disruption of a quenched lava cap within the active vent (Video 2). During the most vigorous activity, flashes of incandescence were observed at the vent opening, indicating temperatures >700ºC. Strong explosions lasting 2-6 minutes were followed by 30-40 seconds of passive degassing (Chadwick et al., 2008); resulting plumes widened gradually as they rose above the vent and shut off abruptly when activity ceased. This nearly continuous activity produced coherent plumes that rose <100 m above the seafloor before dispersing down-current. Evidence of seawater interaction during this phase

included the rapid cycles of flashing and condensation at the plume margin and secondary fragmentation of erupted pyroclasts (Sec. 5.1.2).

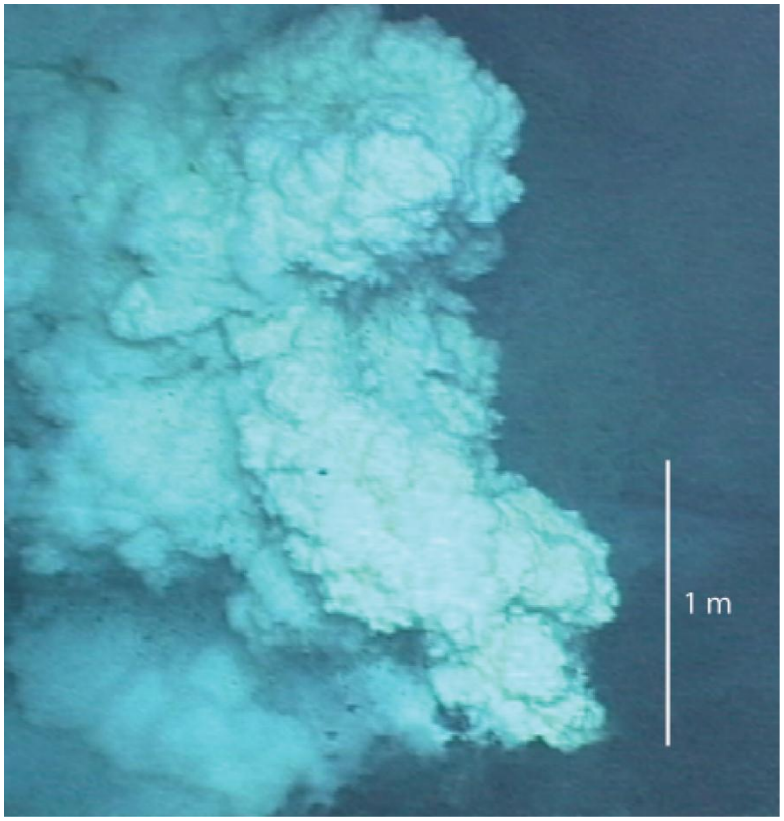

Fig. 2.5. Late stage activity from focused vent <1 m in diameter (dive J2-192) composed of loosely consolidated clasts, mostly centimeters to 10s of centimeters in diameter. Buoyancy-driven plume is white, having already dropped out most erupted pyroclasts. Slight current is present pushing plume to left.

Video 2 (viewed as online supplementary material) shows late stage activity consisting of buoyant plumes from nearly continuous gas emissions, emitted from a focused vent. Eruptions are cyclical with a few minutes of activity followed by a shorter period of repose, during which seawater engulfs the vent and quenches remaining lava. The onset of renewed activity ruptures the lava cap, depositing large cap fragments on the vent rim. Red laser dots are 10 cm apart.

4.1.2. Plume dynamics

Differences in plume behavior between early unfocused and late focused eruptions can be measured by tracking changes in plume height with time (Fig. 2.6a). Early plumes (solid lines) ascended rapidly for the first 0.5-1.25 m (~0.5-0.8 s) before slowing. In contrast, late plumes (dashed lines) ascended steadily throughout the entire period of observation. Above ~1.25 m, early (J2-189) and late (J2-192) plumes ascended at similar rates. We interpret the initial rapid-rise phase of the early plumes to indicate momentum-driven exit from the vent. In contrast, the steady rise of the late plumes (and later phase of the early plumes) indicates buoyancy-driven (convective) plume rise. We note that a few bursts produced by later eruptions also appeared to have initiated with a short momentum-driven phase (Video 3), but could not be measured because of a lack of either camera stability or the 10 cm laser scale. However, these momentum-driven phases were rare and the late phase activity was dominantly buoyancy-driven over the observation intervals.

Video 3 (viewed as online supplementary material) shows evidence for infrequent momentum-driven pulses during late stage activity. During the first sequence pressure builds up in vent due to heavy deposition within the vent and an unstable vent opening, followed by momentum-driven pulses to clear the vent. Also note the amount of ejected material that falls back into the vent. In the second sequence there is an abrupt onset of activity from a period of repose that quickly ruptures the lava cap, resulting in brief momentum-driven pulses. Both examples of momentum-driven phases during late stage activity return to buoyantly rising plumes within just a few minutes.

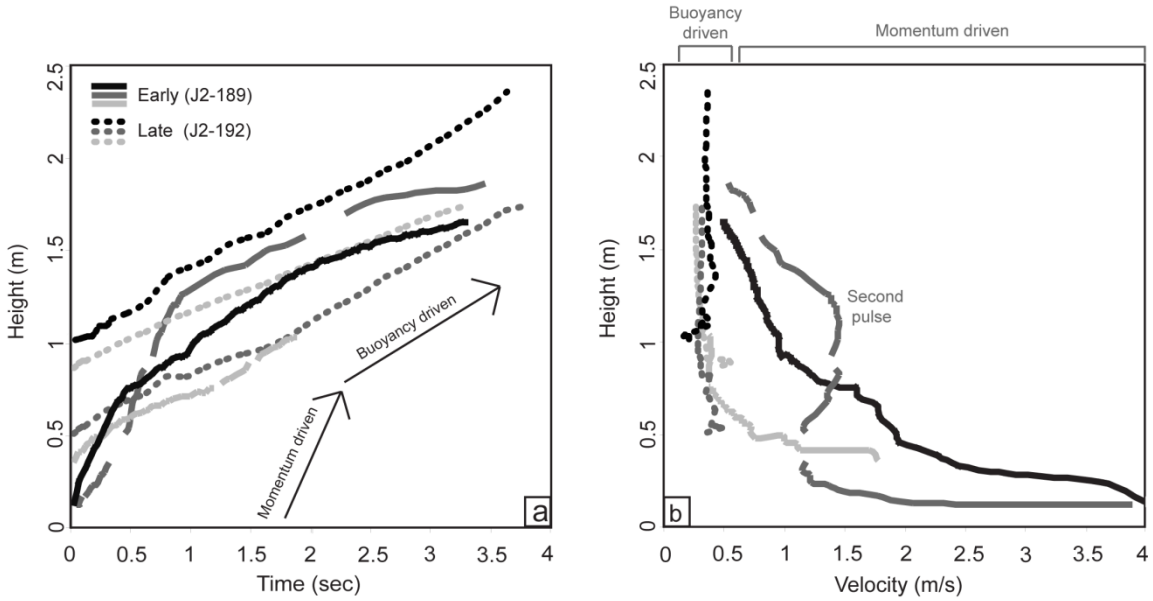

Fig. 2.6. (a) Changes in height of the eruptive plume over time, demonstrating differences in initial plume ascent between early and late eruptive activity. Early plumes (solid lines) have an initial rapid rise, momentum-driven phase, and transitioned into buoyancy-driven plumes within <1.5 m above the vent. Late plumes (dashed lines) were buoyancy-driven from their initiation without a momentum-driven phase. (b) Plot of height vs rise velocity, demonstrating the rapid deceleration of early momentum-driven plumes. The late buoyancy-driven plumes initiate and rise at nearly a constant velocity <0.5 m/s. The odd bulge of the dark grey early plume is due to a second eruptive burst producing a slight acceleration and creating the compound plume from Fig. 2.4.

The difference between momentum-driven and buoyancy-driven plume components is highlighted by a comparison of plume velocities (Fig. 2.6b). Early plumes have initial velocities of ~1-4 m/s, which decreased to 0.5-1 m/s within ~1 m of the vent. The rapid deceleration correlates with deposition of dense clasts, evidenced by a change in plume color from dark to light, and an increase in width of the rising plume (Video 1). In contrast, late focused plumes have ejection velocities of <0.6 m/s and quickly achieve a steady ascent rate of ~0.35 m/s. Although plume initiations of dive J2-192 were difficult to measure due to poor visibility at the vent, the data provide no indication of

rapid deceleration between 0.5 and 1.25 m above the vent, where the early plumes (J2-189) were still decelerating. This relationship between plume dynamics and eruption vigor is addressed in section 5.1.

4.1.3. Clast transport

To relate the plume dynamics to the load of dense particles that they carried, we also examined clast deposition from the rising plumes. Most early plumes reached heights of <0.5-1 m before entrained clasts (coarse ash, lapilli and bombs) were observed to fall from the plume margins, although the largest early explosions transported clasts to >3 m above the vent. Some coarse ash entrained within the core of the plume rose beyond the ROV's field of view to be dispersed more widely. Although ash deposition was observed (infrequently) 10s of meters from the vent, this represented a very small fraction of the ejected material. Rarely, the erupting bursts were so choked with clasts the plume collapsed, producing, in one instance, a dilute density flow. Elutriation of fine particles from such density currents may contribute to the general lack of fine particles in the vent area (Sec. 4.2.1).

The mean size of clasts entrained within the eruptive plumes increased with increasing eruptive vigor (Table 1), as did the amount of juvenile material that was ejected (Sec. 4.2.1). The largest blocks formed from quenched lava caps that were simply pushed up and over the scoria cone rim. Bomb-sized ejecta were tossed <1-2 m above the vent, while most coarse ash and lapilli were transported to ≤4 m. Some ash and lapilli were carried to greater heights (>6 m). In contrast to the early eruptions, most of the

ejected material was initially carried within the plume interior and individual pyroclasts were not visible until they fell out of the plume. Many ejected clasts fragmented on contact with seawater, releasing swarms of gas bubbles (dominantly CO_2; Lupton et al., 2008). Large ejecta were deposited close to the vent to construct the scoria cone. Some of these clasts fell directly back into the vent.

4.2. Pyroclast samples

Pyroclast samples were analyzed for physical properties (grain size, density, and components), crystallinity, and glass composition. Scoop samples provided an integrated record of clast deposition over an undetermined time period, and therefore were used only for analysis of physical properties. Detailed textural and chemical analyses of pyroclasts from sample J2-191-7 provided a snapshot of vent processes occurring during the more vigorous phase of activity.

4.2.1. Grain size, componentry and density

All scoop samples are fines-depleted, well sorted ($0.93 \leq \sigma_\phi \leq 1.39$), and have median grain sizes (Md_ϕ) of ~-1ϕ (2-4 mm). Three primary components were identified in clasts greater than 1 mm (0ϕ): tan juvenile clasts, dark juvenile clasts and altered clasts (Fig. 2.7a-f; Table 2). Juvenile clasts are distinguished from altered clasts by the presence of fresh glass on most surfaces. Little to no fresh glass is present on the surface of altered clasts and phenocryst surfaces are also commonly altered. Yellow or metallic grey sulfur spheres comprise ≤1 weight % of every scoop sample (Fig.2.7k). Elemental sulfur is also

Table 2 - Description of sample components, with vesicularity and density

Component	Color	Morphology	Alteration	Vesicularity range: mean	Density kg/m3 range: mean	Vesicle morphology
Tan juvenile	light to dark brown	smooth, fluidal surfaces with vesicular features- Figs. 2.7a,b	Not present	11.9-38.3%: 32.5%	1666-2172: 1830	Bimodal population: small, equant bubbles and large, irregular vesicles
Dark juvenile	dark brown to black	equant and blocky with multiple fractured faces- Figs. 2.7c,d	Little to moderate surface alteration, often on only one or two faces	25.3-38.1%: 33.7%	1671-2379: 1824	Mostly small, equant bubbles with some large, coalesced spheroidal vesicles
Altered	dark grey to white, often with white or yellow coatings	Similar shapes as both juv. components, but rough surfaces- Figs. 2.7e,f	Heavy alteration on all surfaces, very little glass visible. Glass still present in interior	16.0-38.3%: 29.4%	1666-2267: 1906	Similar to both juvenile vesicle morphologies.
Sulfur	yellow to metallic grey	Mostly spheres and ameboid globules. Less common, fluidly stretched S with entrained ash, or filling vesicles of clasts- Figs. 2.7i,j,k	Uncommon, spheres can alter to grey stony surfaces, with yellow interiors	N/A	N/A	N/A

found filling existing vesicles in basaltic clasts (Fig. 2.7i), or as fluidly stretched sulfur with entrained ash and lapilli (Fig. 2.7j; Table 3). Elemental sulfur and sulphate (measured in excess from Brimstone vent fluids) are products of the reaction between degassed SO_2 with seawater (Butterfield et al., 2009).

Table 3 - Changes in component percentages with sample number.

Sample	% Tan juvenile	% Dark juvenile	% Altered	% Sulfur	MER m^3/hr	Collection
J2-188-4	2.63	38.72	57.65	1.01	~5	scoop
J2-189-1	32.29	27.93	39.78	<0.01	5-100	scoop
J2-191-7	40.59	26.48	32.93	0	10-100	volunteers

Clasts collected from the more vigorous late-stage activity (J2-191-7) have diameters of 1-30 cm. Coarse lapilli are more heterogeneous than those observed in scoop samples, with some juvenile clasts having both tan and dark components. Two large bombs contain small (1-5 cm) highly altered lithic clasts that are either contained within (Fig. 2.7h) or embedded in the surface (Fig. 2.7g) of the clasts.

Most analyzed clasts have densities of ~1700-2100 kg/m^3, with a maximum of 2400 kg/m^3. A slight decrease in average clast density appears to accompany the observed increase in eruption rate, with a shift from ~1950 kg/m^3 in sample J2-189-1 to ~1830 kg/m^3 in J2-191-7. The equivalent vesicularity range is 12 to 38%, with a mean of 31.4% (Fig. 2.8). The density difference between dives may reflect the degree of alteration, as juvenile clasts (both tan and dark) have modal densities of ~1800 kg/m^3 while altered clasts have a modal density of 1950 kg/m^3. The very slight density differences between juvenile and altered clasts, and their similar surface morphologies,

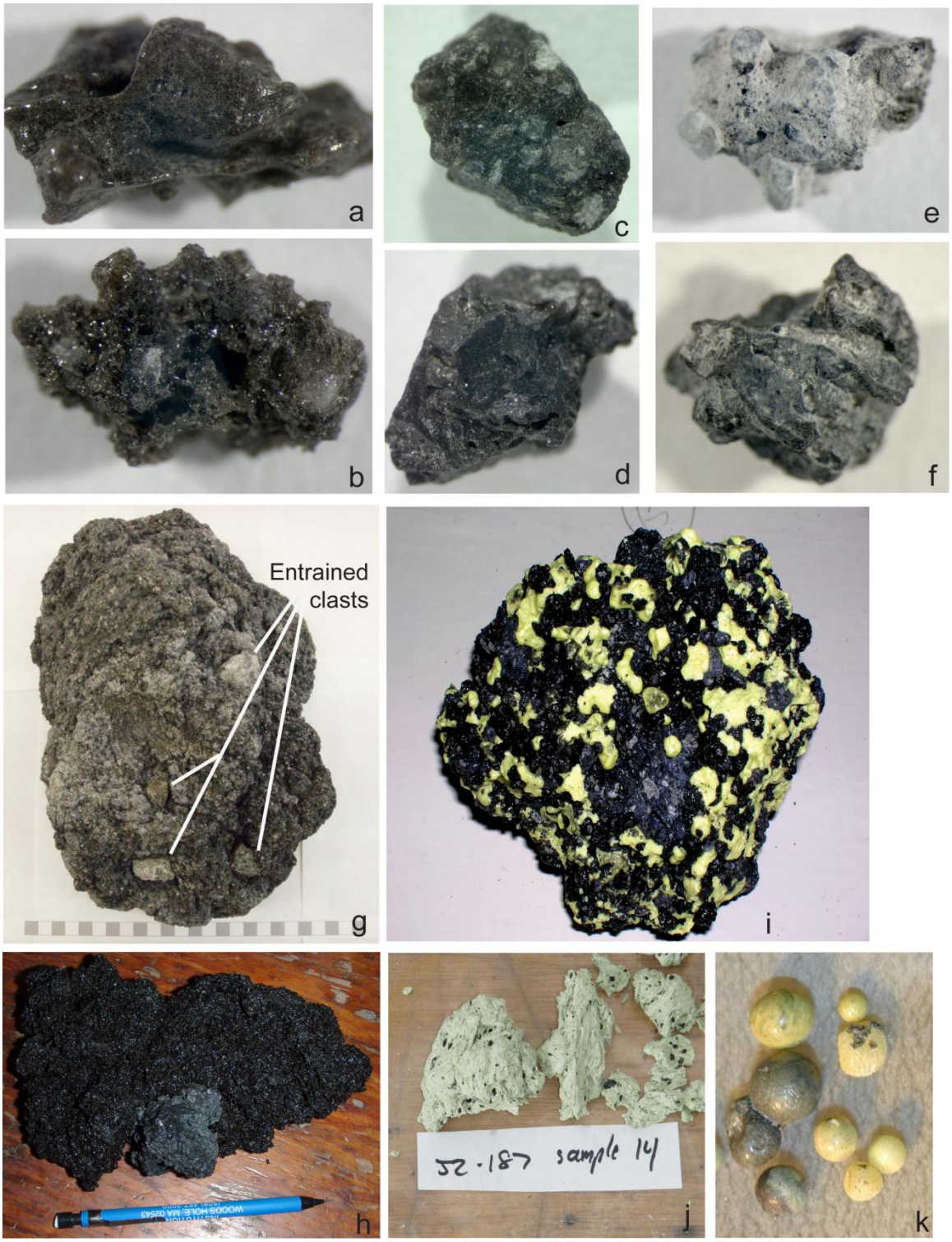
a
c
e
b
d
f
Entrained
clasts
g
i
h
52-187 sample 14
j
k

Fig. 2.7. Photos (a-f) are of clasts ~4 mm in diameter collected from the active vent during dive J2-189. (a) Tan juvenile clast with smooth fluidal surfaces. (b) Tan juvenile clast with jagged vesicular morphology. (c, d) Dark juvenile clasts with blocky, equant shapes. (e, f) Heavily altered clasts; (e) shows evidence of once smooth fluidal surfaces, similar to (a). (g) Mildly altered clast with entrained heavily altered lithics. (h) Glassy, vesicular clast with jagged surfaces similar to (b) and entrained altered clast. (i) Glassy, moderately vesicular clast with external vesicles filled with elemental sulfur. (j) Elemental sulfur that has been thoroughly stretched and folded, like taffy, with entrained ash and lapilli tephra. (k) Elemental sulfur balls; colors include yellow, grey and greenish-grey.

suggests that they are similar in origin and differ only in age (proportional to the degree of alteration).

A comparison of clasts from early and late eruptions shows that changes in eruptive activity were accompanied by changes in components with time (that is, with increasing average eruption rate). Specifically, a comparison of bulk pyroclasts collected from dives J2-188 and J2-189 shows that the proportion of tan juvenile clasts increased from 3 to 32%. Although the sampling technique was not the same, this trend appears to continue through later events, with 41% tan clasts in sample J2-191-7. An accompanying decrease in average clast density (Fig. 2.8) records the increase in juvenile components and corresponding decrease in altered components.

4.2.2. Juvenile clast textures

Juvenile clasts (tan and dark) have similar phenocryst contents, with plagioclase dominant and lesser olivine and clinopyroxene. Tan clasts have large irregular vesicles in a glassy, vesicle-poor matrix (Figs. 2.9a,b). Dark juvenile clasts have numerous small, spherical vesicles within the interior, while vesicles in the dense glassy rims are often

deformed parallel to the outer edge of the clast, indicating post-eruptive inflation of clast interiors (Fig. 2.9c).

Examination of thin sections show that microcrystalline inclusions occur in most tan glassy clasts from dive J2-191 (Fig. 2.9), where inclusions typically comprise 3-20% of the thin section area. Inclusions are rounded to highly deformed, often cored by phenocrysts of plagioclase, pyroxene, or olivine (Figs. 2.9a,b), and medium to dark brown in color (Fig. 2.9e). The boundaries between microcrystalline and glassy regions may be either diffuse (Figs. 2.9f,g) or sharp (Fig. 2.9b). Some microcrystalline-rich areas display fluidal groundmass textures, defined by crystal alignment (Fig. 2.9g) or wispy microlite tails (Fig. 2.9f). In BSE images, the inclusions can be identified by variations in the abundance, shape and composition of groundmass crystals. The matrix of tan clasts has microlites that are less numerous and more euhedral than in the inclusions, where plagioclase microlites often have dendritic overgrowths or swallowtail extensions. Augite and olivine microlites are abundant within the microcrystalline inclusions (Fig. 2.10), as are tiny Fe-sulfides (white dots in Fig. 2.10a).

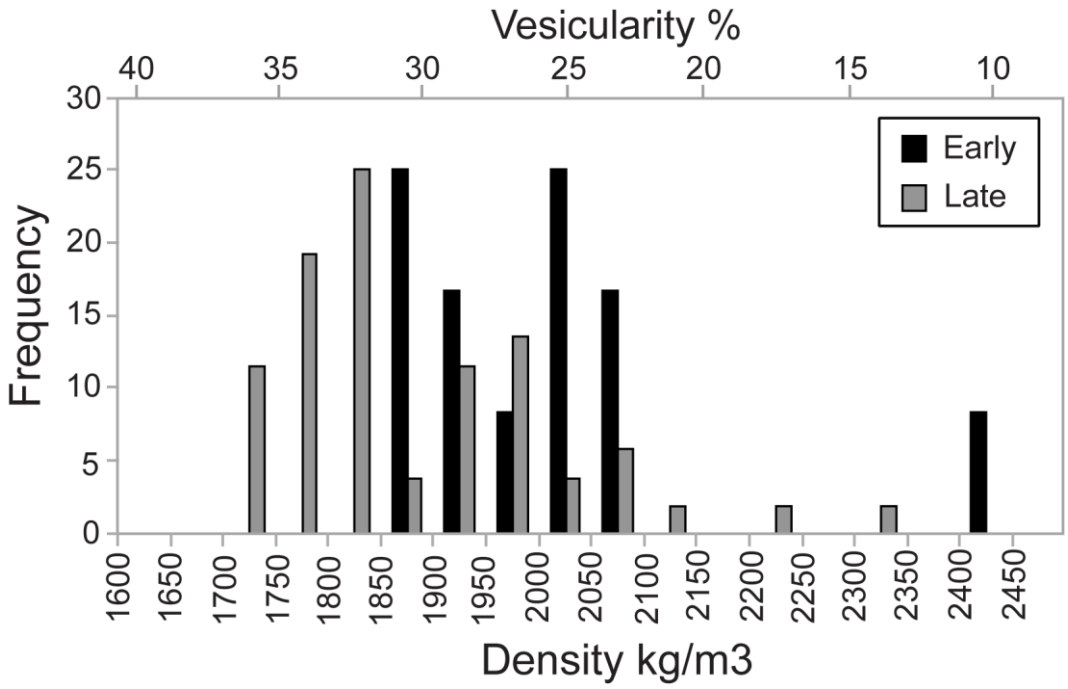

Fig. 2.8. Normalized density frequency distribution from clasts collected during dives J2-189 and J2-191. There is a slight decrease in densities from early to late eruptive activity, correlating with an increase in eruption rate. Vesicularities were calculated from the densities using an averaged vesicle-free rock density of 2700 kg/m^3.

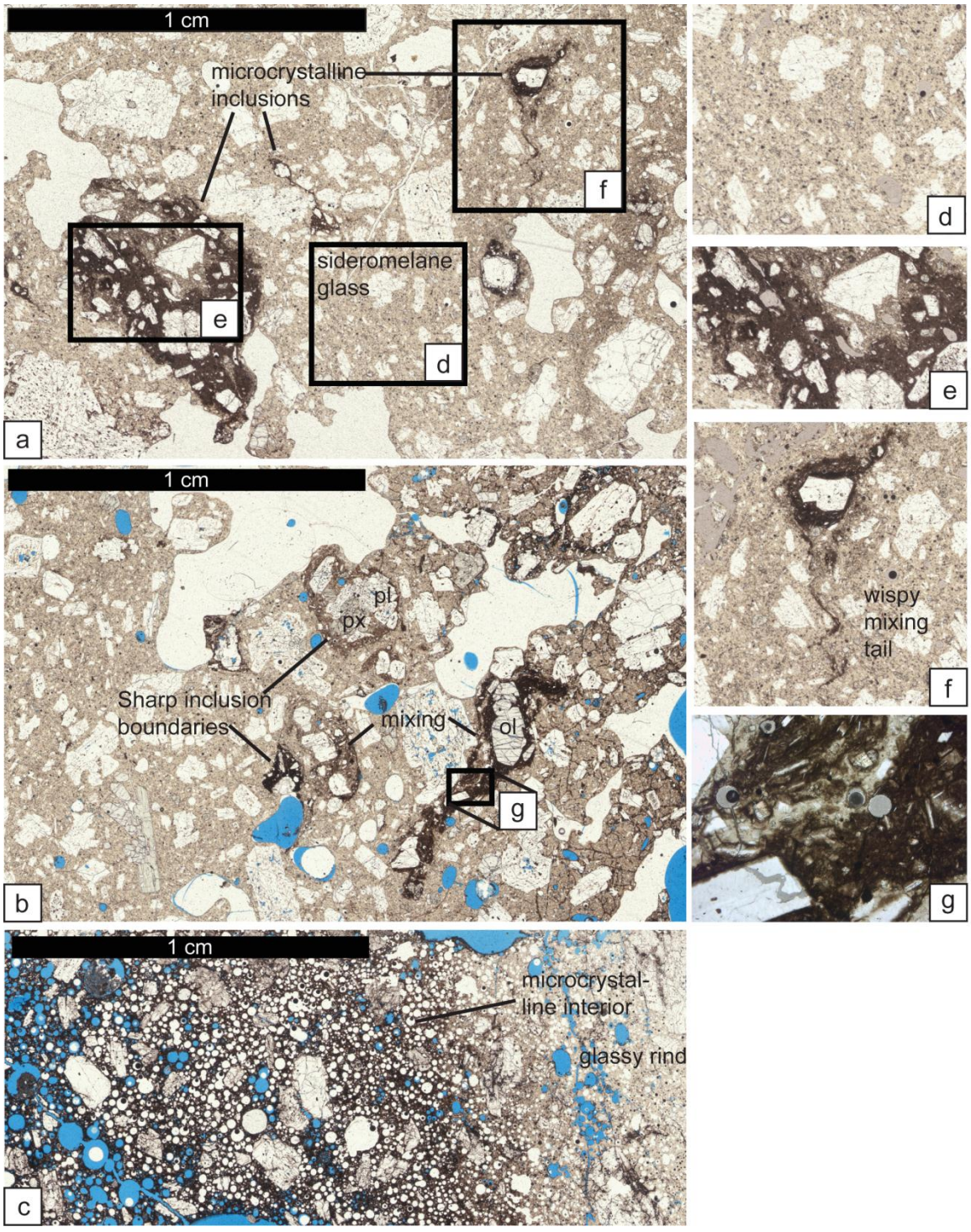
1 cm
microcrystalline inclusions
f
e
sideromelane glass
d
a
d
e
wispy mixing tail
f
1 cm
pl
px
Sharp inclusion boundaries
mixing
ol
g
b
g
1 cm
microcrystal-line interior
glassy rind
c

Fig. 2.9. Thin section scans of juvenile clasts. Tan juvenile clasts (a, b) have large, irregular coalesced vesicles, very few small vesicles within the matrix. Dark juvenile clasts (c) have numerous small, spherical vesicles, particularly the interior. Matrix glass in the tan juvenile clasts is generally microlite-poor (d), but there are areas of high microlite crystallization (e, f, g). These microcrystalline inclusions can have sharp, distinct boundaries (b, e) or diffuse boundaries, occasionally with wispy mixing zones (b, f, g). Microcrystalline inclusions are often cored with plagioclase (pl), olivine (ol) or clinopyroxene (px) phenocrysts (b, e, f). Dark juvenile clasts have tan microlite-poor quench rims and microcrystalline-rich interiors, suggesting post-emplacement crystallization.

To compare groundmass crystal content among the various constituents we measured the abundance of plagioclase microlites and microphenocrysts (<10,000 um^2) in representative glassy and microcrystalline areas; two tan and two dark clasts. The microlite crystallinities of the matrix of the tan clasts and the tan glassy rims of the dark clasts are similar at 6-14%; we assume that this range represents the pre- and syn-eruptive extent of groundmass crystallization. In contrast, both the interiors of the dark clasts and the microcrystalline inclusions in the tan clasts have crystallinities of 17-25%.

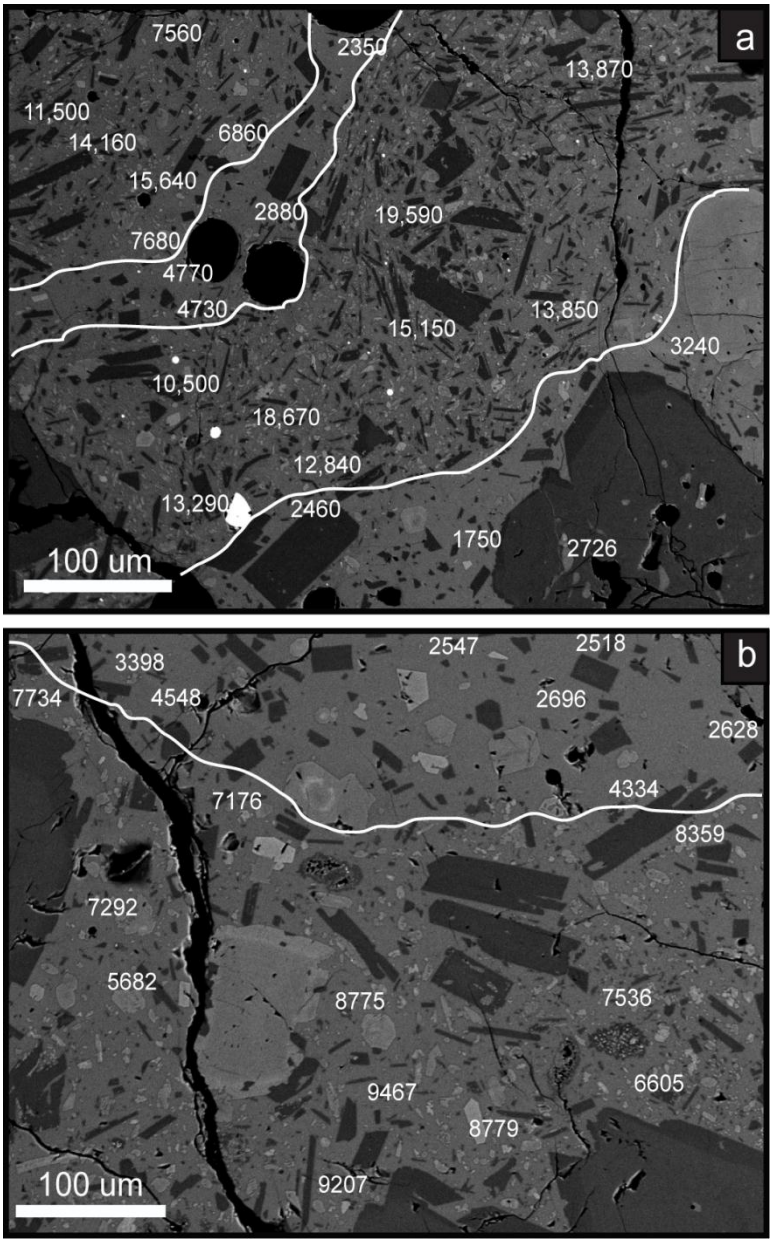

Fig. 2.10. BSE images of microcrystalline inclusions within tan juvenile clasts. Inclusions are microlite-rich and can display mixing textures (a) or sharp, distinct boundaries (b) with surrounding matrix glass. White lines indicate boundaries between inclusions and surrounding matrix. The numbers represent chlorine microprobe values in ppm. The highest Cl values were found within inclusion mixing zones. There are rapid changes in Cl within <100 um along the inclusion-matrix boundaries.

4.2.3. Glass compositions

Matrix glass compositions were analyzed in four tan clasts with microcrystalline inclusions to compare glasses of variable microlite content. Microcrystalline areas have lower MgO and CaO, higher Cl and Na_2O, and a wider range of SiO_2 and FeO than the microlite-poor matrix in the same clast. There is no apparent difference in K_2O, Al_2O_3, TiO_2, MnO, P_2O_5 and NiO between microcrystalline glass and surrounding matrix. The most striking result of our microprobe work comes from measurement of Cl content of the groundmass glass in clasts that contain microcrystalline inclusions. High crystallinity inclusions have a much larger range in Cl than enclosing microlite-poor glass (Fig. 2.11). Areas of low crystallinity (open diamonds) have Cl contents of 1700-3500 ppm, while areas of intermediate and high microcrystallinity (closed diamonds) range from <1000 to 22,000 ppm (2.2 wt%) Cl. Na values, although more scattered than Cl, are also elevated in microcrystalline inclusions relative to the surrounding matrix (Fig. 2.12), although measured values fall both slightly below and slightly above matrix glass values.

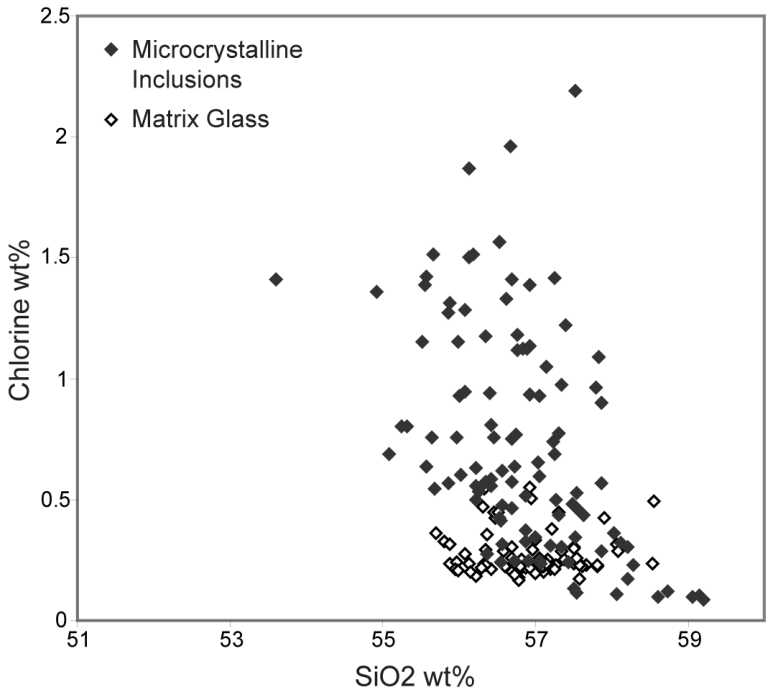

Fig. 2.11. Microprobe analysis of glass within microcrystalline inclusions (solid diamonds) and surrounding matrix (open diamonds) in tan clasts, displaying Cl vs SiO_2 values in weight %. Cl values range widely from <0.1 to 2.2 wt% in microcrystalline inclusions, while surrounding matrix values typically range from 0.17-0.35 wt%. The matrix glass Cl values >0.35 wt% are points taken near the inclusion-matrix boundary (see Fig. 2.10). SiO_2 values also range more widely in microcrystalline inclusions, likely due to the increased late stage crystallization within these areas.

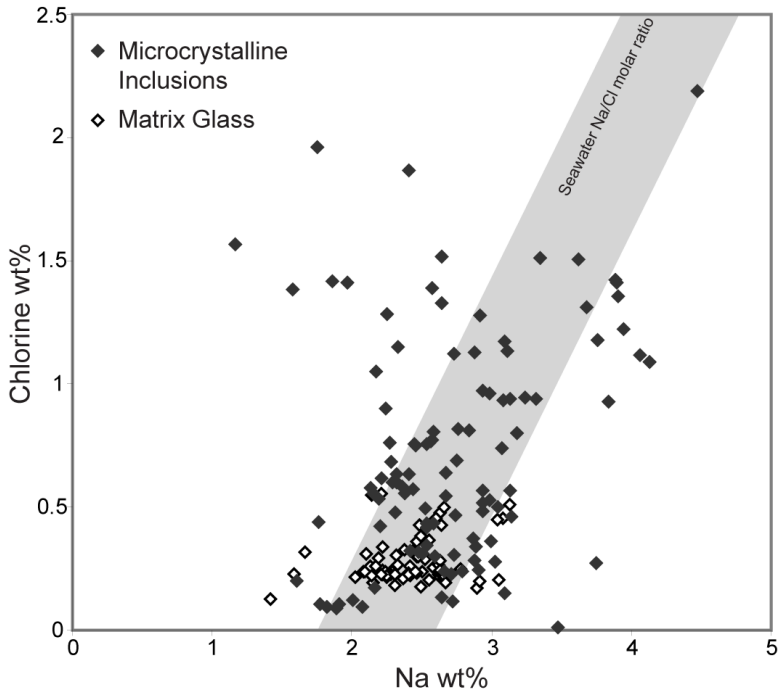

Fig. 2.12. Microprobe data showing the large range in both Cl and Na in microcrystalline inclusions (solid diamonds). The grey shaded region represents the expected trend if Na and Cl were added to glass at the molar ratio of seawater (~0.86) using the typical range of Na in matrix glass (open diamonds) as the starting point. Deviation from the grey shaded trend is likely due to variations in plagioclase crystallization and possible hydration of inclusion glass altering expected Na concentrations.

5.0. Discussion

Repeated multibeam mapping surveys and ROV observations have shown that persistent volcanic activity at NW Rota-1 has induced cyclic episodes of vent collapse and rebuilding (Chadwick et al., 2008; Walker et al., 2008; Chadwick et al., 2009). The timing of our 2006 cruise at NW Rota-1, which occurred shortly after a collapse event, allowed us to observe the early stages of vent reconstruction. Our observations of changes in the eruptive plume dynamics and the characteristics of ejected pyroclasts can be used to interpret the evolution of the uppermost part of the magmatic system during

this time. We show that both data sets suggest an evolution from diffuse gas venting through collapse-related pyroclasts to development of a robust vent structure that allowed magma direct access to the seafloor. These data sets also allow us to examine the effect of the seawater column on the eruption dynamics and pyroclast formation.

5.1. Eruption dynamics

5.1.1. Behavior of eruptive plumes

The behavior of eruption plumes provides important information on both the driving force for eruptive activity and the interaction of erupting mixtures with their environment. Eruption plumes typically initiate as momentum-driven jets and then transform to buoyant plumes as they lose momentum but maintain sufficient thermal buoyancy to continue rising (e.g., Morton, 1959; Keiffer and Sturtevant, 1984). The initial velocity of an eruptive plume thus records the conditions (overpressure) required to trigger the eruptive event. The length-scale over which the plume transitions from momentum-driven to buoyancy-driven and the rate of buoyant plume rise depend on both the characteristics of the plume (size, density and velocity) and the characteristics of the ambient fluid (density and viscosity). Although the behavior of subaerial eruptive plumes is well documented (e.g., Morton, 1959; Wilson and Self, 1980; Sparks et al., 1997; Woods, 1998), there are no comparable data on submarine eruptive plumes.

Eruptive plumes at NW Rota-1 show both momentum-driven and buoyancy-driven behavior. Early momentum-driven jets emerged at initial velocities of ≤4 m/s through loose pyroclastic deposits; these plumes decelerated during the first ~1.5 m of rise to

velocities of <0.5 m/s (Fig. 2.6b). Late-stage plumes emerged at velocities of <0.5 m/s and continued to rise at a constant rate. For comparison, Harris and Ripepe (2007a) document the behavior of small plumes produced by periodic 'puffing' events, which initiate at velocities of 12 m/s and decelerate to velocities of 6 m/s over the first two meters of plume rise. We consider puffing (which occurs at intervals of 1-2 s) to be analogous to the nearly continuous late-stage gas emissions observed at NW Rota-1. A comparison of the plume behaviors shows subaerial plumes to rise more quickly, and decelerate more slowly, than the submarine counterpart. Suppression of both the size and intensity of submarine eruption columns is predicted by theoretical models of submarine eruptive activity (Head and Wilson, 2003; Kokelaar, 1983; Kokelaar and Busby, 1992), which demonstrates the effects of higher ambient pressure, increased drag provided by water, and more efficient cooling of submarine eruptive plumes.

Our observations of buoyant plume rise allow us to estimate the efficiency of cooling by seawater entrainment. Following Wilson and Self (1980), we describe plume rise velocity (v) as a balance between buoyancy and the drag provided by the surrounding water, such that

$$v = \sqrt{(8rg\Delta\rho)/3\rho_{sw}C} \qquad (1)$$

where r is the plume radius, g is acceleration due to gravity, $\Delta\rho$ is the density contrast, ρ_{sw} is the density of seawater (1029.9 kg/m^3; assuming T = 7ºC and 3.5% salinity at 550 m bsl) and C is the drag coefficient (0.5 for a sphere). A plume radius of 1 m and average rise velocity of 0.5 m/s produce a density contrast of ~4.93 kg/m^3. This, in turn,

suggests an average plume temperature of about 27.2ºC, at 1-2 m above the vent (Fofonoff and Millard, 1983). The hottest fluid temperatures measured at NW Rota-1 are ~200ºC (D. Butterfield, pers. comm.), while observations of incandescence at the times of peak activity indicated magma temperatures in the vent in excess of 700ºC (Chadwick et al., 2008). An average plume temperature of 27ºC at a meter above the eruptive vent thus requires extremely rapid cooling (>200ºC/s). In comparison, puffing plumes at Stromboli volcano cool by <300ºC on a similar time scale (Harris and Ripepe, 2007a).

5.1.2. Implications for vent evolution and eruption dynamics

The observed evolution from intermittent and infrequent energetic plumes to nearly continuous buoyant plumes accompanied both an increase in eruptive vigor and a change in the visible vent structure from diffuse to focused. These observations appear counter-intuitive, as both focusing of the vent and increasing eruption intensity might be expected to produce more energetic eruption plumes. However, the observations can be explained if the eruptive activity is driven primarily by rising gas, rather than by a gas-magma mixture. In gas-driven eruptions within a static magma column, solid ejecta must be entrained by explosively expanding gases to escape the conduit. Even the most energetic eruptions appear to be driven by gas, despite flashes of incandescence observed at the vent (Chadwick et al., 2008).

A gas-driven scenario suggests that the diffuse venting that we observed during the early phase of activity reflects the absence of well-developed gas pathways to the surface, a consequence of vent 'beheading' because of the wholesale collapse of the

upper conduit. After collapse, the remaining conduit was covered by remobilized pyroclastic material. Rising pockets of gas from the magma column must traverse through this unconsolidated throat-fill to reach the seafloor. If the individual gas pockets are not strong enough to burst through the overlying material, they may accumulate and then abruptly force a path to the surface (e.g., Boudreau et al., 2005). From this perspective, we interpret the relatively high exit velocities of the early plumes as the consequence of pressurization of shallow gas pockets followed by sudden gas release at the seafloor. We infer that repeated rise of these gas pockets, and resulting disruption of overlying pyroclastic material, gradually cleared a pathway to the surface, thereby re-establishing a through-going conduit. In contrast, buoyant plume rise generated by the late-phase activity indicates gas release without measurable overpressures, which in turn suggests nearly continuous degassing through a well-established gas pathway.

Video observations show that late-stage eruptive activity was modulated by the formation and disruption of a quenched lava cap at the vent (Chadwick et al., 2008). Although this suggests that the magma column extended to the seafloor-water interface, 30-90 second pauses between eruptive events would not have been sufficient to allow large gas overpressures to develop. Additionally, the observed steady increase in acoustic amplitude accompanying each new eruptive pulse suggests that failure initiation was gradual (Chadwick et al., 2008). A gradual, rather than abrupt, onset in eruptive activity is consistent with our plume measurements, as both indicate gas release through balanced, rather than pressurized, plumes. Rare momentum-driven bursts occurred during the most energetic eruptions only when the vent opening became clogged with settling

pyroclasts or when the lava cap covering the vent ruptured abruptly rather than gradually (Video 3).

5.2. Seawater influences on pyroclast formation and deposition

The size and shape of pyroclasts reflect both conditions of magma ascent and eruption, and the environment in which the fragments are cooled and deposited. Clast formation in the submarine environment occurs through four primary processes: (1) magma fragmentation, (2) contact-surface steam explosivity, (3) bulk interaction steam explosivity and (4) cooling-contraction granulation (Kokelaar, 1986). Our understanding of how these processes are affected by depth below sea level is limited.

Evidence for purely magmatic fragmentation has been documented in mid-ocean ridge and ocean island environments, primarily in the form of glassy bubble-wall shards (e.g., Clague et al., 2003a,b; Clague et al., 2009a; Maicher and White, 2001). At NW Rota-1, bubble-wall shards are not present, possibly due to higher crystallinity than is typically found in mid-ocean ridge basalts. Abundant fine ash is common in shallow-water environments (e.g., Mastin, 2007; Wohletz, 1983; Walker, 1973; Walker and Croasdale, 1971), and may reflect the high energy provided by contact-surface interactions and/or bulk interaction of external water with magma. Clast morphologies generated by contact-surface and bulk interactions include blocky and equant, moss-like and convoluted, fluidal (both irregular and drop-like with smooth surfaces), or plate-like (Wohletz, 1983). Cooling-contraction granulation is most likely to form blocky, equant

clasts and likely occurs at any depth (e.g., Kokelaar, 1986; Wohletz, 1983; Büttner et al., 2002).

Changes in the mechanisms of magma-water interactions at shallow depths were documented during the 1963 eruption of Surtsey, Iceland, as the location of eruptive activity moved from submarine to subaerial. The submarine deposits (≤120 m bsl) are poorly sorted and composed of glassy clasts with median grain sizes of 2-4 mm. In contrast, the deposits of subaerial surtseyan explosive eruptions are very poorly sorted and dominated by fine particles (Kokelaar and Durant, 1983). This study suggests that rapid expansion of steam at the seawater-atmosphere interface increases the extent of both contact-surface and bulk interactions, and the efficiency of fragmentation. Importantly, this level of fragmentation energy appears to be limited to very shallow water.

At NW Rota-1, all scoop samples from the active vent region are well sorted, with median grain sizes of 2-4 mm (-1ϕ). Although we were unable to collect bulk samples during the later (larger) eruptions, video footage of this activity suggests that these eruptions produced many larger clasts and were dominated by coarse ash and lapilli, with limited fine ash. Small strombolian eruptions, such as those observed at NW Rota-1, may provide insufficient energy to induce the physical mixing of magma and seawater required for bulk interactions. Moreover, although limited flashing of water to steam was interpreted to be occurring in the vent during the most vigorous eruptive activity (Chadwick et al., 2008), these contact-surface interactions produced no obvious effect on the fragmentation process. The limited energy of eruption may be insufficient to sustain

steam explosions when particle sizes become so small (~1 mm) that cooling does not create enough steam to continue fragmentation (Head and Wilson, 2003; Wohletz, 1983). Therefore, we concur with Kokelaar and Durant (1983) that efficient fragmentation due to contact-surface interactions is limited to very shallow water (10s of meters).

What was the effect of seawater on pyroclast generation at NW Rota-1? Secondary fragmentation could be seen as the spontaneous disruption of larger clasts within the eruption plume and as small particles spalled off larger clasts as they settled to the seafloor. Additionally, the abundance of blocky, equant clasts in all eruptive deposits supports an interpretation of water-induced fragmentation (cooling-contraction granulation). Therefore, although the relative importance of syn-eruptive magmatic fragmentation and post-eruptive quench granulation cannot be quantified, we infer that much of the ash and lapilli were produced or modified through secondary fragmentation processes.

5.3. Vent dynamics

At NW Rota-1 seawater appears to modulate vent dynamics by quenching lava exposed to seawater within the vent. It is useful to ask whether seawater interaction also controls the dimensions of the vent. All eruptive activity at NW Rota-1 emerges from openings less than 1.5 m in diameter, which is small compared to most subaerial vents. Therefore, our observations suggest that, in addition to low eruption rates, plume suppression and severe restriction of the area over which clasts are deposited, seawater serves to limit the size of both the vent itself and constructional features around the vent.

Possible controls on vent diameter could be the rate of magma supply to the vent, the gas flux, or the thermal balance between emission of hot gas and magma and quenching by seawater.

5.3.1. Evidence for pyroclast recycling

Recycling of pyroclasts is not uncommon at subaerial volcanoes and may be more common at small submarine eruptions due to ejection into ambient seawater. Recycling has been observed at subaerial scoria cones when pyroclasts on the inner cone slopes slide back into the vent (Heiken, 1978) and are recognized as abraded scoria lapilli (Valentine and Gregg, 2008). In phreatomagmatic and surtseyan eruptions, instabilities within the inner cone slopes create a slurry of previously ejected material and infiltrating water, resulting in up-rushing jets of juvenile material, recycled clasts and steam (Kokelaar, 1983), commonly producing cored lapilli. Recycling has also been observed at the submarine volcano West Mata, Lau Basin, where repeated cycling of clasts through the vent during degassing episodes produced rounded cobbles that account for ~33% of near vent ejecta (Clague et al., 2009b). At NW Rota-1, pyroclasts were also observed to fall back into the vent (Video 3). Here we suggest that recycling was enhanced by suppression of the eruptive plume by hydrostatic pressure, cooling effects, and drag of the overlying water column.

At NW Rota-1, we see evidence for recycling in both the textures and glass compositions of Brimstone clasts. Textural evidence is both macroscopic - with (typically altered) clasts entrained within or embedded in the surfaces of large pyroclasts (Fig.

2.7g,h) - and microscopic, with microcrystalline inclusions included within crystal-poor matrix glass (Fig. 2.9a,b). Although pyroclasts from scoria cone eruptions commonly show incorporation of more crystalline magma within less crystalline magma, these textures have been interpreted as entrainment of more crystalline material from either the sidewalls of the conduit (e.g., Taddeucci et al., 2004; Lautze and Houghton, 2007) or from mixing of deep (less degassed) and shallow (more degassed) magma reservoirs (Metrich et al., 2001; Pioli et al., 2008).

Matrix glass compositions in NW Rota-1 samples provide convincing evidence for recycling. Specifically, the groundmass glass within the recycled regions shows anomalous enrichments in chlorine and, to a lesser extent, sodium (Figs. 2.11, 2.12), which suggests assimilation of either seawater or brine. Adding seawater or a seawater-derived brine to the melt should produce Na:Cl enrichment at the molar ratio of seawater (~0.86; Fig. 2.12, shaded area). However, Na concentrations are also affected by the crystallization of plagioclase, which may have simultaneously reduced the Na content of the melt. The highest Cl concentrations (≤2.2 wt%) were found along the mixing boundaries between recycled areas and surrounding glassy matrix (Fig. 2.10).

The very high Cl contents along the margins of the mingled clasts suggest surface contact with a Cl-rich brine or salt. At 550 m bsl, as pyroclasts fall back into the vent seawater trapped within surface vesicles will vaporize and separate from the clast, leaving NaCl-rich brine or salts present on the pyroclast surface. Elevated Cl concentrations within the inclusion glass require Cl diffusion inward from the surface. In an anhydrous melt, Cl diffusion rates are on the order of 30-115 seconds over a distance

of 100 μm at temperatures of 700ºC-1000ºC (Bai and Koster van Groos, 1994), providing minimum times required for Cl incorporation into quenched clast interiors. In hydrous melts the time required for diffusion is reduced (Alletti et al., 2007). Interestingly, there is no evidence for Cl diffusion into the surrounding matrix glass, which may suggest the inclusion glass is hydrated during recycling, facilitating diffusion. The presence of water may also explain the scatter in the Na microprobe data within inclusion glass (Fig. 2.12).

Reheating of recycled clasts within the vent is indicated by deformation of included clasts and development of internal flow-banding. It appears that this reheating may also have caused the observed increase in groundmass crystallinity, perhaps as the quenched glass was heated above the glass transition temperature. Preservation of both compositional and textural evidence of clast recycling sets limits on the time scales of clast residence within the vent magma. In particular, diffusion of Cl within, but not outside of, microcrystalline inclusions indicates that the timescales of recycling are rapid, consistent with the nearly continuous activity observed during this time period.

Observations of pyroclast recycling are not unique to the submarine environment, but may be characteristic of low mass eruption rates (MERs) and strombolian eruptive styles. Low MER eruptions are pulsatory and have insufficient energy to expel all erupted pyroclasts from the vent, allowing some clasts to fall or slide back in between individual explosive events. We suspect recycling of pyroclasts to be facilitated in the subaqueous environment because of hydrostatic suppression of eruptive plumes and increased drag on erupted particles, both of which limit the extent to which pyroclasts are transported away

from the vent. However, our identification of recycled clasts by microcrystalline textures in addition to anomalous Cl raises the intriguing possibility that similar textures observed in subaerial basaltic pyroclasts (e.g., Taddeucci et al., 2004; Lautze and Houghton, 2007) may have a similar origin.

5.3.2. Extent of pyroclast recycling

Quantifying the extent of clast recycling at NW Rota-1 is difficult as ROV observations and sampling in 2006 provide only a snapshot of the activity. However, if we assume that the late stage activity is representative of explosive volcanism at NW Rota-1, we can estimate the extent of recycling through thin section analysis of clasts from sample J2-191-7. Recycling textures are found in 65% of the clasts made into thin sections (15 total), where, recycled inclusions occupy 3-20% of individual thin section areas. This suggests that up to ~15% of total volume of pyroclasts erupted during the late stage activity may be recycled. This estimate does not include pyroclasts that are re-ejected without being entrained by fresh melt. Therefore, if >15% of the erupted material is recycled, then only ~85% of the magma emitted during a single event is deposited, and thus recorded as accumulated mass.

6.0. Conclusions

Observations of eruptive activity in 2006 at NW Rota-1 volcano at a depth of ~550 m bsl documented the evolution from intermittent discrete gas bursts from a diffuse vent region (early phase) to nearly continuous activity from a focused vent (late phase).

The early discrete plumes initiated as momentum-driven jets indicating overpressure buildup beneath loose pyroclastic deposits. Late-stage activity produced nearly continuous buoyancy-driven plumes indicative of a robust and open gas pathway. Suppression of rising plumes by cooling and drag exerted by the surrounding water caused most coarse ejected material to fall from the plume within a few meters above the vent and accumulate as a small cone (~5 m diameter). All eruptive activity produced both fresh and altered clasts with both fluidal and blocky morphologies. During the week of observations, the percentage of juvenile components and fluidal morphologies increased, and the mean clast density decreased, as the mass eruption rate (MER) increased. We use these characteristics to suggest that the clasts formed primarily by magmatic fragmentation but with secondary fragmentation due to cooling-contraction (quench) granulation. Contact-surface and bulk interaction steam explosivity appear to play little or no role in clast formation at NW Rota-1, suggesting that the combination of low MERs and rapid cooling created insufficient energy for steam explosions.

Evidence for pyroclast recycling is found in hand sample as entrained clasts and in thin section as microcrystalline regions within microlite-poor glass. The microcrystalline regions have anomalously high Cl and elevated Na concentrations, suggesting assimilation of NaCl-rich brine or salts into the melt. The recycling mechanism proposed could occur at any underwater explosive basaltic vent, although the limited observations of elevated Cl and Na in submarine basalts to date suggest that the assimilation of seawater, brine or salts may require very specific eruption conditions.

Bridge from Chapter II to III

In Chapter II, I discussed the eruptions observed and sampled from NW Rota-1, Mariana arc in 2006 and introduced the concept of pyroclast recycling in volcanoes with low mass eruption rates, particularly in the submarine environment. Chapter II discussed how the suppression of eruptive plumes in the submarine environment likely increases the probability of recycling pyroclasts and presents evidence of seawater assimilation through chlorine and sodium enrichments. In Chapter III, I further investigate pyroclast recycling using electron dispersive spectroscopy to map Cl enrichment and use Cl diffusion rates and crystallization experiments to constrain the timescales on which recycling occurs. Furthermore, I use crystallinities of samples from observed effusive and explosive episodes, along with summit tephra samples to explore the full range of activity for NW Rota-1.

CHAPTER III

SEAWATER ASSIMILATION PROVIDES EVIDENCE OF PYROCLAST RECYCLING DURING LOW ENERGY BASALTIC ERUPTIONS

1.0. Introduction

Tephra produced by explosive eruptions provides important information about magma ascent, vesiculation, fragmentation, and deposition. Unlike silicic pyroclasts from Plinian and subplinian eruptions, which typically have a limited range in vesicularity (e.g., Cashman, 2004), mafic pyroclasts from strombolian to violent strombolian eruptions are characterized by a wide range in both vesicularity and groundmass crystallinity (e.g., Heiken, 1978). In particular, mafic pyroclasts are often classified as either sideromelane (vesicular and microlite-poor) or tachylite (microlite-rich); both sideromelane and tachylite are often found within the same depositional layers, and even within a single clast. However, the origin of these clast types, and the ascent and eruption conditions implied by the variable proportions of different clasts types, is not well understood.

The presence of both sideromelane and tachylite is a common feature of tephra deposits from cinder cone eruptions (e.g., Cinder Cone, CA - Heiken, 1978; Stromboli, Italy - Lautze and Houghton, 2005, 2007; Mt. Etna, Italy - Taddeucci et al., 2004; Paricutin, Mexico - Pioli et al., 2008; Newberry Volcano, OR - McKay et al., 2009; Mt. Vesuvius, Italy - D'Oriano et al., 2011). Sideromelane clasts are generally assumed to represent primary (deeper) magma that ascends rapidly and erupts. Tachylite clasts have

been interpreted as slow-moving magma incorporated from along conduit walls (Lautze and Houghton, 2007; Taddeucci et al., 2004), or as magma stored temporarily in shallow dikes and sills (Pioli et al, 2008; Metrich et al, 2001); both scenarios call upon sufficiently long residence times within the upper crust to allow magma degassing and crystallization prior to eruption. An alternative explanation is additional residence time in the vent by recycling previously erupted clasts (Chapter II), a mechanism that should be pronounced when mass eruption rates (MERs) are sufficiently low that clasts are not transported far from the vent.

The ongoing eruption of NW Rota-1 submarine volcano provides a unique opportunity to test the recycling hypothesis. Identifying recycled clasts with certainty requires that they have a unique chemical and/or textural signature. In chapter II we first suggested pyroclasts were recycled at NW Rota-1 due to observations of plume suppression and limited clast deposition and textural and geochemical evidence including microcrystalline inclusions with Na and Cl enrichment. Here we demonstrate how seawater-derived Cl is easily mapped in the matrix glass of quenched pyroclasts and we constrain time scales of recycling by experiments designed to examine rates of crystallization during clast reheating. Time scales of minutes to tens of minutes suggest that a limited range of eruption conditions will allow both efficient clast recycling and enough time for reheating/crystallization.

2.0. NW Rota-1, southern Mariana arc

NW Rota-1 is an active basaltic andesite submarine volcano with its summit at ~517m below sea level that is located in the southern Mariana arc, ~100km north of Guam. The volcano was directly observed for the first time in 2004 (Embley et al., 2006) and has been the target of five subsequent ROV (remotely operated vehicle) cruises in 2005, 2006, 2009 (two visits) and 2010. The observed eruptive activity has ranged from slow extrusion of solidified lava at mass eruption rates of $<5m^3$/hr (in 2009, 2010: Chadwick et al., 2009) to low-moderate strombolian explosions at MER = 5-100m^3/hr (in 2004-2006 and 2010: Embley et al., 2006; Chadwick et al, 2008; Chapter II) to more energetic explosive (strombolian) activity in 2008 and 2009 (MER >100m^3/hr inferred from hydrophone records; Dziak et al., 2009; Chadwick et al., in review). During slow effusive activity, lava emerged from the vent as solidified lava spines (<1-2m diameter) that disintegrated into smaller blocks as they emerged from the vent. Observed strombolian activity produced intermittent gas bursts at low MER and nearly continuous emissions of gas and pyroclasts at moderate MER; eruption plumes from this activity were 10s of meters high (Chadwick et al., 2008; Chapter II). During the most vigorous activity observed in 2006, explosions were cyclic, with 2-6 minutes of gas emissions alternating with 30-40 seconds of quiescence (Chadwick et al., 2008).

Pyroclast size, shape, and texture vary with eruption style. During slow lava extrusion, dense angular fragments are formed by 'quench granulation' when hot lava encounters cold seawater. These quench granulated clasts are mobilized by vigorous degassing in the vent to be deposited within a few meters from the vent. During low-

moderate strombolian eruptions, explosive plumes are suppressed by ambient seawater to the extent that most pyroclasts fall out of the plume within <4m above the vent and are deposited within a few meters of the vent to form a coarse-grained, poorly sorted clastic cone. The observed transport distance for most pyroclasts at NW Rota-1 is limited to meters. However, we have observed fresh (unaltered) vesicular clasts at the volcano summit during each ROV visit. Therefore, we infer the highest MER activity to have blanketed the summit of NW Rota-1 (45m north of, and ~5 to 40m above, the primary vent) with pyroclasts; since the low-moderate strombolian eruptions have insufficient strength to deposit lapilli at this distance. Our inferred high MER energetic eruptions are also supported by hydrophone acoustic recordings of greater energy than any eruptions yet observed. Further evidence for three eruption types (low MER effusive, low-moderate strombolian, high MER energetic strombolian) at NW Rota-1 lies in the variability of pyroclast morphology and density; suggesting that individual clasts have different ascent and fragmentation histories (Chapter II).

The groundmass textures of individual pyroclasts also vary with eruption style. At the low-MER end of the spectrum, lava blocks and spalled fragments are nearly holocrystalline because of extensive (syn-eruptive) plagioclase and clinopyroxene crystallization. Pyroclasts from the low-moderate strombolian eruptions are both microlite-rich and microlite-poor; it is common to find the two groundmass textures within the same clast, in which case the microcrystalline regions are always included within a microlite-poor matrix (Fig. 3.1a). Similar textures are common in the products of some subaerial violent strombolian (e.g., Erlund et al., 2010) and strombolian eruptions

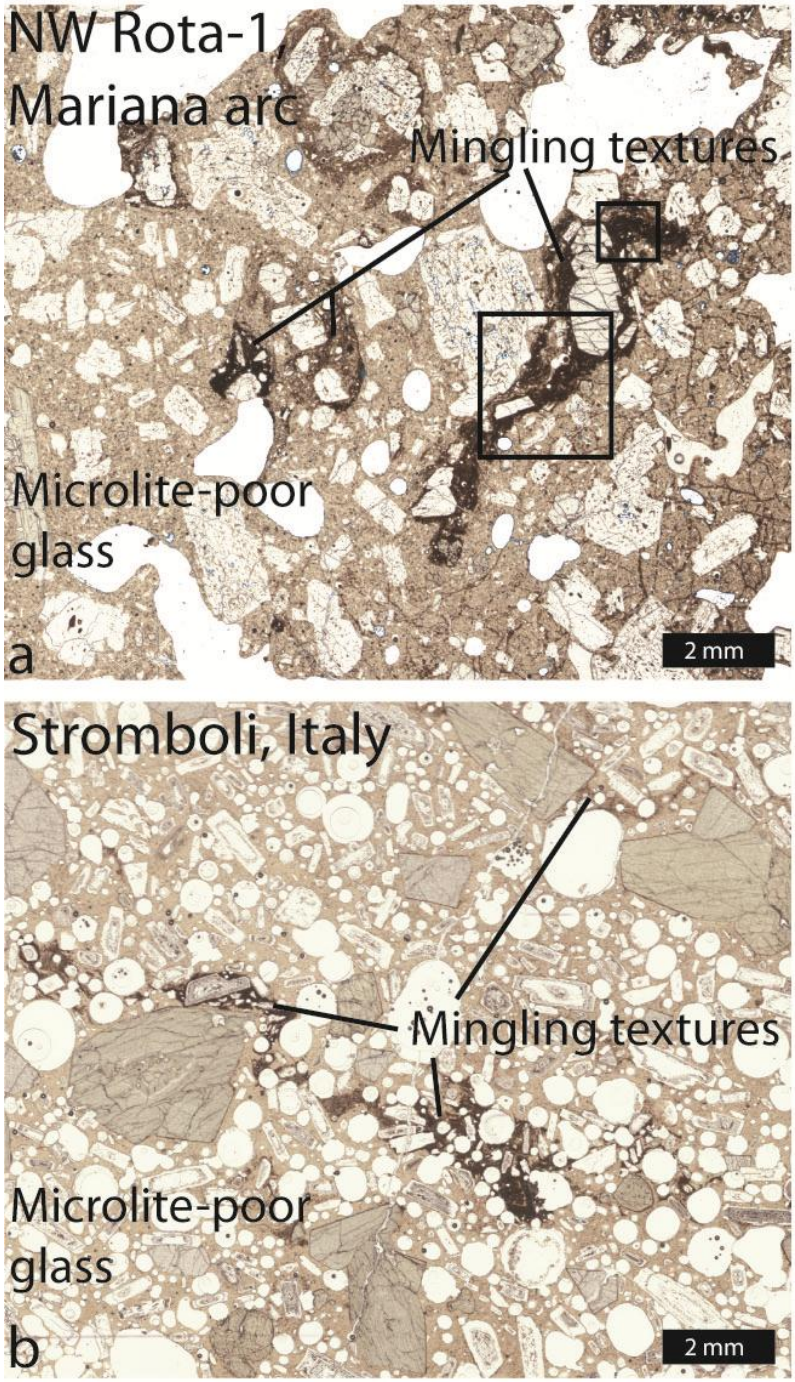

Fig. 3.1.- Thin section scans from NW Rota-1 and Stromboli volcanoes. Thin sections have microlite-poor (tan-sideromelane) matrix glass with microcrystalline inclusions. Inclusions can have sharp or diffuse boundaries. (a) NW Rota-1- small box designates area in Fig. 3.2a; large box represents area for EDS scan in Fig. 3.4. (b) Stromboli-subaerial microcrystalline inclusions show strikingly similar textures.

(e.g., Fig. 3.1b). Pyroclasts from the summit, produced by the most energetic (high MER) eruptions are uniformly glassy and nearly free of microlites.

3.0. Methods

Thin sections of 29 representative lava and pyroclast samples from NW Rota-1 were analyzed for groundmass crystallinity. Full thin section scans permitted evaluation of groundmass heterogeneity and were used to target areas for detailed imaging by back-scattered electron (BSE) microscopy using a FEI Quanta 200 SEM at the University of Oregon. BSE images were analyzed for plagioclase abundance only, because plagioclase is the easiest phase to measure by semi-automated image processing. Element maps were generated for selected areas within 15 thin sections using Energy-Dispersive X-ray Spectroscopy (EDS) to identify variations in the chemical composition of the matrix glass. In particular, EDS images allowed us to identify matrix regions with anomalously high Cl concentrations. We then obtained microprobe analyses of the matrix glass in four of these samples using a Cameca SX100 microprobe at the University of Oregon; operating conditions included an accelerating voltage of 12keV, a beam current of 20nA and a beam diameter of 2.5μm. The elements analyzed include major and minor elements (Na_2O, K_2O, Al_2O_3, MgO, FeO, TiO_2, MnO, P_2O_5, SiO_2, CaO, and NiO) and the volatile elements F, S and Cl. Total count times for each beam location was >200 seconds, although the most volatile elements (i.e. Na) were analyzed first to limit loss.

Reheating experiments on natural basaltic lapilli from Paricutin, Mexico (see Erlund et al., 2010) were conducted to test the effect of reheating on crystallinity in

tephra with recycled textures. Heating experiments were attempted on NW Rota-1 samples, however heating the clasts resulted in an odd alteration where the glass 'inflated' producing a bubbly, popcorn texture that was very brittle. We were unable to polish or analyze these samples with the SEM. The 'inflation' of NW Rota-1 glass may be due to moderately hydrous glass. We determined volatile contents by analyzing matrix glass using Fourier transform infrared spectroscopy (H_2O: 0.3-1.1wt%; CO2: below detection limits).

We chose Paricutin lapilli for the low volatile contents and because eruptions and deposits have been well studied and are of similar composition to NW Rota-1.We selected clasts of 4-8 mm in diameter, split them in half (saving one half as a control), and heated each in a one-atmosphere Deltec furnace at atmospheric oxygen fugacities (fO_2). Each clast was heated isothermally for 5-30 minutes at temperatures (T) ≥1100°C and 5-60 minutes at T = 600-1000°C. Images of both the control and the experimental samples permitted classification according to differences in groundmass texture caused by heating.

4.0. Groundmass textures

Microcrystalline inclusions in NW Rota-1 thin sections are medium to dark brown in color and have boundaries that are either sharp or diffuse, suggesting mingling (Fig. 3.1). We define mingling as mixing between surrounding and inclusion matrix. BSE images show that groundmass crystals are dominantly plagioclase and pyroxene, and may include small amounts of tiny oxides (Fig. 3.2a-d). Figure 3.2a shows a sharp boundary

between a microcrystalline area (left) and a microlite-poor area (right). In figure 3.2b an elongated inclusion is wrapped around microlite-poor glass (bottom right); this inclusion has fluidal groundmass textures with crystal alignment (location- small box in Fig. 3.1). A close up view of Fig. 3.2b shows that the inclusion has abundant plagioclase and pyroxene microphenocrysts as well as very fine-scale crystallization of the matrix glass (Fig. 3.2c). Similar fine-scale crystallization occurs within phenocryst-hosted melt inclusions (Fig. 3.2d) within microlite-rich areas; melt inclusions in microlite-poor matrix are not crystallized (Fig. 3.2d). The mingling of crystalline textures, tiny oxides, and crystal alignment are not observed in lava samples or summit tephra.

We measured the abundance of plagioclase microlites and microphenocrysts (<10,000 μm^2) in samples of lava (low MER), and pyroclasts from both low-level explosive (low-moderate MER) eruptions collected near the vent and from the summit (inferred high MER). Plagioclase microlite crystallinity varies from up to 71% in the lava, to 5-10% in the summit tephra (Fig. 3.3). Pyroclasts generated by low-moderate MER eruptions also have intermediate crystallinities (14-33%); moreover, these are the only clasts that show mingling between microlite-poor (14-21% plagioclase crystallinity) and microlite-rich (24-33% microlite crystallinity) matrix regions. Although we were not able to adequately measure the very small mafic crystals (microlites) in all analyzed images, their abundances also vary among samples. Mafic microlites form 15-35% of the lava groundmass, making some samples nearly holocrystalline. In contrast, the summit tephra has very few mafic microlites, whereas mingled pyroclasts from intermediate

activity have <8% mafic crystals in microlite-poor matrix and <15% in microcrystalline areas.

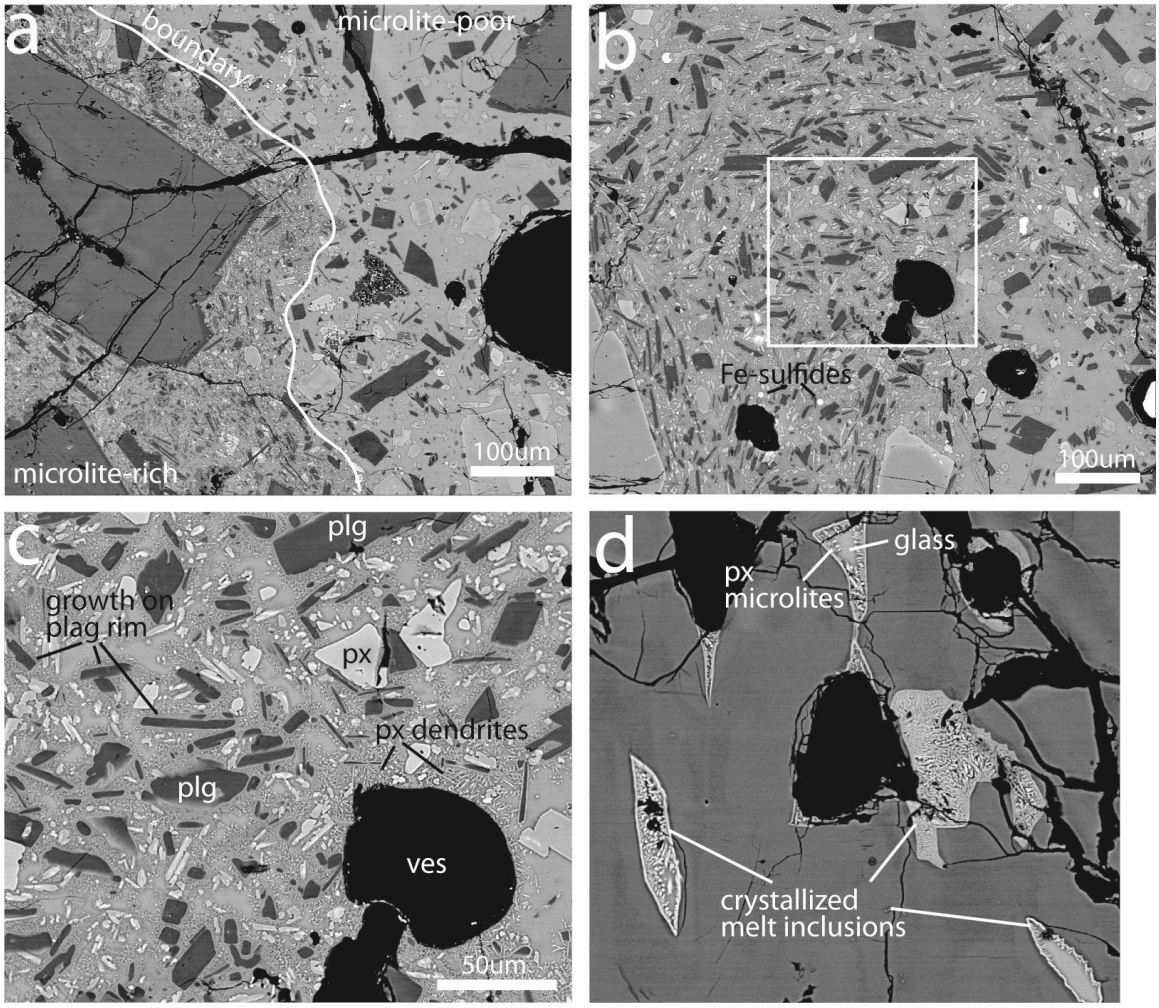

Fig. 3.2.- Backscatter electron images of microcrystalline inclusions. (a) boundary between microlite-poor area (right) and microcrystalline inclusion (left) (b) crystal alignment within sheared inclusion. Bright white spots are Fe-sulfides. White box represents area of (c). (c) blow up of (b) showing rapid crystallization textures in matrix glass and growth on pre-existing plagioclase rims. Labels are plagioclase (plg), pyroxene (px), vesicle (ves). (d) plagioclase phenocryst in inclusion area with crystalline melt inclusions. Bright crystals are pyroxenes.

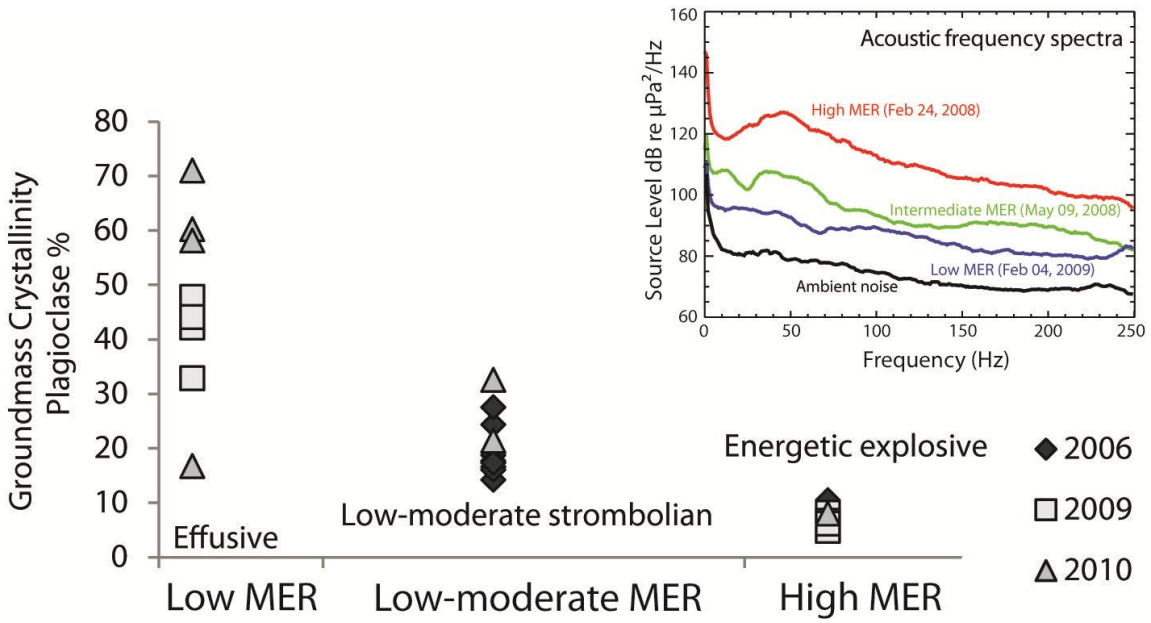

Fig. 3.3.- Groundmass plagioclase crystallinity vs. mass eruption rate (MER) associated with three types of eruptive activity at NW Rota-1. As the MER increases, the groundmass crystallinity decreases. Low MER samples from effusive lava (2009-2010) have the highest crystallinities. Low-level explosive eruptions have intermediate MER and crystallinities. Samples identified by microcrystalline inclusions within sideromelane. The highest MER samples are inferred to be from larger explosive events, evident in hydrophone data but not yet directly observed. Inset shows hydrophone frequency spectra of the three representative types of activity. Each curve is 10-20dB, or 5-10 times as great as the one below. The high MER activity produces sound levels that are 40-50dB above ambient sound levels.

5.0. Range of eruptive activity at NW Rota-1

Microcrystalline inclusions are common in samples from the moderate strombolian activity of 2006 and 2010; in contrast, these textures are not observed in either lava samples from the slow effusive activity or in tephra collected from the volcano's summit (representing the most energetic explosions). These three sample suites also have distinct groundmass crystallinities that suggest different magma ascent rates and degassing histories (Fig. 3.3). For example, the microlite-poor regions in moderate

strombolian eruptions have higher crystallinities than the summit tephra. This may be due to increased crystallization from extensive mingling and mixing with microcrystalline areas or from slower magma ascent than the summit samples. Effusive lava presumably represents the longest ascent times, allowing extensive degassing and crystallization. The distinct crystallinities of the samples likely represent the full range of crystallization for 2006-2010 activity at NW Rota-1. Lava effusion represents the lowest level of activity (MER $<5m^3$/hr). The low-moderate submarine strombolian eruptions cover a larger range of activity (MER: <5-$100m^3$/hr; Chadwick et al., 2008) and have microcrystalline inclusions. The most energetic activity has been documented by hydrophone monitoring, and is probably represented by vesicular microlite-poor tephra found on the summit.

The three types of eruptive activity at NW Rota-1 have also been characterized acoustically using temporary (hours to days) portable and long-term (1 year) moored hydrophone deployments. The temporary hydrophone was used in 2006 to record low-moderate strombolian explosions; characterized by cyclic activity fluctuating between little or no activity and strong, semi-continuous explosive bursting (Chadwick et al., 2008). The two long-term hydrophone deployments provide evidence of temporal variations in eruptions from Feb. 2008 to Feb. 2009 and Feb. 2009 to Feb. 2010 (Dziak et al., 2009; Chadwick et al., submitted). Figure 3.3 (inset) shows the sound levels associated with the three types of eruptive activity as representative frequency spectra. For example, the loudest explosions produce spectra that are >30dB higher at all frequencies, which means the acoustic amplitude of the strong activity is >15x louder

than the low MER activity. ROV dives during hydrophone deployments allowed observations of eruptive styles to be linked with hydrophone data recorded in 2006 (Chadwick et al., 2008), 2009, and 2010.

6.0. Evidence of recycling

As previously stated, moderate strombolian activity at NW Rota-1 produces pyroclasts that often have microcrystalline inclusions within microlite-poor matrix. To examine these groundmass textures, matrix glass compositions were analyzed in four inclusion-bearing clasts. Variable crystallinity of the inclusions causes some variation in the major element composition of the matrix glass (particularly in SiO_2, FeO, MgO and CaO; Chapter II). For example, figure 3.4a (large square in Fig.3.1a) shows a microcrystalline inclusion that is elongated from the bottom left to the top right of the image. In figure 3.4a, the microcrystalline region is identified by its medium gray appearance (caused by the presence of numerous tiny plagioclase crystals), which contrasts with the light gray of the surrounding (and microlite-poor) matrix glass. Also note the complex mingling textures of light and dark gray matrix within this region.

The most striking difference between the microlite-rich inclusions and the microlite-poor matrix lies in the elevated Cl (<2.2wt%) and Na (<4.5wt%) content of the inclusions (Figs. 3.4b-d). Cl, in particular, varies strongly between the host matrix (0.17-0.35wt%) and inclusion glass (0.1-2.2wt%; Chapter II). A Cl x-ray map (Fig. 3.4b) shows the high Cl content of the matrix glass in the inclusions (<1.9wt%). Na enrichments are not as striking (Fig. 3.4c), probably because of the increased plagioclase crystallization

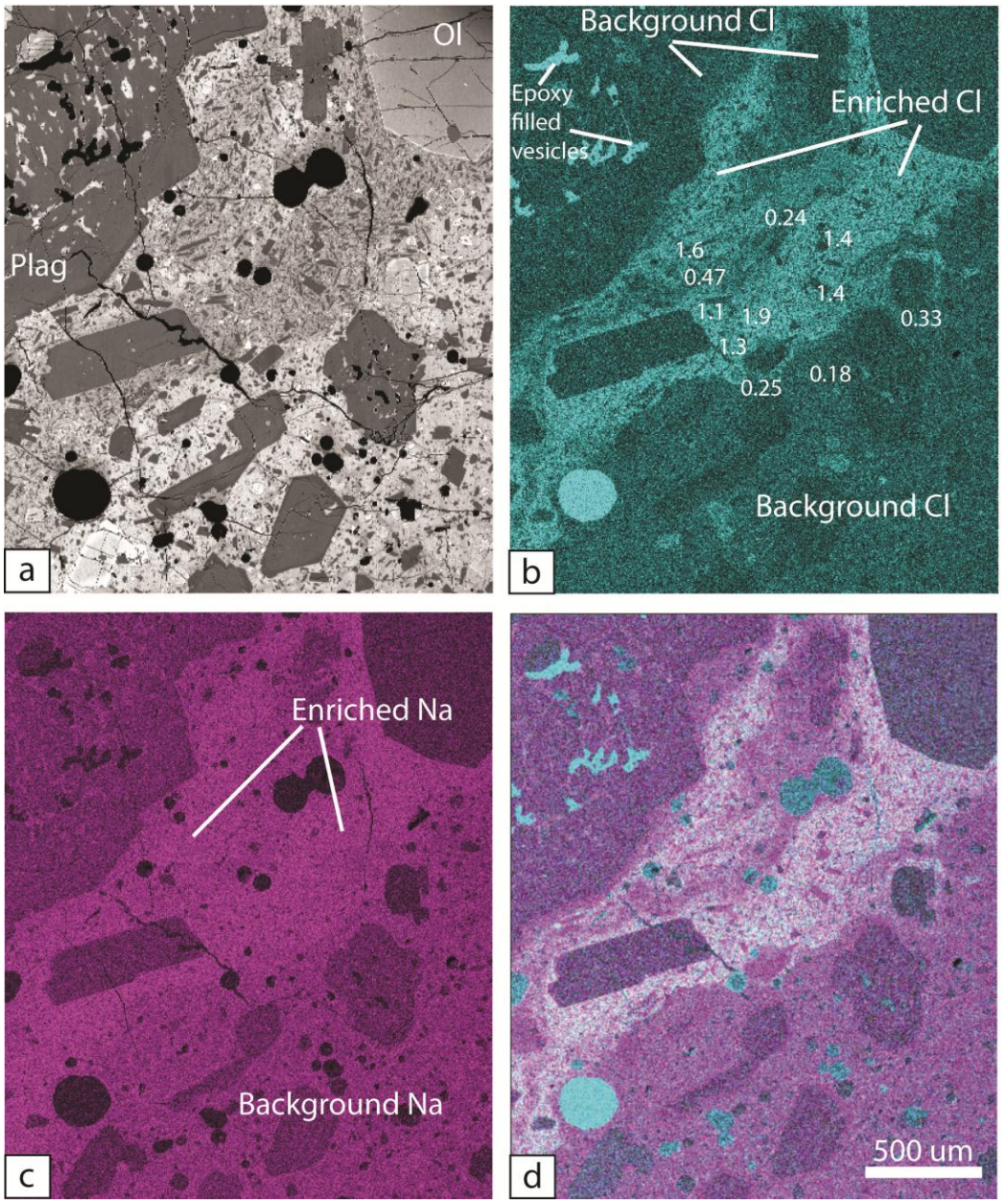

Fig. 3.4.- BSE and electron-dispersive x-ray spectroscopy images. (a) BSE image of elongated microcrystalline inclusion shown as dark diagonal strip from bottom left to top right. Note the thin strip of less crystalline glass within the inclusion. (b) Cl x-ray map showing counts of EDS scan. Bright areas are enriched in Cl; dark areas are background values. Numbers are Cl concentrations in weight %. (c) Na x-ray map; bright areas align with Cl enrichment. (d) Cl and Na maps overlain on BSE image. Background concentrations (dark areas) are distinctly separated from enriched microcrystalline areas, showing delicate mixing along the boundaries and thin strip of possibly included less crystalline matrix glass.

(which depletes the Na content of the melt). A combined Cl and Na element map (Fig. 3.4d) shows the intricate mingling of the inclusions with the host melt. Note the thin strip of less crystalline (darker) glass, which suggests that the microcrystalline inclusion was either folded and sheared, encapsulating a strip of surrounding matrix glass or, alternatively, that maximum enrichment occurs along the boundaries of the clast. The image also suggests that, although sufficiently fluid to flow, the included clast retained fairly sharp boundaries, particularly where it flowed past the large plagioclase phenocryst shown in the upper left of each image.

The elevated Cl and Na contents within microcrystalline inclusions suggest interaction with seawater. However, the Na/Cl ratios are not entirely explained by simple incorporation of seawater (Chapter II). We suggest that two factors may explain this discrepancy. First, the extensive plagioclase crystallization will consume Na, thus lowering the Na/Cl ratio of the glass. Second, our microprobe analyses used a narrow (2.5μm diameter), focused beam and long count times (>200sec) which, although Na was the first element analyzed, may have caused some data loss. In addition, the very high measured Cl contents (≤2.2wt%) are approaching saturation levels in molten basalt (Webster et al., 1999). The assimilation of seawater (~1.9wt% Cl) and NW Rota-1 melt (~0.2wt% Cl- background average) would produce Cl values well below the Cl enrichment (<2.2wt%) measured within NW Rota-1 inclusions, suggesting the inclusion of NaCl-rich brine or salts instead. A key observation is that the Cl and Na maps show the enrichment is limited to the microcrystalline areas, suggesting crystallization and Cl assimilation may have occurred at the same time.

7.0. Recycling of pyroclasts

During the moderately explosive activity of April 2006, we observed that pyroclasts frequently fell back into the vent (Chadwick et al., 2008; Chapter II). Incandescent material observed within the vent requires temperatures in excess of 700°C (Chadwick et al., 2008). These high temperatures are sufficient to cause seawater to boil, leaving behind either a NaCl-rich brine or salt on the exterior surfaces and within vesicles and cracks of the pyroclasts (Fig. 3.5). Additionally, the incandescent material suggests the vent and upper conduit are of sufficient temperature to prevent the direct intrusion of seawater. Therefore, previously erupted clasts with a NaCl-rich coating or pockets could be incorporated back into the melt by falling directly into the vent, by sliding down the interior slopes of the growing scoria cone, or by slumping of cone debris within the vent. Evidence of clast reheating within the melt is provided by (1) varying degrees of deformation, mingling, and banding of recycled material, as seen in thin section (Fig. 3.1) and BSE images (Fig. 3.2) and element maps (Fig. 3.4); (2) recrystallization of included clasts, which is more likely to occur during reheating than during rapid quenching on eruption (e.g. Burkhard, 2001), and (3) limited diffusion of Cl from included clast margins into the surrounding matrix glass.

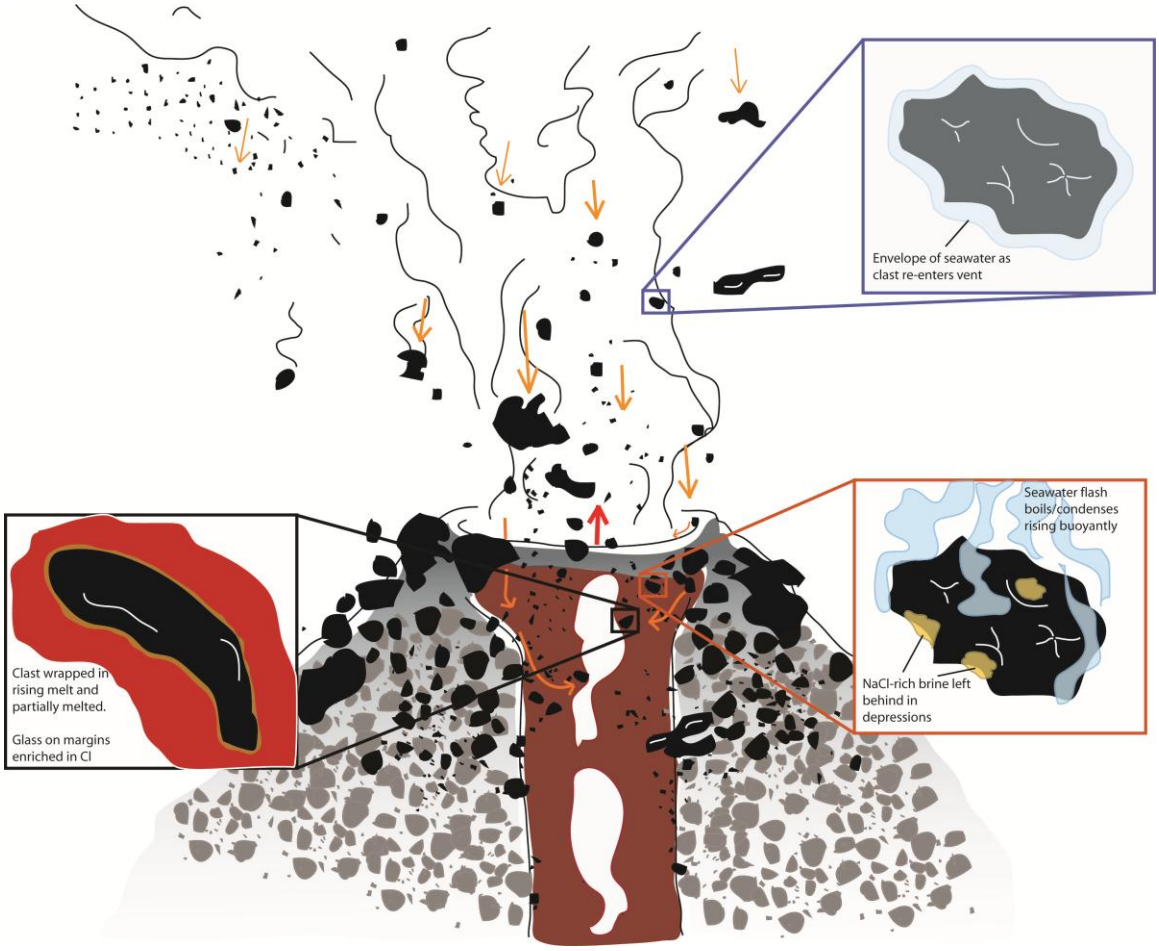

Fig. 3.5.- Schematic diagram showing recycling of ejected pyroclasts. An ejected clast is initially, quenched, and enveloped in seawater (top right). If the clasts falls back down into the vent it encounters an extreme thermal gradient, flashing seawater to steam and leaving behind NaCl-rich brine or salts (bottom right) on external surfaces and in vesicles. The clast may then be wrapped in juvenile melt and reheated, allowing additional crystallization and Cl and Na diffusion into the clast (left). The clast must then be re-ejected and quenched again to preserve the microcrystalline textures.

8.0. Cl diffusion

Elevated Cl concentrations are limited to within microcrystalline inclusions. Boundaries between inclusions and surrounding matrix are typically sharp indicating very limited or no diffusion into surrounding matrix glass (Fig. 3.4). Inclusion interiors,

however, have consistently high, although fluctuating, Cl concentrations, which suggests either extensive Cl diffusion from pyroclast external surfaces to the interior or diffusion from localized concentrations, such as cracks or vesicles infused with NaCl. We suggest the Cl diffusion initiates from NaCl-rich deposits on crack and vesicle surfaces left behind by boiling seawater. Additional heating of the included pyroclast and NaCl allows diffusion over much shorter distances than would be expected from NaCl on external surfaces to the clast interior (see Appendix A for additional discussion). Additionally, Cl diffusion through cracks and vesicles helps explain the limited diffusion into the surrounding matrix. NaCl deposition may be limited to internal cavities.

Although Cl diffusion rates for molten basalt are known (e.g. Alletti et al., 2007), we cannot adequately use Cl diffusion to constrain timescales of recycling due to our limited understanding of the initial conditions. Unfortunately we do not know the length scale over which diffusion occurs, the original geometry (i.e. diffusion across a plane, radial diffusion into a sphere, etc.), or the temperatures involved; all of which can affect the estimated time scales by several orders of magnitude. Therefore, we constrain reheating time scales using reheating/crystallization experiments.

9.0. Experimental constraints on heating-induced crystallization

Although crystallization is usually studied as a cooling-driven phenomenon, heating of glass to a temperature above the glass transition (but below the liquidus) can also cause crystallization (e.g. Burkhard, 2001). To constrain the kinetics of heating-induced crystallization, we heated samples from below the glass transition temperature

(T_g) of ~690°C (e.g., Giordano et al., 2005) to 1170°C, which we infer to be above the eruption temperature, for variable time intervals.

We characterize crystallization textures by qualitative examination of BSE images of the reheated clasts and map them in temperature-time phase space (Fig. 3.6). The groundmass of starting material (Fig. 3.7) has few microlites but abundant plagioclase microphenocrysts and minor mafic (olivine and pyroxene) microphenocrysts. Microlite crystallization is first observed at temperatures above T_g in samples run for <10 minutes and in <5 minutes at T ≥800°C (Fig. 3.6). Pyroxenes are the first crystal phases to form at temperatures of ~690-1100°C, followed by oxides observed at temperatures >700°C. Plagioclase forms at temperatures >990°C, but was likely introduced below 900°C (Burkhard, 2001). Additionally, plagioclase crystallization was not clearly observed in experimental runs of ≤10 minutes. Crystallization increases with time and temperature (Fig. 3.6). Increased crystallization is observed as larger areas of phase separation and *rapid nucleation*, followed by *dendritic growth* which continues until little or no matrix glass remains (*extensive crystallization*). *Rapid nucleation* textures are characterized by speckled areas of phase separation and the beginning of dendritic growth along existing crystal faces (Fig. 3.7b,c). *Dendritic growth* is most prevalent in localized areas between plagioclase microphenocrysts; areas that presumably were the first to nucleate (Fig. 3.7c,d). *Extensive crystallization* occurs at temperatures of ~1000-1100°C and is characterized by dendritic growth of at all three crystal phases and very little (<10min) or no (>30min) unaffected matrix glass (Fig. 3.7e). At temperatures >1100°C crystallization becomes *oxide-dominated* (Fig. 3.7f), with oxides replacing pyroxenes as the dominant

crystal phase. High temperature experiments (>1150°C) produced numerous oxides growing on the surfaces of microphenocrysts and vesicles. The high temperature experiments lower the viscosity of the matrix glass (Δlog viscosity = ~4Pa s from 690-1150°C; after Shaw, 1972) sufficiently to allow flow; observed as collapsed vesicles, new vesiculation, and reshaping of clasts into fluidal morphologies. The collapsed vesicles formed linear strands of oxides from the converging vesicle walls (covered in oxide microlites-Fig. 3.7f).

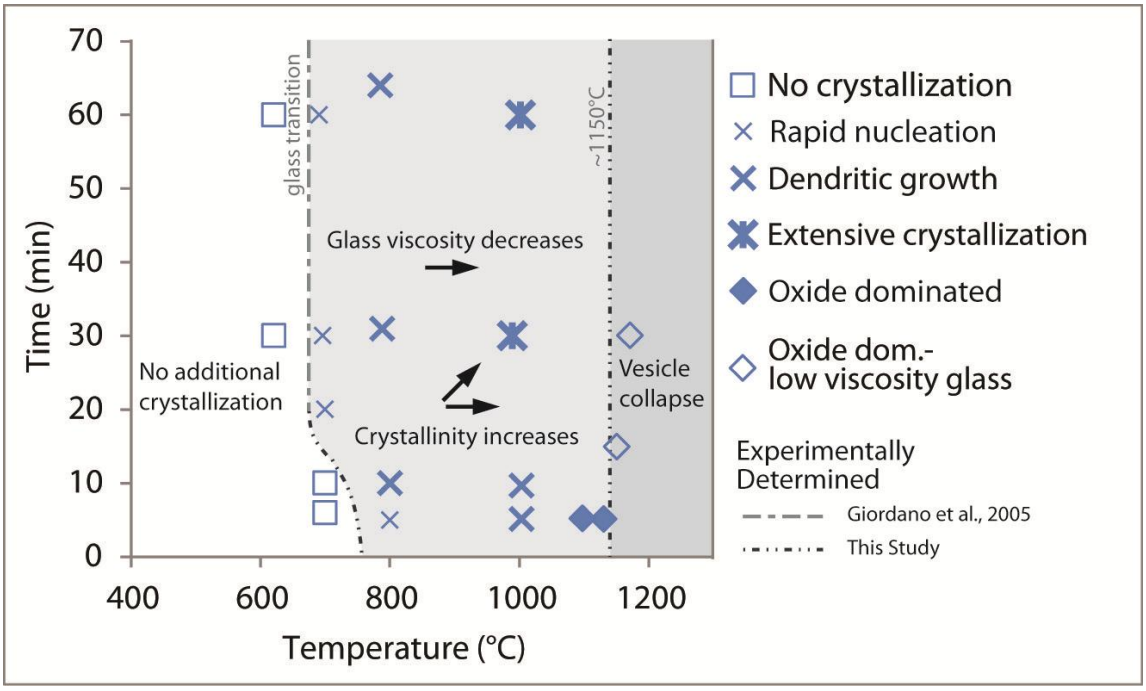

Fig. 3.6- Temperatures and duration of reheating/crystallization experiments. Crystal nucleation was observed above the glass transition temperature (~690°C). Crystallization increased with time and at higher temperatures. Pyroxenes dominate at low temperatures (<1000°C); oxides dominate in high temperature experiments (>1000°C). Plagioclase is observed in experiments of >10min duration at >1000°C. Experiments run at T>1150°C show reorganization of glass as viscosity is reduced, allowing flow (i.e. melting).

The extent of crystallization in basaltic systems is primarily controlled by composition, temperature and pressure, and is driven by undercooling and/or decompression. In a basaltic andesite system at 1atm, undercooling would initially induce crystallization of plagioclase and oxides, followed by olivine and finally pyroxenes (Moore and Carmichael, 1998). The reverse is true for our heating experiments. As the clasts are heated, effective supersaturation decreases and once the eruption temperature is reached, the sample should be at equilibrium with the phase assemblage of the erupted material. Oxides are still crystallizing during the high temperature experiments because of the high fO_2 of our experiments. Crystallization is driven in our experiments by multiple phase supersaturation but is also controlled by the glass viscosity. When clasts are heated above T_g, the matrix glass viscosity is reduced sufficiently to allow some element diffusion, causing crystallization. The first crystal phases to appear likely have the fastest element diffusion rates. For example, in our experiments, pyroxene is the first phase to crystallize, while plagioclase requires higher temperatures (>900°C) and more time (>10min) to crystallize because of larger cations and relatively slower diffusion.

Our reheating/crystallization experiments produced a range of crystal textures from localized crystal nucleation of only one or two crystal phases to extensive crystallization with three crystal phases. Many of the experimental crystal textures observed are comparable to textures found in microcrystalline inclusions from NW Rota-1 samples (Fig. 3.8). The speckled nature of phase separation (Fig. 3.8a,b) was very common in experimental pyroclasts but has only been observed in a couple of NW Rota-1 thin sections. Crystal nucleation and additional dendritic growth on pre-existing crystal

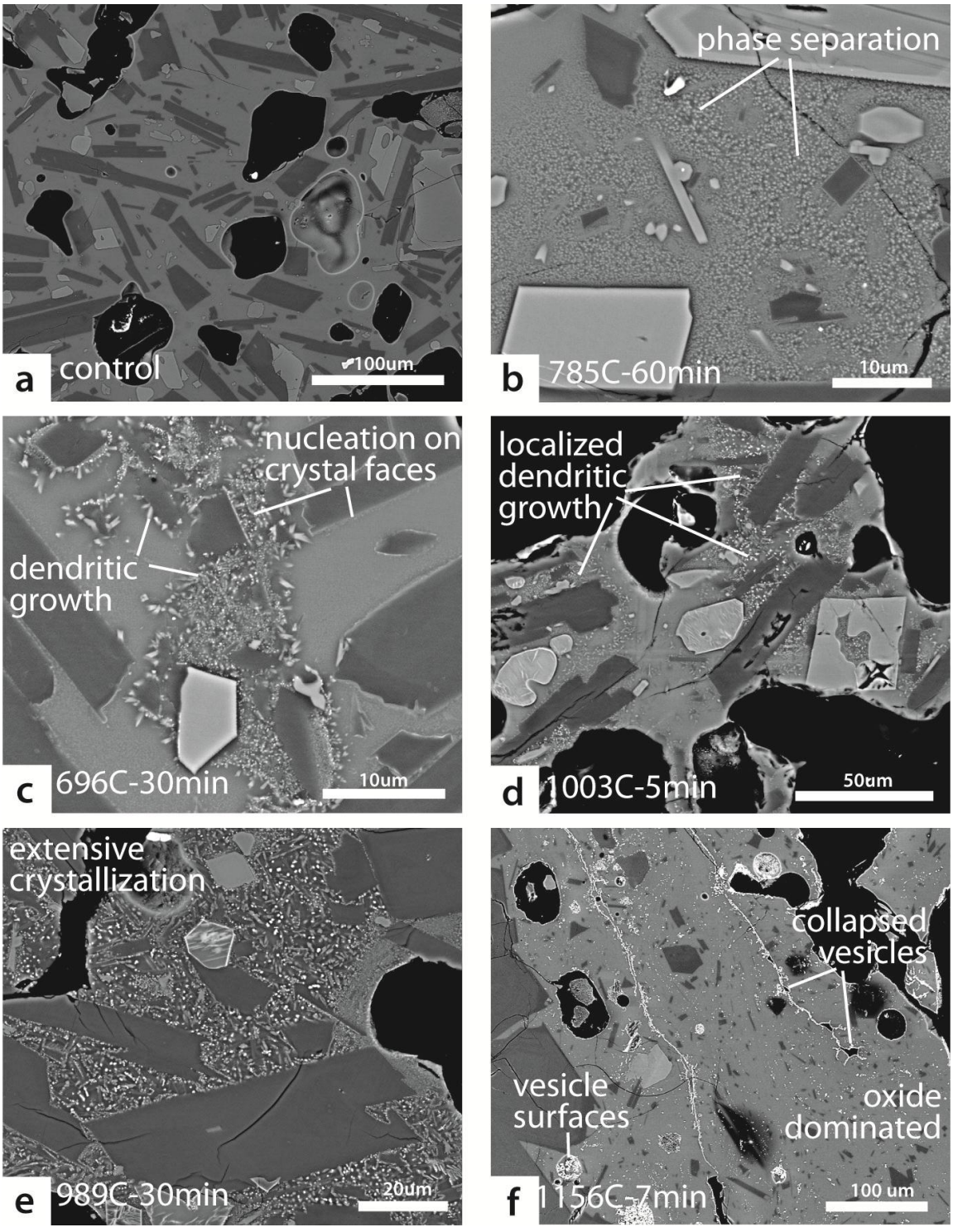
a
control
100um
b
785C-60min
phase separation
10um
c
696C-30min
nucleation on
crystal faces
dendritic
growth
10um
d
1003C-5min
localized
dendritic
growth
50um
e
989C-30min
extensive
crystallization
20um
f
1156C-7min
collapsed
vesicles
vesicle
surfaces
oxide
dominated
100 um

Fig. 3.7.- BSE images of experimental reheating/crystallization textures. (a) Control- no reheating induced crystallization present. (b) Rapid nucleation and phase separation, as glass is heated beyond glass transition the viscosity is reduced allowing element diffusion. (c) Dendritic growth between crystals and on the surfaces of pre-existing crystals. (d) localized dendritic growth, commonly found in areas enclosed by microphenocrysts. (e) Extensive crystallization- no unaffected matrix glass remains; plagioclase and pyroxenes dominate; oxides (white dots) also present. Area around vesicle is 'altered' but no extensive crystal growth present. (f) High temperature experiment- glass has begun to flow, collapsing vesicles. Oxides, growing on vesicle and crystal surfaces, form linear features after vesicle collapse.

faces (Fig. 3.8c,d) is particularly common in both experimental and natural samples, occurring in all experimental runs from T_g to >1000°C and nearly all NW Rota-1 microcrystalline inclusions. Extensive crystallization, where the reheated pyroclast has almost entirely crystallized with very little matrix glass remaining, has not been observed in natural microcrystalline inclusions (Fig. 3.8e,f). However, many microcrystalline inclusions do have three crystal phases (pyroxenes, plagioclase, Fe-sulfides- i.e. Fig. 3.8f), suggesting that although the crystallization textures may differ from our experimental results, the crystallization of these phases occurs at similar temperatures and crystallization rates in natural samples. One additional texture not present in NW Rota-1 inclusions but observed at high experimental temperatures, is oxide-dominated crystallization. Our experimental conditions (atmospheric fO_2) were ideal for the nucleation and growth of Fe-oxides, conditions that are not probable in the submarine environment. However, in the subaerial environment ejected pyroclasts may encounter similar oxidizing conditions. In figure 3.8f a BSE image of a pyroclast from Stromboli, Italy shows a microlite-rich area (right) and a microlite-poor area (left) bordered by a thin strand of oxides. There is also a thick strand of oxides extending from this oxide border

that resembles linear strands of oxides after vesicle collapse in our reheating experiments (Fig. 3.8g). The oxides bordering the microcrystalline matrix suggest it was ejected into oxidizing conditions (air) and recycled, bound by juvenile melt, and re-ejected. Therefore, while Cl assimilation provides a recycling signature in the submarine environment, these oxide strands may provide a signature for subaerial recycling.

At T > ~690°C our experiments show the onset of crystallization within 5 minutes and extensive crystallization occurs within 5-10 minutes if clasts are heated to ≥1000°C (possibly ≥900°C). The extensive crystallization of plagioclase, pyroxenes, and oxides seen in our experiments complement our observations of recycling textures in the natural NW Rota-1 samples. The experiments also provide a tentative guide to interpreting the phases and textures present in recycled areas. Since plagioclase is prevalent within the microcrystalline textures of NW Rota-1, we infer that the recycled pyroclasts were reheated to temperatures >900°C for >10 minutes. Textures, such as flow banding and mingling, of recycled areas suggest temperatures ≥1150°C; the temperature at which vesicle collapse and glass flow occurred experimentally. One caveat is that the experimental samples (from Paricutin, Mexico) and the NW Rota-1 samples have slightly different compositions which may alter the temperature at which each phase crystallizes and when vesicles will collapse (i.e. glass starts to flow). The complex crystallinities and mingling textures observed at NW Rota-1 may require residence times >5-10min and relatively high temperatures (900°C - >1150°C) to produce recycling textures.

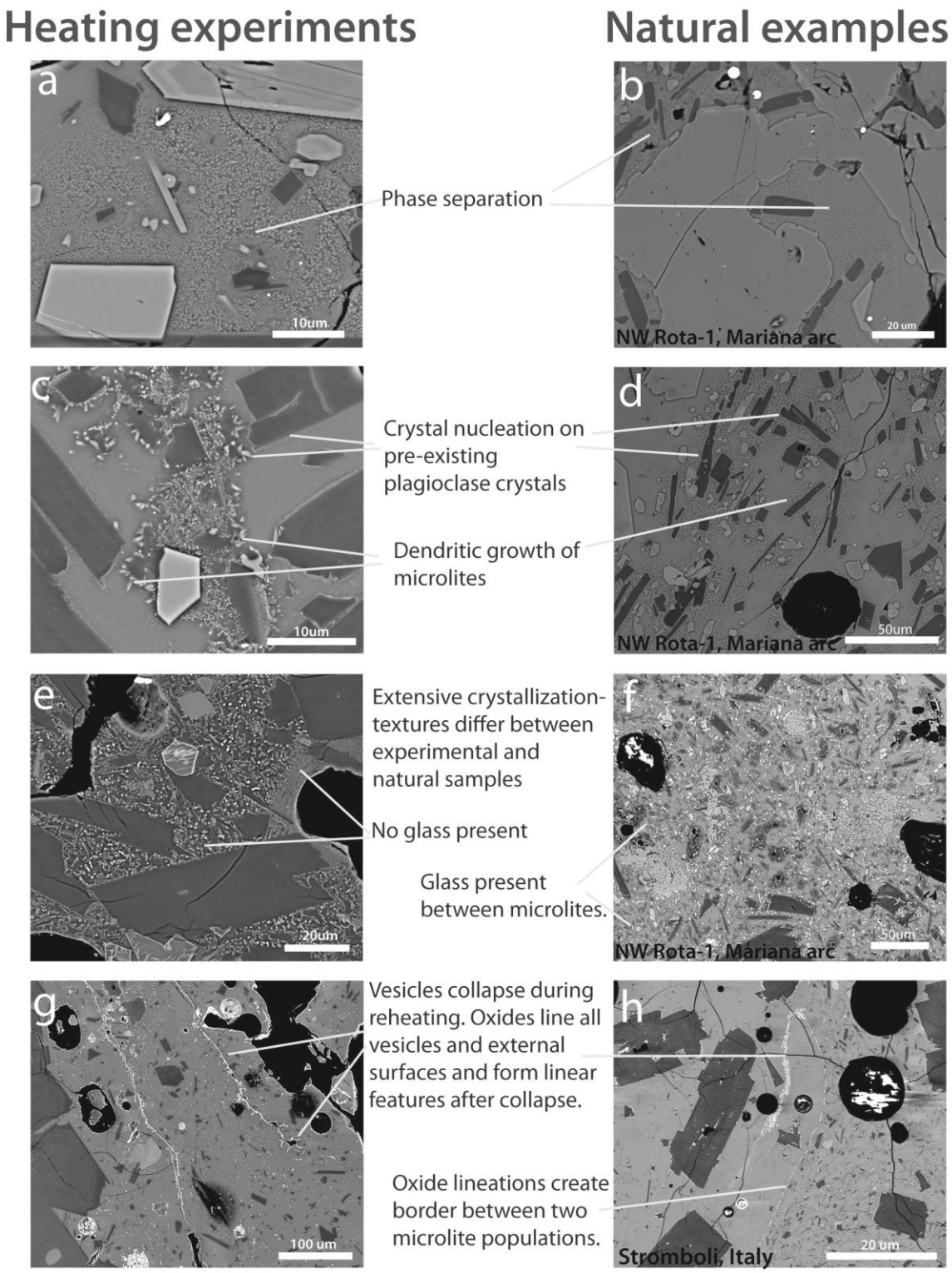

Fig. 3.8.- Comparison of experimental and natural recycling crystal textures.

10.0. Conclusions

Three types of eruptive activity have been identified at NW Rota-1 (two directly observed and one inferred) by groundmass crystallinity and hydrophone data. The full range of groundmass crystallinity at NW Rota-1 is likely due to a combination of magma ascent rate, extent of degassing, and recycling of pyroclasts. The three eruptive types are produced through low (<5m^3/s), intermediate (~5-100m^3/s) and high MER (>100m^3/s) eruptions, which dictates the eruptive style (i.e. effusive, weak strombolian, or energetic explosions). We believe the intermediate activity is due to low-moderate strombolian eruptions and produces recycling of pyroclasts, represented by mingling of microcrystalline and microlite-poor matrix. At NW Rota-1 recycling appears to be limited to low-moderate MER explosive eruptions, caused by insufficient energy to fully expel pyroclasts from the vent, which suggests the same may be true for subaerial volcanoes. However, recycling may be more common in submarine volcanoes because of suppression of the eruptive plumes by hydrostatic pressure, cooling effects, and drag from ambient seawater (Chapter II). Additionally, interaction with seawater during recycling is assimilating Cl and Na into the included material and producing a geochemical signature by which recycling can be identified. Subaerial volcanoes do not have a similar geochemical signature, but may be identified by linear bands of oxide crystals between microcrystalline and microlite-poor areas. We have shown here that minutes to tens of minutes are required to explain observed crystallization, providing an estimated time for recycling of pyroclasts.

Bridge from Chapter III to IV

In Chapters II and III, I discussed direct observations and sampling of explosive mafic eruptions on a submarine volcano (NW Rota-1, Mariana arc). Direct observations of active volcanism are not common, and therefore scientists must infer eruption conditions from the physical and chemical characteristics of eruptive deposits. Chapter IV uses the morphology of a prehistoric lava flow in the Oregon Cascades to infer emplacement conditions.

In the subaerial environment, explosive mafic volcanism commonly produces cinder cones that can be accompanied by extensive lava flow fields. Cinder cones are typically monogenetic and basaltic in composition, but can erupt compositionally heterogeneous intermediate magmas in arc settings. In Chapter IV, I present a high resolution (~1m) map and GIS-based morphological analysis of an intermediate composition lava flow emitted from Collier Cone, a cinder cone on the north flank of North Sister in the Central Oregon Cascades.

CHAPTER IV

EMPLACEMENT CONDITIONS OF THE C. 1600 YBP COLLIER CONE LAVA FLOW, OREGON: A LIDAR INVESTIGATION

1.0. Introduction

Mafic flows are a common form of volcanic activity. While rarely life-threatening, lava flows resurface the landscape and may trigger secondary hazards such as fires (Ogden et al., 1998) or flooding (Thorarinsson, 1979). For this reason, predictive modeling of lava flow emplacement has been a focus of investigation in volcanically active areas (e.g., Crisci et al., 2008). Important input parameters for flow models include lava flux (mass eruption rate) and flow duration, which, in turn, control both the rate of lava flow advance and the final flow length (e.g., Walker, 1973; Kauahikaua et al., 2003). These flow parameters are well constrained for basaltic lava flows from Hawaii and Italy, where eruptions are both frequent and carefully documented (e.g. Walker, 1971; Hon et al., 1994; Kauahikaua et al., 1998; Lipman and Banks, 1987; Wadge et al., 1975; Guest et al., 1987; Calvari et al., 2002; Pinkerton and Wilson, 1994; Pinkerton and Sparks, 1976). Less well constrained are emplacement conditions relevant for flows of intermediate composition, which are both less frequent and more difficult to monitor (exceptions include Naranjo et al., 1992; Borgia et al., 1983; Cigolini et al., 1984; Borgia and Linneman, 1990).

An alternative to making direct measurements on active flows is to develop methods to infer emplacement conditions from the morphologies of solidified flows.

Published field measurements of flow features are limited, primarily because of the difficulties inherent in collecting accurate data on flows that are both rough and spatially extensive. However, recent advances in airborne and satellite remote sensing techniques allow the production of 3D high resolution (<1m) topographic data, revolutionizing geomorphic analyses (e.g., Woolard and Colby, 2002; Perron et al., 2003; McKean and Roering, 2004; Roering and Gerber, 2005; Slatton et al., 2007). In particular, the development and increasing availability of Airborne Laser Swath Mapping (ALSM), and, more specifically, airborne Light Detection And Ranging (Lidar), is changing the way that we view volcanic landscapes (e.g., Cashman et al., in review). Lidar data are particularly useful in vegetated regions, where post-processing of the data provides bare-earth topography, often with sub-meter resolution.

Here, we use Lidar data from the c. 1600 ybp basaltic andesite Collier Cone, OR lava flow field to constrain its emplacement history. Lava flow emplacement and resulting morphologies are controlled by many factors including viscosity, yield strength, effusion rate, surface crustal strength, pre-existing topography and slope (Walker, 1973; Hulme, 1974; Kilburn and Lopes, 1988; Kerr and Lyman, 2007). In measuring the morphology of the Collier lava flows we hope to quantify flow parameters and use the measured parameters to constrain emplacement conditions (e.g. effusion rate and eruption duration) that cannot be directly measured. First, we use Lidar-generated topography to target field work and sampling that allow us to map the individual flow units that comprise the flow field. Second, we extract measurements of flow area and thickness from Lidar digital elevation models (DEMs) that allow us to refine estimates of flow

volume. Third, by comparing along-flow measurements of channel and flow widths with model predictions (Kerr et al., 2006) we constrain the range of effusion rates operative during the eruption and, in doing so, estimate the eruption duration. Finally, we use surface analysis techniques (e.g., Booth et al., 2009) to constrain the dimensions (amplitude and wavelength) of surface folds developed within the lava channels; we then compare our results to published measurements from a wide range of flow types, to evaluate the potential use of flow surface morphologies for inferring the composition of planetary lava flows (e.g., Fink, 1980; Gregg et al., 1998). Taken together, these analyses not only constrain the emplacement conditions of a specific andesitic lava flow but also allow us to evaluate the flux and duration that might be expected for future cinder cone eruptions in the central Oregon Cascades.

2.0. Background

2.1. *Lidar and lava flows*

Lidar data can provide new insight into lava emplacement mechanisms and new opportunities for lava flow hazard and risk assessment (e.g., Cashman et al., in review). For example, Lidar-generated digital elevation models (DEMs) allow detailed mapping of individual lava flow units and flow facies changes (Favalli et al., 2010a) and extraction of morphometric parameters that can be used to constrain some physical properties of the lava (Pyle and Elliot, 2006; Ventura and Vilardo, 2008). Lidar mapping of active lava flows provides both snapshots of active lava channels (Mazzarini et al., 2005) and time-series analysis of flow features (Favalli et al., 2010b) that can be related directly to

measured lava rheologies and effusion rates (Harris et al., 2007). Lidar DEMs are being used to create hazard and risk assessment maps of active volcanic regions (e.g., Favalli et al., 2009b; Hofton, et al., 2006). Lidar also provides new ways of characterizing lava flow surfaces. For example, Lidar intensity varies with flow surface texture, a function of both emplacement style and flow age (e.g., Mazzarini et al., 2007). Multi-temporal Lidar (repetitive data collection of same area) provides critical information not only on volume changes (effusion rates) of active flows but also syn-eruptive volcano deformation (Marsella et al., 2009), and morphologic changes in scoria cones (Fornaciai et al., 2010) and lava flow fields (Favalli et al., 2010b).

The studies outlined above illustrate a range of questions that can be addressed using high resolution 3D topographic datasets of active volcanic landscapes. However, most studies to date have focused more on technique development (proof-of-concept) than on attempts to relate flow morphology directly to emplacement mechanisms. Exceptions are studies by Pyle and Elliot (2006) of Nea Kameni lava flows (Santorini, Greece) and by Ventura and Vilardo (2008) of the 1944 lava flow from Vesuvius volcano, Italy. We build on these studies by exploiting the ease and accuracy of extracting simple morphologic measurements from high resolution Lidar DEMs using GIS methods to demonstrate ways in which these measurements can be used to analyze emplacement of lava flows from Collier Cone, Oregon.

2.2. *Collier Cone, OR*

Collier Cone is one of the youngest (1600 ±100 ybp; Sherrod et al., 2004) of the Holocene cinder cones in the central Oregon Cascades. It is situated on the north flank of North Sister stratovolcano at an elevation of 2296 m (Fig. 4.1). Both the youth and elevation of the vent have left the associated lava flows sparsely vegetated over ~2/3 of its length (Fig. 4.2a). Prior work on the Collier Cone lava flow has shown that the flow field is comprised of several distinct flow units that range in composition from basaltic andesite to dacite (Baker and McBirney, 1986; Schick, 1994). In this study we build on the work of Schick (1994) by using bare earth Lidar-generated DEMs both to refine the flow mapping (particularly in the distal, more vegetated parts of the flow) and to quantify morphologic changes along the flow length, with the specific goal of estimating flow emplacement parameters, such as effusion rate and eruption duration, that are necessary for volcanic hazard assessment in this area.

The Collier Cone lava flow field is composed of two main lobes. The primary lobe flowed west 13.6km down the glaciated valley of White Branch Creek, damming both Spring Lake and Linton Lake (Fig. 4.2) where it blocked tributaries to the White Branch. The western lobe is topographically constrained along the southern margin for most of its length; the northern margin is topographically confined at lower elevations, where it is funneled south of c. 13,000 ybp Sims Butte and into the White Branch glacial valley (Fig. 4.1). The western lobe is channelized along most of its length; the presence of multiple inset levees within the main channel suggest declining effusion rates through time. Near the cone, the western lobe is covered by a later flow unit, which flowed 4.6km

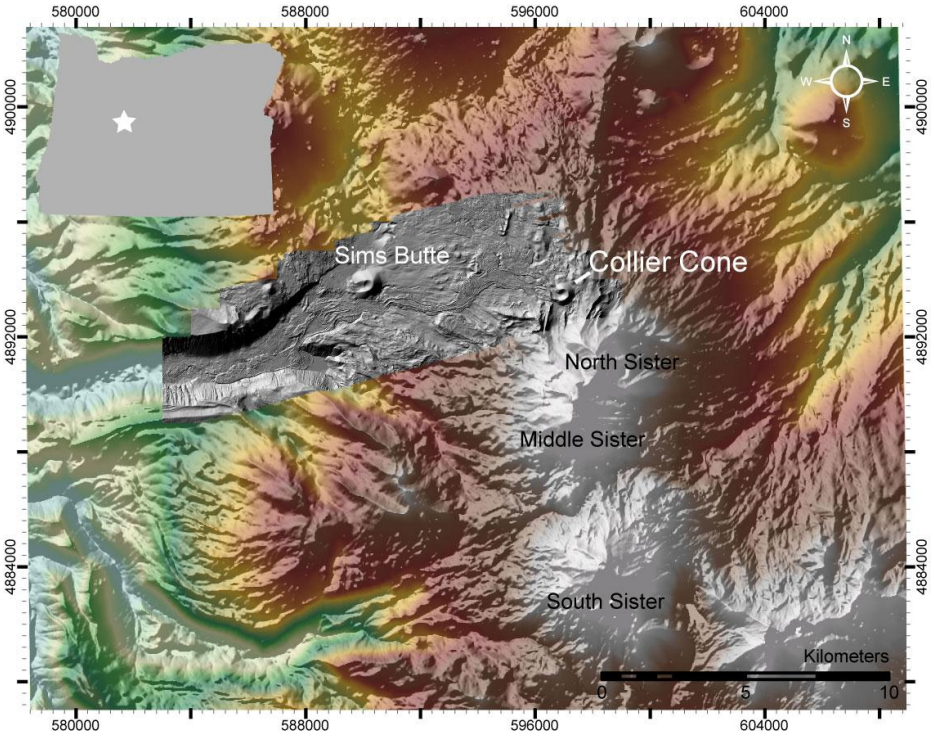

Fig. 4.1.- 10m DEM overlain on shaded relief map of Three Sisters Volcanic Complex, High Cascades, OR. Inset shows location (star) within the state of Oregon. Study area is designated by grey shaded relief map (gridded at 1m) of Collier Cone lava flow field. Latitude and longitude coordinates are in UTM Zone 10 projection.

to the northwest. This lobe is channelized only near the vent, where it was topographically confined by the vent itself. Glacial outwash covers much of the lava within cone. The lava confined within the channels has well developed surface folds, as do most of the lobate extrusions along the flow margins.

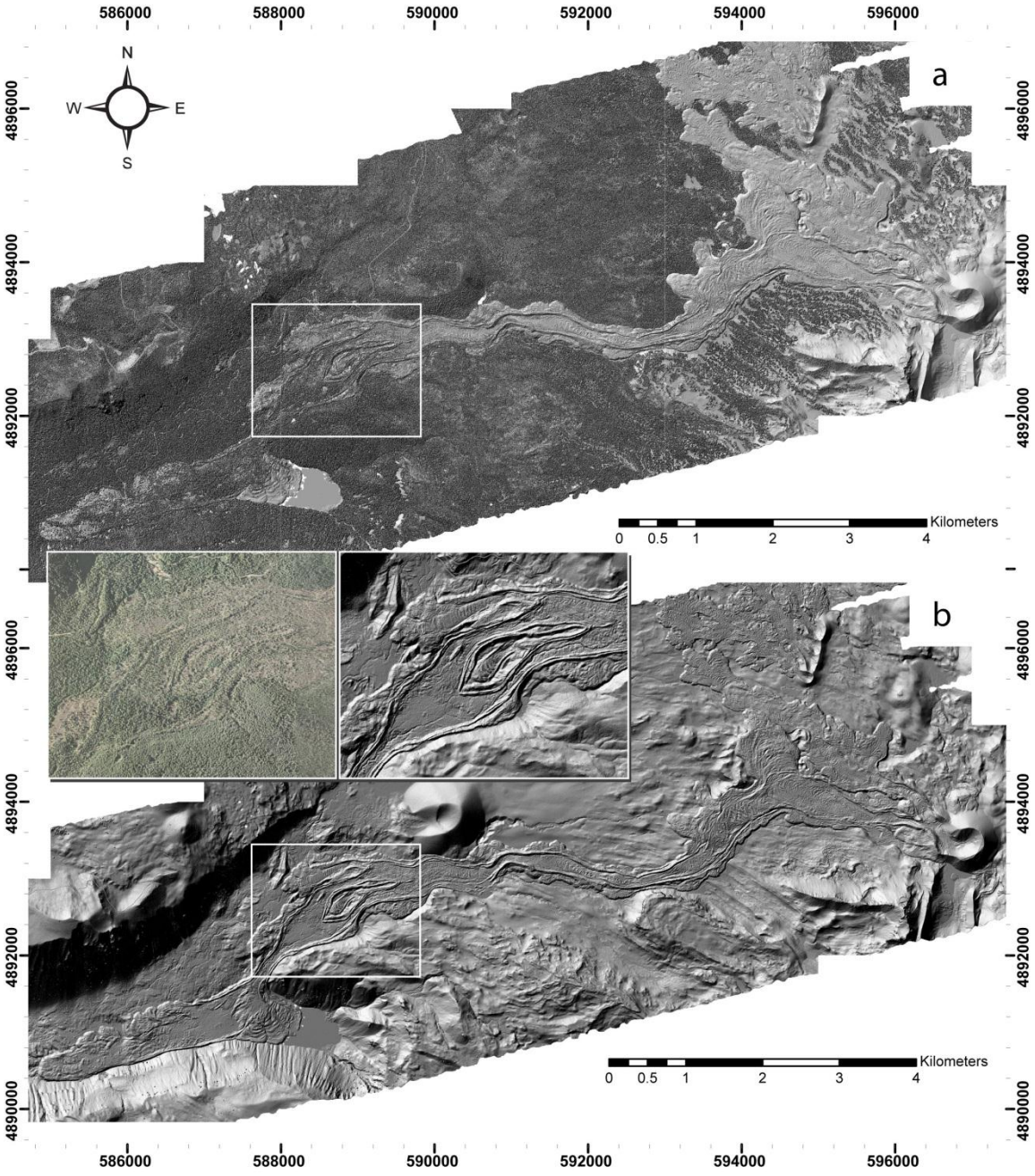

Fig. 4.2.- Shaded relief maps of Collier Cone lava flow field; gridded at 1m resolution. (a) unfiltered shaded relief map, displaying vegetation cover on the lava flow and surrounding glaciated terrain. (b) filtered shaded relief map with vegetation removed. Inset includes an orthorectified photo (left) and a close up shaded relief (right) of lava flow bifurcation (white rectangle). Complexity of this area was unknown before retrieval of lidar. Coordinates are UTM Zone 10 projection.

3.0. Methods

Key to this study is high resolution digital topographic data acquired by airborne laser altimetry (Lidar). The Lidar survey of the Collier lava flows used an Optech Gemini Airborne Laser Terrain Mapper (ALTM). Operation of the ALTM and all initial data processing were completed by the National Center for Airborne Laser Mapping (NCALM). The Gemini ALTM specifications, data collection and processing techniques are described by Shrestha (2007). ALTM specifications for the Collier lidar data collection are listed in Appendix A. The 55.2km^2 of Lidar data were collected at Collier Cone on July 28, 2008 using 01:05:00 hrs of total laser time. Initial processing – removal of errant data points and ground classification – was completed by NCALM. Post-processing included gridding all GIS layers at 1m spatial resolution within the NAD83 UTM Zone 10 coordinate system. Figure 4.2 shows gridded shaded relief maps of the study area with both unfiltered (a) and filtered (b-vegetation has been removed) layers.

3.1. *Field work and mapping of lava units*

Mapping the Collier flow field required a combination of field work, ground-based GPS, and Lidar-derived maps. Morphologic features were mapped directly from shaded relief and slope maps. Importantly, these maps generated from the bare earth Lidar exposed flow termini, morphologies and complexities that were previously hidden from view (Fig. 4.2b). For example, the flow bifurcation near Sims Butte (Fig. 4.2b, inset) and the flow terminus of Unit 2 were identified only upon retrieval of the bare earth Lidar. Identification of individual flow units required additional field mapping, as they

were distinguished more by crystallinity and compositional variability than by morphology. In particular, areas with multiple lava units and less pronounced inset levees (e.g., near the cone, as the flow widens after the breach) were difficult to distinguish with the lidar data alone. Field mapping and sampling locations were mapped on the Lidar shaded relief maps using data from a hand held GPS unit and ArcMap. We focused particularly on identifying flow margins and collecting samples along transects normal to flow direction and within the cone. Transects close to the cone were chosen to coincide with locations where all lava units identified by Schick (1994) were present; in more distal areas, we chose transects near inferred flow unit termini and in areas of complex flow features (Fig. 4.3). In the field, flow contacts were identified by changes in flow morphology as well as changes in the abundance of both phenocrysts and xenoliths. During mapping, we collected 162 samples for hand specimen, thin section, and geochemical analysis (Fig. 4.3). 50 samples were sent to the GeoAnalytical Lab at Washington State University for ThermoARL x-ray fluorescence (XRF) spectrometer analysis of all major and trace elements. These data were used in conjunction with 46 bulk rock compositions (analyzed for major and trace elements at the University of Oregon using a Varain 125 atomic absorption photospectrometer) and locations from Schick (1994) to create the flow map shown in Figure 4.3.

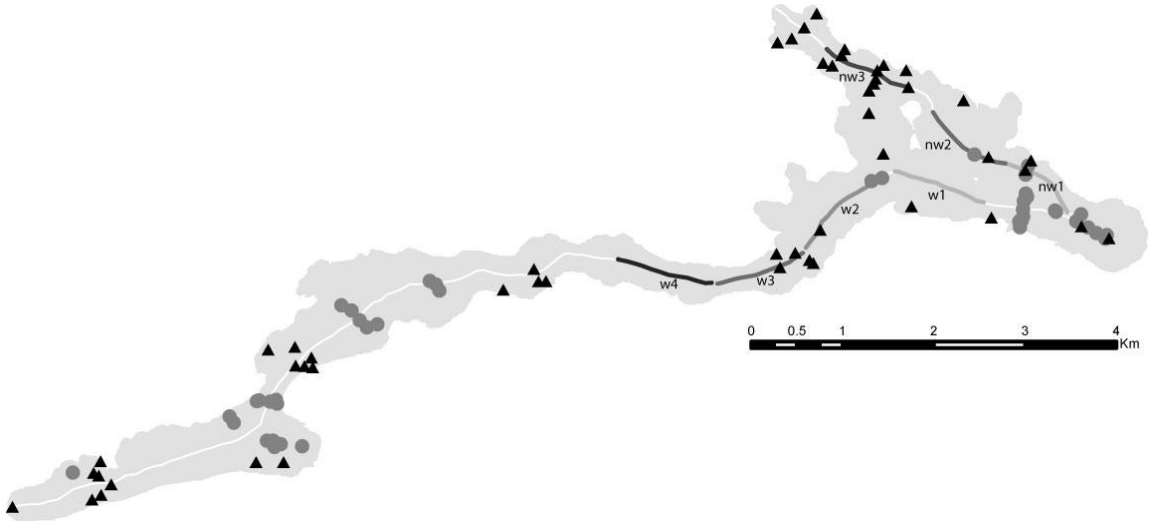

Fig. 4.3.- Lava flow field polygon with sample locations for all analyzed for bulk compositions. Circles are samples collected for this study. Triangles are analyses from J. Schick (1994). White lines indicate full along channel profiles for the west and northwest lava lobes. Short 1000m profile segments, used for DFT analyses, are indicated by grey tones (light grey through black) and are labeled w1-w4 for the western segments and nw1-nw3 for the northwestern segments.

3.2. *GIS analyses*

We used GIS analysis to measure lava morphologies by two methods: (1) extraction of discrete 2D lava flow profiles and (2) extraction of measurements from within regularly spaced boxes that extended along the entire flow field (Fig. 4.4a). Lava profiles were created along the centerlines of both channels to estimate the gradient over which the flows traveled and to measure the amplitude and wavelength of surface folds. Profiles normal to the flow direction allowed measurements of levee height, flow and channel widths, and flow thicknesses (Fig. 4.5). In total, 53 normal profiles were created along the west lava lobe and 16 along the northwest lobe, representing an average spacing of 250m.

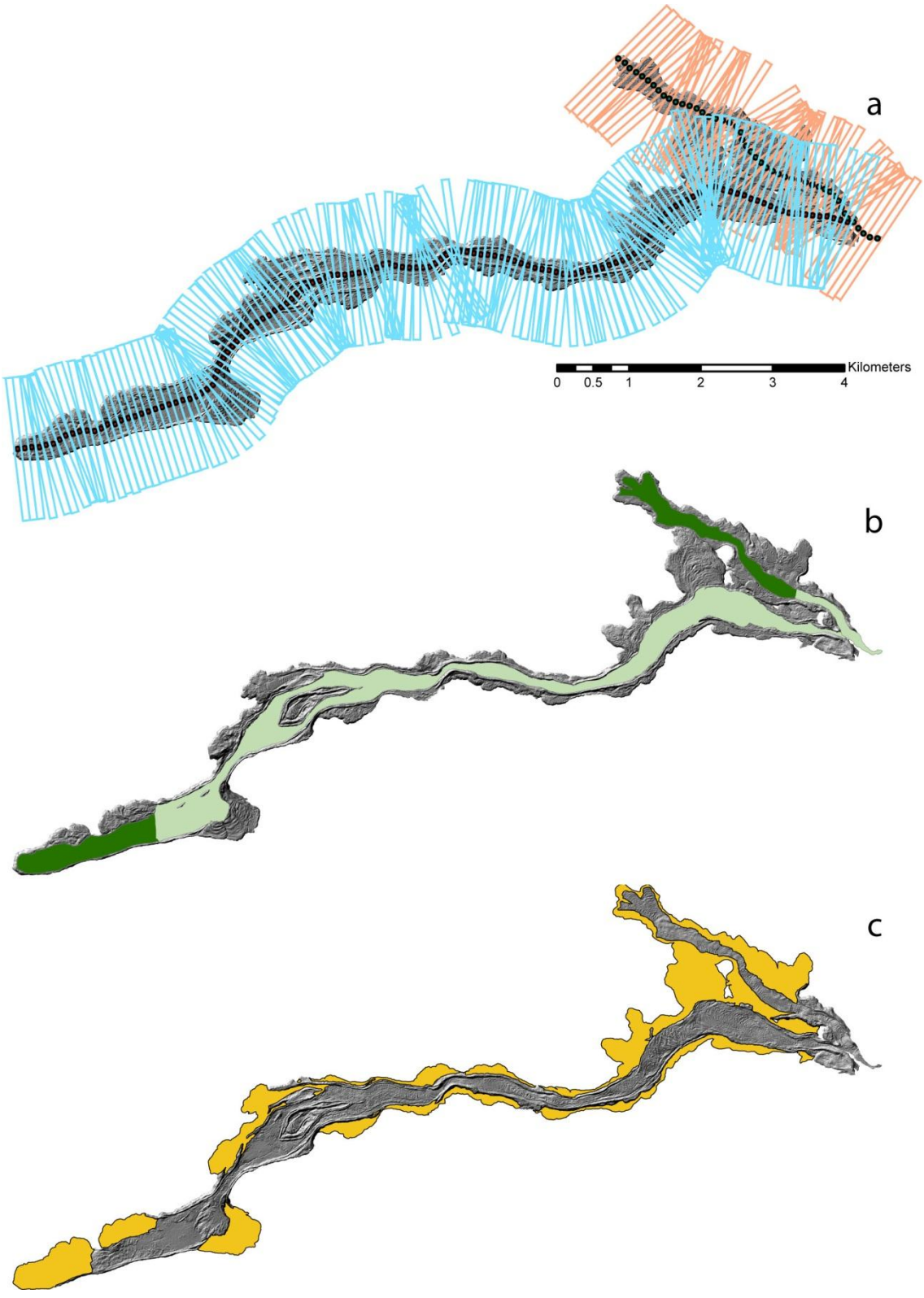
a
Kilometers
0 0.5 1 2 3 4
b
c

Fig. 4.4.- Polygons and swath boxes. (a) two series of swath boxes (over the west and northwest lava lobes) used in ArcGIS statistical analysis of the lava flows. The boxes are 2000m long and 100m wide and oriented normal to flow direction. (b) green polygons represent area analyzed for channel morphology measurements. Channels with well-developed levees are shaded in light green and channels with discontinuous levees are dark green. (c) orange polygons represent the flow margins. This area was analyzed for flow thickness measurements.

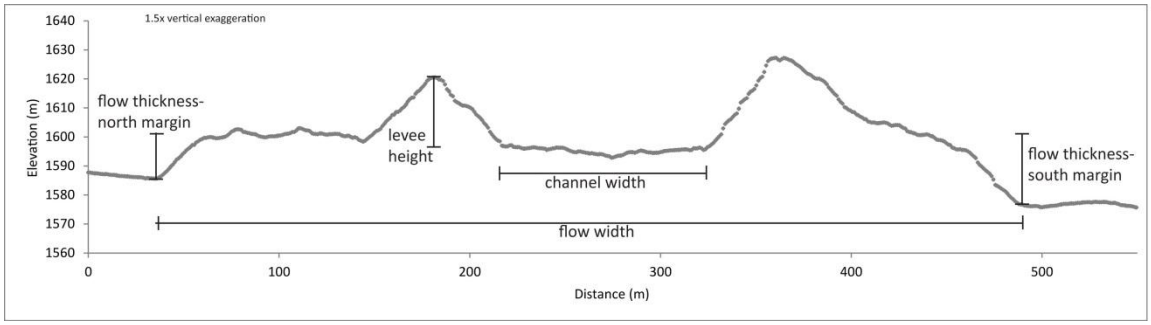

Fig. 4.5.- Example lava profile; digital slice of elevation data normal to the flow direction. Dimensions of lava morphologies measured (channel width, flow width, flow thickness, levee height) are indicated. Profile has 1.5x vertical exaggeration.

To analyze the entire flow field, we developed a GIS-based method for extracting average channel width, levee dimensions, and flow margin thickness from contiguous 100m segments along both channels. To do this in ArcMap, we constructed rectangular 'boxes' (2000m long, 100m wide) along the entire length of both flow lobes and oriented normal to the flow direction (143 boxes covered the western lobe, 47 boxes covered the northwestern lobe; Fig. 4.4a). The centroid (geometric center) of each box was aligned with the centerline of the channel. Polygon shapefiles of the flow field, the two flow lobes, the lava channels, levees, and outermost flow margins (Fig. 4.4) were constructed using ArcMap. Because multiple sets of levees are present along most of the flow field, the channel polygon includes only the area bracketed by the innermost set of levees (Fig.

4.4b). The polygons were used as masks to extract gridded rasters for the relevant area. The 100 x 2000m boxes were overlain on the raster polygons and used to extract statistical data. Channel and flow widths were calculated from these data by averaging the extracted data for each 100m segment. Flow thickness was determined by analyzing the outer margins of each flow lobe and subtracting the mean margin elevation from the minimum elevation within each box. Thicknesses were measured separately for flow margins on both sides of the channel (i.e. north and south for the western lobe) to compensate for both slope changes and topographic interactions (Fig. 4.4c). The total flow volume was calculated by summing the average volume measured for each box. Although this method of estimating volume does not account for across-flow variations in thickness caused by complex channel and levee structures, it is more accurate than commonly used methods that apply a single average thickness to the entire flow (e.g., Coltelli et al., 2007; Cashman et al., in review). Slope measurements were determined within the lava channel from the elevation data within each box using a custom Matlab script. For each box, we fit a least squares planar surface to calculate the down slope gradient. Although this yields a slope for the existing channel rather than the pre-existing topography, we suggest that it supplies a reasonable approximation to the surface over which the flow traveled. Procedures for morphologic measurement extraction are in Appendix B and Matlab script for determining slope is in Appendix C.

3.3. *Discrete Fourier transforms*

To determine the characteristic scale of prominent surface folds, we selected representative 1000m along-channel segments – four from the west lobe and three from the northwest lobe (Fig. 4.3) to cover a range in channel width, surface fold expression (i.e. larger vs smaller folds), and distance from the vent. All profiles were detrended to reduce the effect of slope and then analyzed using two discrete Fourier transform (DFT) analyses in Matlab: (1) a spectrogram function and (2) an averaged modified periodogram. The spectrogram, often used for time-dependent acoustic signal analyses, is computed using a sliding window and displays the spectral density over time (or distance) for a data sequence. We used a 100m (Hann) window with 50% overlap; the small windows minimized the local slope effects, which typically vary over several hundred meters. Spectrograms of lava profiles typically display changes in surface topography with distance. Quasi-periodic topographic signals of the lava are represented by fluctuations in power spectral density over a range of frequencies (or wavelengths), thus along-channel spectrograms show changes in the location, wavelength, and intensity of surface folding as a function of the distance traveled.

For a more detailed analysis of the surface folds we measured the wavelengths and amplitudes for each representative segment by DFT analysis, which can be used to determine the mean-squared amplitude and spatial scale of periodic and quasiperiodic surface features (Booth et al., 2009; Perron et al., 2008). Our DFT analysis measured the power spectral density (in units of amplitude squared) of the input profile (elevation with distance) using an averaged modified periodogram (pwelch) and a 200m window

(Hamming) with 50% overlap. The DFT periodograms produce 1D arrays of spectral density over a range of spatial frequencies, which describe the amplitude and spatial scale (wavelength) of lava surface topography. To identify characteristic wavelengths of lava surface morphology the DFT analyses were normalized by dividing the spectral power densities of representative segments by their power law trendline. Because the lava surface features are not perfectly sinusoidal or periodic, amplitudes were also measured by hand from lava profiles for comparison. Matlab scripts for spectrogram and DFT analyses are in Appendix C.

4.0. Results

The Collier lava is a complicated, heterogeneous flow field. The detailed mapping presented here would not have been possible without extensive sampling and high resolution field maps. Here we discuss the Collier lava units, our extracted flow morphology measurements, and relationships between morphologies.

4.1. *The Collier Cone lava flow*

The Collier Cone lava flow is composed of two main lobes that traveled to the west and northwest; the western lobe was formed by at least three separate flow units (labeled Units 1-3), while the northwestern lobe comprises a single (although compositionally variable) unit (Unit 3; Fig. 4.6). The western lobe has a calculated volume of ~0.14km^3 and the northwest lobe is ~0.03km^3, for a total volume of 0.17km^3.

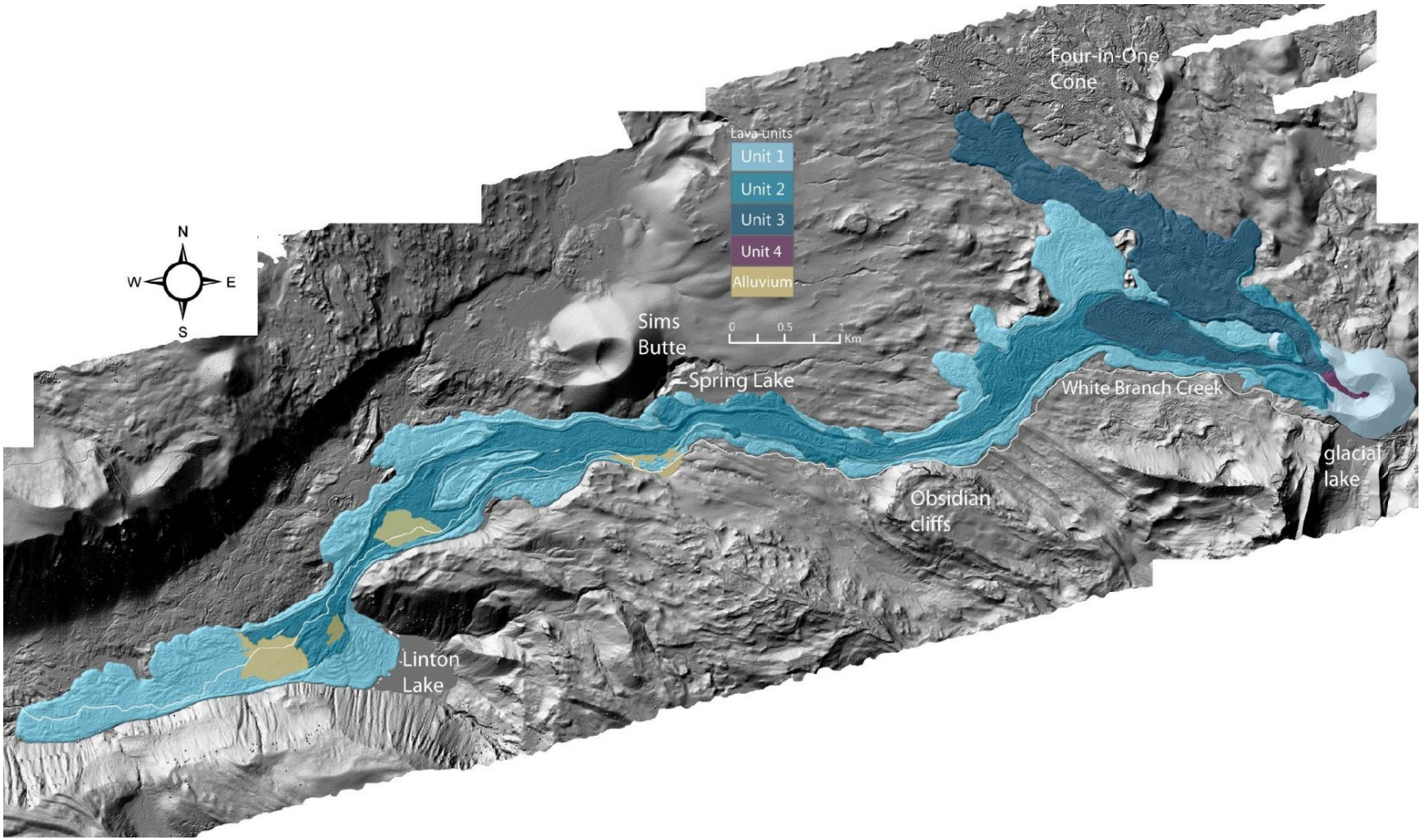
Four-in-One
Cone
Lava units
Unit 1
Unit 2
Unit 3
Unit 4
Alluvium
N
W
E
S
0
0.5
1
Km
Sims
Butte
Spring Lake
White Branch Creek
glacial
lake
Obsidian
cliffs
Linton
Lake

Fig. 4.6.- Map of the Collier Cone lava flow field including lava units, cinder cone, and alluvial deposits. The cinder cone and rafted cone material are very light blue. Lava units are: Unit 1- light blue , Unit 2- medium blue , Unit 3- dark blue , Unit 4- magenta (confined within cone). Topographic features effecting the lava flow, during and after emplacement, are labeled.

Flow units are defined by variations in crystallinity, xenolith content, and composition. Unit 1 (earliest) is andesitic (57.5-60.3wt% SiO_2) and ranges from nearly aphyric (<5%) to moderately crystalline (20%); plagioclase is the dominant phenocryst phase and is accompanied by scarce olivine (<5%). Unit 2 is more crystalline (20-30%) and is distinguished by the abundance (≤15%) and large size of the olivine phenocrysts. Unit 2 also has a large range in bulk composition (55.4-58.9wt% SiO_2) that can be attributed to the variable olivine content. Unit 3 is more evolved silicic andesite (59.0-61.3wt% SiO_2) with 15-20% plagioclase and 5-10% olivine and contains silicic xenoliths throughout. Unit 4 is a small dacite flow (63.3-65.1wt% SiO_2) that is confined within the cone. This unit is crystal-poor (<10%) with few silicic xenoliths but numerous mafic inclusions.

The spatial distribution of individual flow units records the temporal evolution of the eruption. Unit 1 traveled west for 13.6km down the White Branch valley. A small lobe of Unit 1 also traveled to the northwest from the main channel (~2.5km from the vent) and spread around vents from the Four-in-One eruption (c. 1900 ybp; Sherrod et al., 2004), immediately north of the Collier flow field. Unit 2 lava apparently ponded within the vent before overtopping and breaching the cone to the west and northwest, respectively. Evidence for this phase of activity can be found in a short lava lobe on the west flank of the cone (Fig. 4.6) and in large (up to 2m) fluidal bombs of Unit 2

composition that lie along the western crater rim. Unit 2 bombs are also present on top of a cone segment that was rafted ~700m to the northwest when the cone was breached. Unit 2 lava then focused within the Unit 1 channel, forming inset levees, overflowing the channel in multiple locations east of Sims Butte, and terminating by Linton Lake (Fig. 4.6). To the northwest, Unit 2 lava can only be identified in flow levees near the cone. Unit 3 is silicic andesite in composition and produced two lobes, one that followed the channels of the two previous units to the west for ~2.5km and another that extended 4.6 km to the northwest. The western extent of Unit 3 was mapped from aerial photographs using its darker color; the terminus was confirmed by field checking and sampling. A very small dacite lobe within the cone comprises the final stage of the eruption.

4.2. *Flow morphology*

The succession of four flow lobes complicates interpretation of morphologic characteristics of the Collier Cone flow, particularly because the three major units traveled at least part way through the same western channel. However, the flow unit map (Fig. 4.6) shows that, throughout most of the western flow lobe, the earliest unit (Unit 1) defines the flow width. Unit 2 is mostly confined within Unit 1 channels except where there are channel overflows (east of Spring Lake). Thus much of the innermost (and most easily measured) western lobe channel was established during the Unit 2 eruptive phase. In contrast, the northwestern flow is formed almost exclusively by Unit 3 lava.

Along the Collier Cone western lava lobe, total flow widths vary from 130-1440m while inner channel widths vary from 30-490m. Both channel and flow widths vary with

distance from the vent, local slope, and surrounding topography (Figs. 4.7a,b,d). Channel widths nearly parallel the flow widths, but have lower absolute variability (i.e standard deviation: flow widths = 235m, channel width = 120m). As expected, flow and channel widths vary inversely with gradient (Fig. 4.7b), such that steeper slopes produce narrower flow and channel widths and lower gradients allow the lava to spread laterally. The narrowest channels are present near the cone (where the lava breach occurred), near Obsidian Cliffs, east of Sims Butte, and north of Linton Lake. These locations represent the steepest slopes measured, mostly ranging from 5-12.5°, and are all regions where the flow was partially or completely confined by pre-existing topography (Fig. 4.6, 4.7). The very steep slopes and narrow channel near the cone (9-23.5°) were formed when lava breached the cone.

Measured flow margin thickness ranges from <5–32m, correlates with flow width (Fig. 4.7c), channel width, and is generally inversely proportional to slope. The northern margin of the western lobe is mostly unconfined by topography and represents the most representative thickness measurements. The southern margin of the western lobe is bordered by White Branch creek near the cone, and is confined by Obsidian Cliffs and a steep glacially carved slope for the proximal 1/3 of the flow (Fig. 4.6). Because thickness was measured using the difference between average and minimum elevations (i.e. from the base to the crest) of the lava margin, thicknesses measured in areas of steep confining topography are minima. Flow margins are over thickened where Unit 2 lava overflowed the channel and near the flow front, where the distal toe of the flow may have experienced some amount of inflation (Fig. 4.7d).

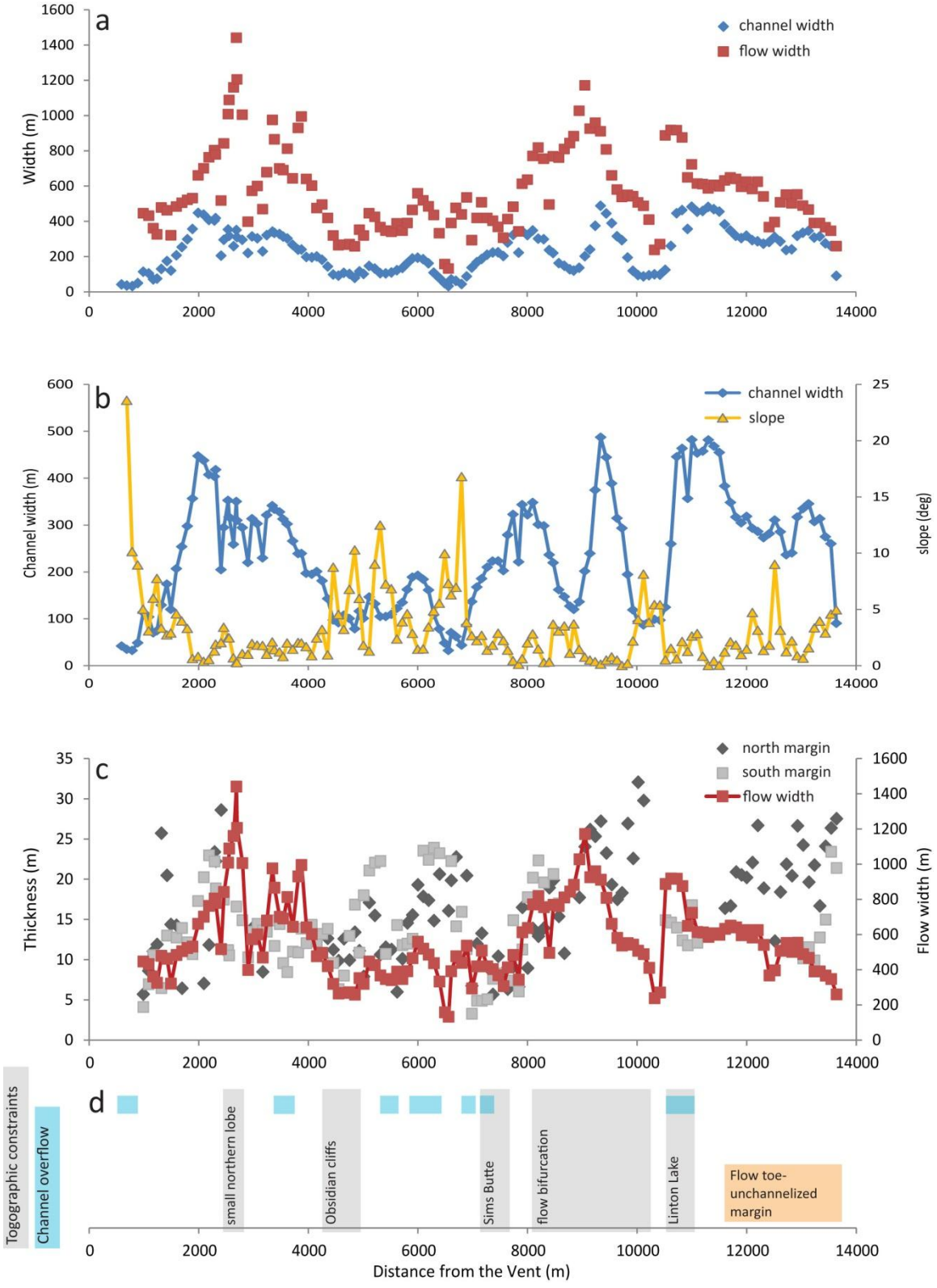
a
channel width
flow width
Width (m)
b
channel width
slope
Channel width (m)
slope (deg)
c
north margin
south margin
flow width
Thickness (m)
Flow width (m)
d
Togographic constraints
Channel overflow
small northern lobe
Obsidian cliffs
Sims Butte
flow bifurcation
Linton Lake
Flow toe-unchannelized margin
Distance from the Vent (m)

Fig. 4.7.- Flow morphology box measurements, plotted with distance from the vent. (a) channel and flow widths are coupled. Flow widths have a wider range due to branching lava lobes, flow bifurcation, channel overflow, and topographic constraints. Both channel and flow widths are inversely correlated with local slope. (b) channel width is inversely correlated with increased slope. (c) Flow thicknesses appear to correlate with flow width, allowing for a few deviations. These deviations (plotted in d) occur in areas of topographic constraint (grey regions), channel overflow (blue boxes), and the flow toe (orange region).

The Collier lava flows interacted with surface water where the western lobe dammed Spring Lake and Linton Lake (Fig. 4.6). Of note is the region of particularly complex flow structures west of Spring Lake, ~8km from the vent (Fig. 4.2, inset). Here the flow transformed from a single well-defined channel to multiple channels; specifically, the flow appears to have bifurcated around an early (stalled) flow lobe. As there are no obvious topographic highs (i.e. kipukas) present at this location, it seems plausible that standing water may have stalled the lava advance. The creek feeding what is now Spring Lake pre-dates the Collier lava flows and presumably ran through this complex area, funneled by Sims Butte and the steep terrain to the south. Currently, Spring Lake is fed seasonally by the creek and drains underneath the Collier lava to emerge further down valley. We also surmise that there was water where Linton Lake is today, possibly dammed by the earlier Sims Butte lava flow. We infer the presence of water from the limited advance of Unit 2 lava into the glacial trough that currently hosts Linton Lake. The trough is supplied by two glacially fed creeks that also pre-date the Collier lava flows. We further speculate that water quenching may be responsible for the development of well-defined surface folds at the margins of Linton Lake.

In this section, we have demonstrated that flow width, channel width, and flow thickness are all inversely correlated with slope. The observation that both flow width and flow thickness vary with slope is important, as most existing (1-2D) flow models hold either one or the other constant. We have also shown that local flow morphology is strongly influenced by topographic features and, potentially, by surficial water. The observed relationships between flow width, channel width and slope (Fig. 4.7) are consistent with observations from analog experiments (e.g. Gregg and Fink, 2000) and suggest that morphologic measurements of lava flows can be combined with parameterizations derived from analog models to constrain emplacement conditions.

5.0. Discussion

5.1. *Flow emplacement conditions*

Determining the emplacement conditions of a prehistoric lava flow from preserved flow morphologies requires development of a theoretical framework for understanding coupling between the fluid dynamics and thermal evolution of the flowing lava. Analog experiments (Fink and Griffiths, 1990; Griffiths and Fink, 1993, 1997; Gregg and Fink, 2000; Griffiths et al., 2003; Lyman et al., 2004; Lyman and Kerr, 2006) permit simple parameterizations between flow advection and cooling because analog materials typically have a single solidification temperature (unlike lava flows, which solidify over a large temperature range).

Testing these models has proved difficult, however, because of the limited availability of accurate morphologic data (e.g. Cashman et al., 2006). Lidar provides a

unique opportunity to test existing numerical models with data from natural lava flows (e.g., Cashman et al., in review).

Here we use local slope, as well as flow and channel width measurements from the Collier Cone lavas, to constrain effusion rate, which, in turn, allows us to estimate the eruption duration. Following Kerr et al. (2006) we calculate the cross-slope flow distance (i.e. flow width, *w*) as a balance between the internal lava flow rheology moving down slope and the cooling crust restraining the lava:

$$w = \left[\frac{(g\rho)^2 Q^7 \mu^4 cos^9\theta}{\sigma_c^6 \kappa^3 sin^7\theta}\right]^{1/13} \qquad (1)$$

where g is acceleration due to gravity, ρ is the lava density, Q is the effusion rate (m^3/s), θ is the slope in radians, μ is the lava viscosity, σ_c is the crustal yield strength, and κ is the thermal diffusivity. Slopes measured within the channel of the western Collier lava lobe reflect the current channel surface rather than the pre-existing flow topography; we consider these slopes to be average values because it is likely that lava filled underlying depressions. We assume fixed values of ρ = 2600kg/m^3, σ_c = 2MPa, $\kappa = 10^{-6}$ m^2/s, and $\mu = 10^6$ Pa s; these physical parameters were inferred from observations of an andesite lava flow from Lonquimay Volcano, Chile (Naranjo et al., 1992), which is similar in size and composition to the Collier Cone lava (Table 4). We also assume a constant average effusion rate. Of these assumptions, those of constant viscosity and effusion rate introduce the largest errors, as both parameters are likely to have changed during the eruption (e.g., Naranjo et al., 1992).

Table 4- Comparison of Collier Cone, OR and Lonquimay, Chile volcanoes

	Collier Cone, OR	Lonquimay, Chile
Composition	55.4-65.1wt% SiO_2	58-59wt% SiO_2
Lava volume	0.17km^3	0.23km^3
Final length	13.6km	10.2km
Crystallinity	≤5-30% (unit variable)	uniform crystal-poor (<1%)
Average slope	3.10°	3.00°
Thickness range	3-32m	5-50m
Eruption rate	10-50m^3/s	10-80m^3/s
Emplacement time	39-197days	330days

The model predictions closely parallel measured flow and channel widths except in short stretches of unusually low slope (≤0.3°), where predicted widths increase sharply (Fig. 4.8). We attribute this mismatch to two factors. First, our slope measurements are based on average surface slopes within limited channel segments; it is certainly possible that local anomalies in channel infilling and drainage create channel surface slopes that are not representative of underlying slopes. Second, we expect that changes in flow width in response to slope variations requires a finite response time, so that the length scale of the slope change may limit the extent to which the flow can respond before encountering steeper slopes. Additionally, we measure unusually low slopes where outbreak floods from a glacial lake near Collier Cone have traveled down the White Branch Creek and deposited alluvium within the lava channel (Fig. 4.6). At these locations the model predicts unreasonably large flow widths that are not relevant as the lava slope has been

modified. For these reasons, we remove all points with slopes ≤0.3° prior to interpreting flow emplacement characteristics obtained from the Kerr et al. (2006) model.

We find that a constant effusion rate of $3m^3/s$ best predicts the innermost channel widths of the western Collier lobe (Fig. 4.8) Increasing the effusion rate moves the predicted widths closer to the measured widths of the western flow lobe (squares- Fig. 4.8), although the flow widths cannot be predicted as accurately as the channel widths. In a similar analysis, Cashman et al. (in review) successfully predicted channel widths for a basaltic lava flow on Mt. Etna, but were unsuccessful in predicting flow widths because of the variability caused by bifurcations, breakouts, and lobate flow margins. The western Collier flow, with limited channel overflows and a single major flow bifurcation near Sims Butte, is generally better behaved and can be fairly well matched using an effusion rate of $\leq 20m^3/s$ (Fig. 4.7a). As flow widths were set by Unit 1 activity and channel widths derive primarily from Unit 2, we suggest that effusion rates of $20m^3/s$ and $3m^3/s$ provide average eruption rates for these units. More broadly, channel widths are bracketed by effusion rates of $1\text{-}10m^3/s$ while the flow widths are bound by $\sim 10\text{-}50m^3/s$ (Fig. 4.9).

Using a calculated volume for the western lobe of $\sim 0.14km^3$ and an inferred range in effusion rates of $1\text{-}50m^3/s$, we can estimate the western Collier lobe was emplaced between 32 and 1620 days. If we add $0.03km^3$ for the northwestern flow lobe, we can bracket the entire eruption to <1968 days. This emplacement duration is much longer than the 330 day duration of the 1989-1990 eruption of Lonquimay, Chile, which had a volume of $0.23km^3$. For the Collier lava flows, we consider effusion rates determined by

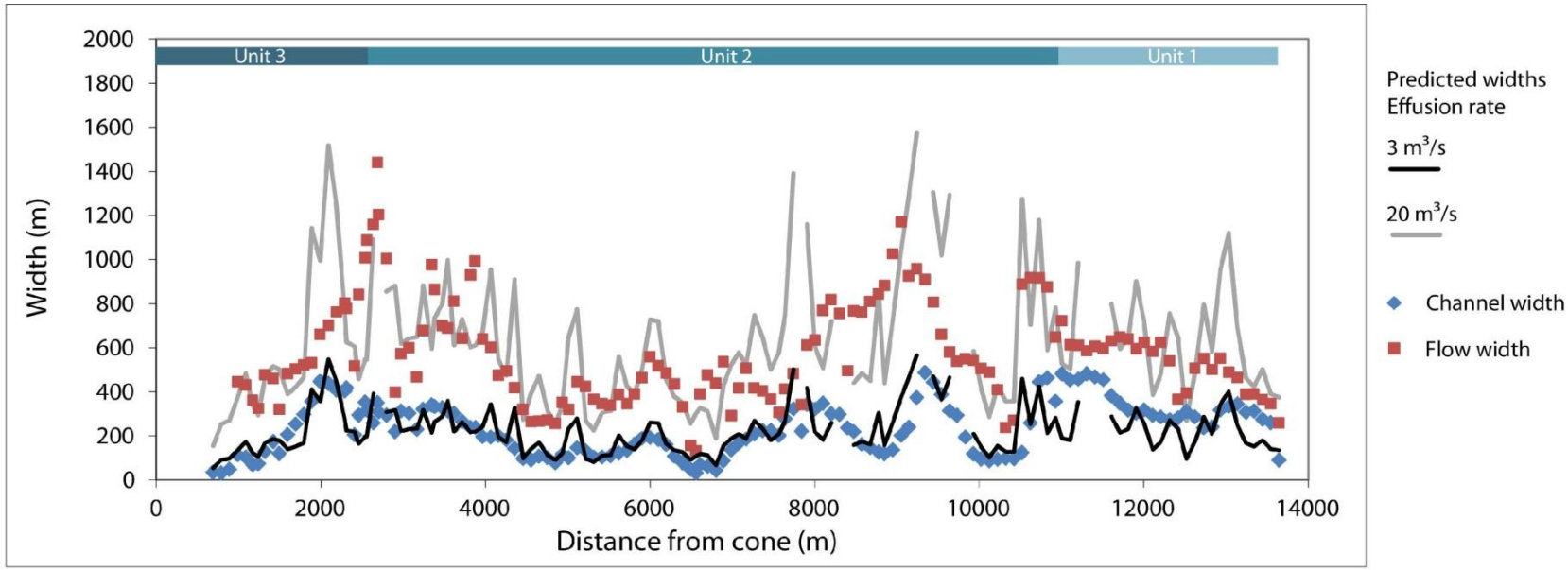

Fig. 4.8.- Comparison of measured channel (diamonds) and flow widths (squares) with predicted widths from the Kerr et al. (2006) model. Predicted widths of constant effusion rates are plotted as solid lines. Predicted widths from extremely low slopes(<0.3°) have been removed. Channel widths are fit closely with an effusion rate of ~3m^3/s, while flow widths are fit best by ~20m^3/s. The extent of each relevant lava unit is identified by the bar on top of the figure ranging from dark (Unit 3) to medium (Unit 2) to light (Unit 1) blue.

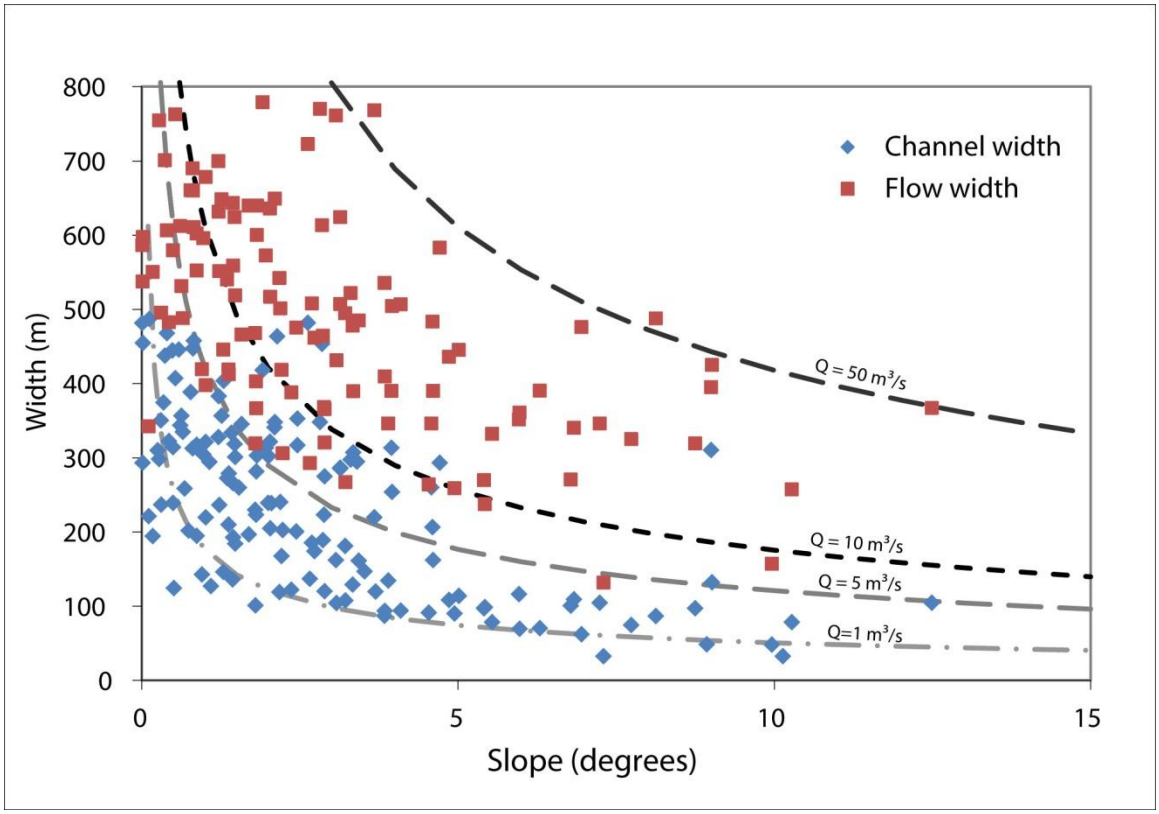

Fig. 4.9.- Measured flow and channel widths are shown to decrease with increased slope. Dashed lines represent modeled constant effusion rates. Channel widths (diamonds) are bracketed by effusion rates of 1-10m^3/s, while flow widths (squares) are bracketed by 10-50m^3/s.

channel widths to be minima. Flow widths predict more realistic effusion rates (10-50m^3/s) and emplacement durations (32-197days) that are comparable to Lonquimay. Importantly, most (8.7 of 10.2km) of the Lonquimay lava flow was emplaced within 100 days; as we infer a peak effusion rate for Unit 1 lava, we suggest that the initial advance of the Collier Cone lava flow was also rapid, possibly reaching its maximum flow length in a month.

5.2. *Surface Morphology*

The most obvious geomorphic features on the Collier lava flow besides the leveed channels are the pronounced surface folds that form both in distal flow lobes and in many places within the lava channels. Surface folds record the dynamics of flow emplacement and are formed by the competition between the fluid processes driving the flow (controlled primarily by lava flux and rheology) and the restraining presence of a growing (and confining) crust (e.g., Griffiths, 2000; Applegarth et al., 2010a). Surface folds have been interpreted as compression of the advancing flow against a solidifying crust (Fink and Fletcher, 1978; Fink, 1980). However, folds often initiate near eruptive vents and are well developed in most lava channels (e.g., Pyle and Elliott, 2006), which suggests that at least some folds may form because of lateral extension within the channel (e.g., Smith and Houston, 1994). Alternatively, the surface folds may form when fluid traction along the base of the higher viscosity lava surface creates enough instability to induce buckling (Slim et al., 2008). Here the interior must travel at higher velocity than the higher viscosity surface to induce shear, but a flow constriction is not required for buckling to occur.

5.2.1. Spectrograms:

Surface folds are present on all lobes of the Collier lava flow field. If changes in flow morphology, such as a constriction or gradient change, are responsible for surface buckling, the appearance of surface ridges should correlate with these regions. To look for this correlation we created spectrograms along a centerline profile of the western lobe

of the Collier lava flow. In the spectrograms, the surface topography is represented by the intensity of the spectral signal as a function of signal frequency (Fig. 4.10). The underlying assumption is that surface folding is periodic. In Figure 4.10, the very high power region represented by the dark red band (frequencies $<0.025m^{-1}$; $\lambda>40m$) in all profile spectrograms is probably an artifact of the sliding window used in the analysis. The parts of the flow with the smoothest topography (no surface folding) show low power signals at all frequencies $>0.025m^{-1}$ ($\lambda<40m$). Areas with large and periodic surface folds are indicated by 'flames' of warm colors (strong signals) that disrupt the very low frequency red band and extend into frequency ranges of 0.025 - $<0.1m^{-1}$ (10-40 m wavelength; grey bars in Fig. 4.10). Areas with smaller or less periodic ridges do not disrupt the red band but still have increased power signals at higher frequencies (light grey bars).

Examination of the full profile spectrogram reveals topographic signatures of features other than ridges (Fig. 4.10). The first ~700m of the spectrogram has unusually low spectral power where glacial outwash partially covers the lava. Where the flow bifurcates, the profile traverses levees and lava lobes, so that the spectrogram is not representative of the channel surface. Near the flow terminus, the lava transitions from channel to flow margin. This transitional zone has unevenly spaced ridges that produce a spectral signature that is similar to that generated by pronounced surface ridges oriented perpendicular to flow direction.

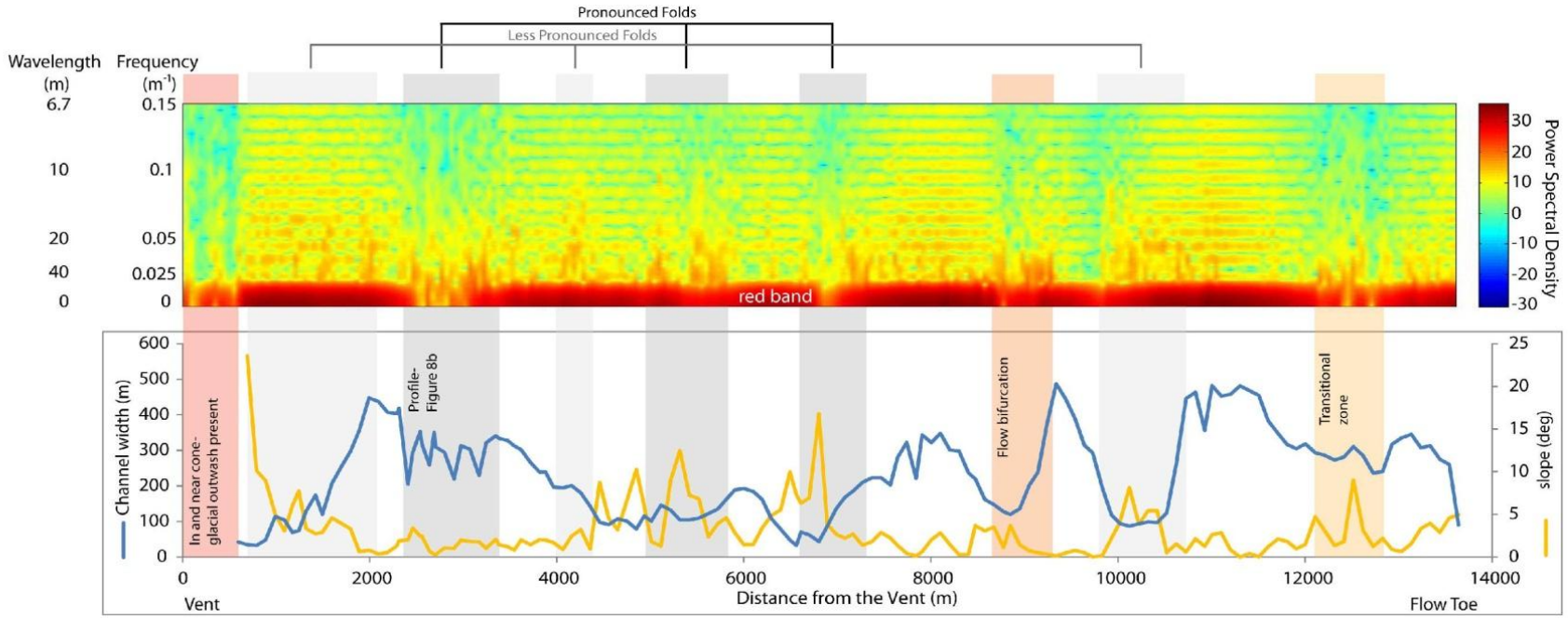

Fig. 4.10.- Spectrogram (top) of the western lava lobe full channel profile. Topographic features are identified by fluctuations in the power spectra as a function of frequency. Power spectral density (values are arbitrary) represents the amplitude of a particular frequency. Warm colors represent strong signals with greater periodicity from more pronounced topography. Pronounced surface folds (grey bars) and less pronounced folds (light grey bars) extend strong signals to higher frequencies. Other topographic signals produce spectral signals, including glacial outwash within the cone (red bar) and a transition zone of uneven ridges near the flow toe (orange bar). At the flow bifurcation the channel profile does not split and includes levees and flow lobes; data should be ignored. Pronounced folds occur in areas of rapidly fluctuating or increasing channel widths (bottom).

To explore the spectral signature of surface ridges in more detail, we examine two short (1000m) profiles that have contrasting surface textures (Fig. 4.11; segments w2, Unit 2, and nw2, Unit 3, in Fig. 4.3). In these spectrograms, most of the spectral density lies at frequencies of $<0.15m^{-1}$ ($\lambda>6.7m$). The channel section shown in Figure 4.11a shows pronounced surface folds with a range of amplitudes (Fig. 4.11b). The topographic signatures of the folds are represented by a high power region between $0\text{-}0.1m^{-1}$ ($\lambda>10m$) and dissipating to $\sim0.2m^{-1}$ (Fig. 4.11c). Channel segments that do not have continuous surface folding (e.g., Fig. 4.11d) have correspondingly weak spectral signals. As an extreme example, we highlight a >200m channel segment without visible surface features (grey bar in Figs. 4.11e,f). This region, in particular, has a weak topographic signature with a narrow high power region ($<0.025m^{-1}$; $\lambda>40m$). Additionally, this entire channel section is smoother (lower spectral density) at high frequencies ($>0.25\ m^{-1}$; $\lambda<4m$) than the channel section shown in Figures 4.11a-c. These differences in small scale roughness may represent differences in the mean block size of the flow surface; testing this hypothesis would require detailed field measurements that are beyond the scope of this study.

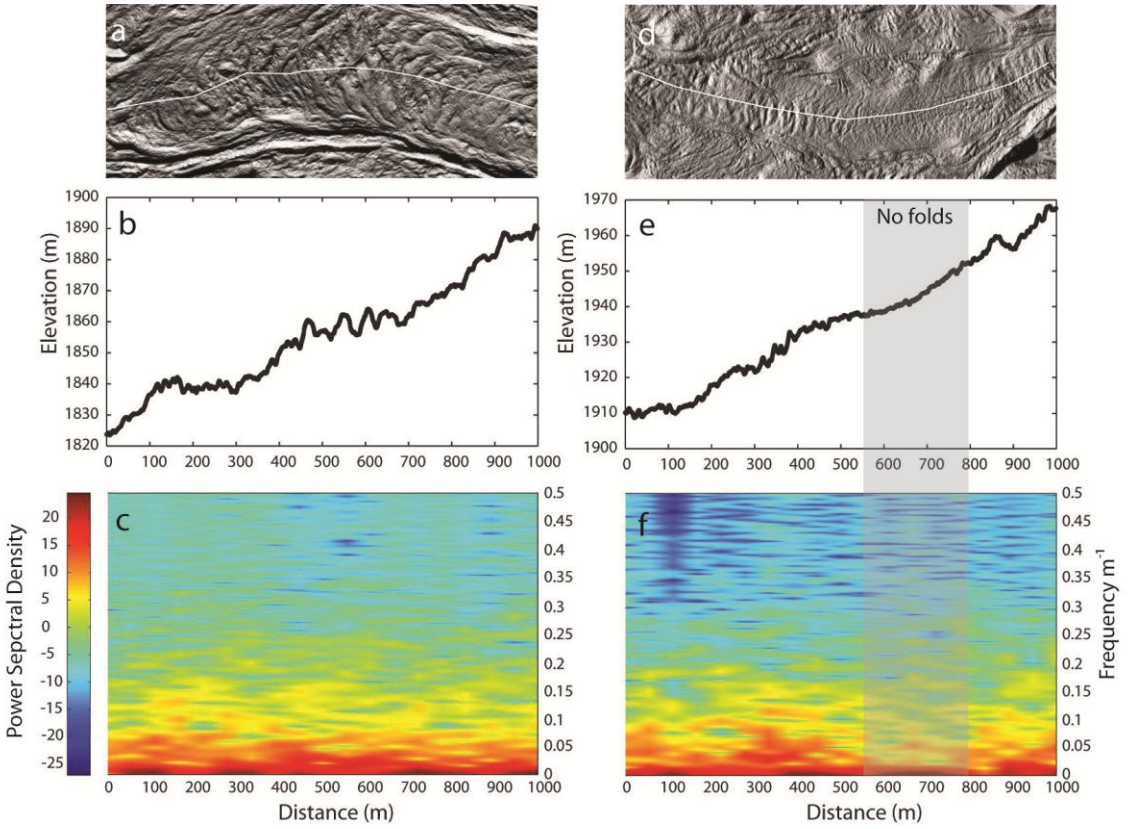

Fig. 4.11.- Representative 1000m profiles of w2 and nw2 (Fig. 4.3). Channel centerlines are identified as white lines (a,d). Profiles are plotted as elevation with distance (b,e). Profile (b) has pronounced surface folds for its entire length. Profile (e) has a region without folds >200m long (grey bar), that is surrounded by small folds. Areas with folding are represented in the spectrograms by stronger spectral density signals over a wider range of frequencies (c,f), while areas without folding (f-grey region) show a very narrow range of frequencies with strong spectral signals, and generally have reduced spectral densities.

Surface fold locations within the Collier lava show no obvious correlation with flow width, flow thickness, or slope. However, the most pronounced surface folds occur in areas of increasing channel width, particularly after width was decreased (Fig. 4.10). In areas of channel widening the lava velocity must decrease to conserve mass balance. Rapid deceleration, particularly after a fast narrow channel, may induce shear or drag on

the base of the crust producing buckling. Additionally, the decelerating flow front should experience compression, which may enhance buckling. These surface instabilities may continue as the channel progressively widens. However, on the Collier flows if the channel continues to widen the surface folds dissipate and lose some of their expression.

5.2.2. Surface analysis:

Several authors have attempted to relate surface folding to lava rheology (e.g. Fink and Fletcher, 1978; Fink, 1980; Gregg et al., 1998; Castro and Cashman, 1999). In theory, the geometry of flow surface folds can be used to constrain the thickness and viscosity of the folding layer (from the fold wavelength) and the compressional stress (from the fold amplitude; e.g., Fink and Fletcher, 1978; Gregg et al., 1998). Crustal thickness is controlled primarily by lava composition and extent of cooling - lavas of more evolved compositions advance more slowly and have thicker crusts, which generate surface folds with larger wavelengths.

Fink and Fletcher's (1978) analysis assumes that lava viscosity decreases exponentially from the surface to a constant interior value. Minimum lava viscosity can be estimated if wavelength and crustal thickness are known. Crustal thickness is typically estimated from measured fold amplitudes or depths of surface cracks; fold amplitudes measured in this way may be minima if compression has pinched off the anticlinal trough

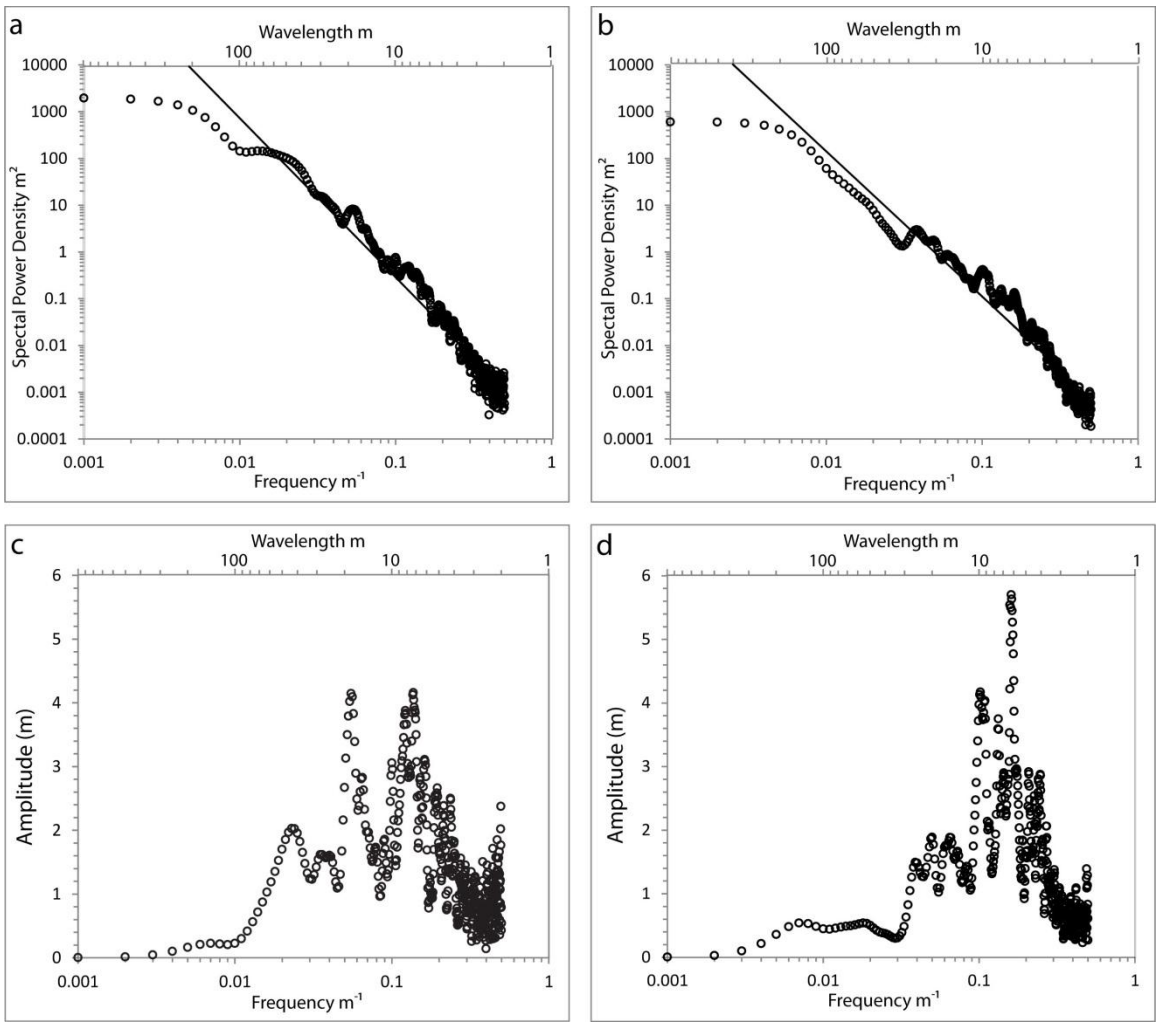

Fig. 4.12.- Discrete Fourier Transform periodograms of 1000m profiles w2 and nw3 (Fig. 4.3). Significant topographic signals (i.e. surface folds) are represented by vertical deviations from the powerlaw trendline. The frequencies at which these deviations occur provide dominant wavelengths of surface folding. Dominant wavelengths are more easily observed in normalized periodograms (c,d). Profile w2 has pronounced folding with dominant wavelengths at 40-50m, 20m and 5-10m (a,c). Profile nw3 has limited or no folding but still produces a strong signals at <10m wavelength (b,d).

or if the trough has been filled with debris. Lidar DEMs allow accurate measurement of both wavelength and amplitude through the application of Fourier transform analysis to along-flow transects. Here we use Discrete Fourier Transform analysis to quantify fold

characteristics from 1000m representative Collier channel segments. Two examples are shown in Figure 4.12 (w2, shown in Fig. 4.11a-c, and nw3, see Fig. 4.3 for location).

DFT analysis of 1000m profiles provides a measure of wavelengths and amplitudes over a range of frequencies. The spectral densities of the analyzed lava profiles decrease with increased frequency, as expected for landforms (Perron et al., 2008). A relatively flat lava profile with no topographic features (other than block sizes) would follow this trend without deviations. Prominent morphological features (such as surface folds, tumuli, extensional cracks, etc.) produce deviations from the trend in the form of vertical fluctuations at intermediate frequencies (Fig. 4.12a,b) that can be analyzed to extract the dominate wavelengths and amplitudes of folding.

We confine our analysis to intermediate frequencies of 0.2-0.02m^{-1} (fold wavelengths of 5-50m); long wavelengths approach the limit of recognizable wavelengths (half the window length of 200m), while smaller wavelengths may be complicated by variable surface block sizes or gridding artifacts. The spectra shown in Figures 4.12a and 4.12b show contrasting behavior at intermediate frequencies that reflect real variations in surface folding characteristics. Vertical fluctuations are enhanced by normalization to the power law of the spectral signal (Fig. 4.12c,d). Figure 4.12c shows distinct broad peaks at wavelengths of 40-50m, 20m and 5-10m that reflect the frequency range (0.025-0.2m^{-1}) of elevated spectral density identified in Figure 4.11c. Figure 4.12d is a region without obvious surface folding; however, the spectrum deviates from the expected trend at small wavelengths (<10m), and shows sharp peaks at wavelengths of 6 and 10m. More generally, analyzed channel segments along the

northwest lobe show strong peaks at 0.03-0.04, 0.08-0.09, and 0.1-0.2m^{-1} (λ= 25-33, 12-14, and 5-10m; Fig. 4.12d). In contrast, the western channel segments show consistent strong peaks at frequencies of 0.025, 0.06-0.07, and 0.1-0.15m^{-1}(λ= 40m, 14-17m, and 7-10m, respectively; Fig. 4.12c). The small wavelength (5-10m) signals present in all spectra may represent first generation folding that is not easily discernible from the DEM because of overprinting by surface block textures. We suggest that folds with larger wavelengths represent subsequent fold generations. Multiple fold generations are common in Hawaiian pahoehoe flows and record thickening of the surface crust during flow.

The normalized spectra show surface fold amplitudes relative to the power law and should, therefore, be considered minima. Additionally, the DFT analysis may have averaged peaks and troughs of surface folds as natural features are neither perfectly sinusoidal nor periodic. For these reasons, we also measured amplitudes directly from profiles of the 1000m segments to determine the full range of <1 to 7.2m; with the highest amplitudes (>4m) measured on folds with the largest wavelengths (>30m). The average amplitude for all analyzed segments is 2.3m (±1.3).

In a folding analysis of layered obsidian and pumice in rhyolitic lava, Castro and Cashman (1999) relate dominant wavelength (W_d) to layer thickness (T) and the shear viscosity ratio (μ_l/μ_m) between layers through:

$$W_d = 2\pi T \left(\frac{\mu_l}{6\mu_m}\right)^{1/3}$$

assuming a Newtonian fluid (after Biot, 1961). In this relationship, dominant wavelength increases as a function of thickness and shear viscosity ratio. Similarly, the wavelengths of surface folds should scale with crustal thickness and flow viscosity, which depend on effusion rate and lava composition. Therefore, increases in surface fold wavelengths should correlate with more evolved (higher viscosity) lava compositions. To test this, we have compiled surface fold measurements and compositional data from the literature for lava flows that range in composition from basalt to rhyolite (Fig. 4.13). Surface fold measurements from the literature were obtained by a number of different methods, including field measurements, aerial photos, and satellite, airborne, and terrestrial remote sensing (Table 5). We have added to the existing database using GoogleEarth to measure fold wavelengths on flows for which composition is known.

As expected, figure 13 shows that fold wavelengths generally increase with increased SiO_2, as lava evolves from basalt to dacite. However, the dacitic lava flows show a striking departure from the trend defined by the other flow compositions. In particular, rhyolite flows have surface fold wavelengths that are surprisingly similar to those of andesite lavas. This similarity may be explained by considering the effective viscosity of the lava. Although rhyolitic melts have viscosities that are higher than melts of less evolved compositions, effective viscosity is strongly influenced by the crystal content of the lava. Obsidian flows, by definition, have low crystallinities. In contrast, H_2O-rich andesite and dacite lavas often have high crystallinities because of extensive decompression-driven crystallization. The effects of crystallization are two-fold: addition of solid particles increases the effective viscosity (e.g., Costa, 2005) and crystallization

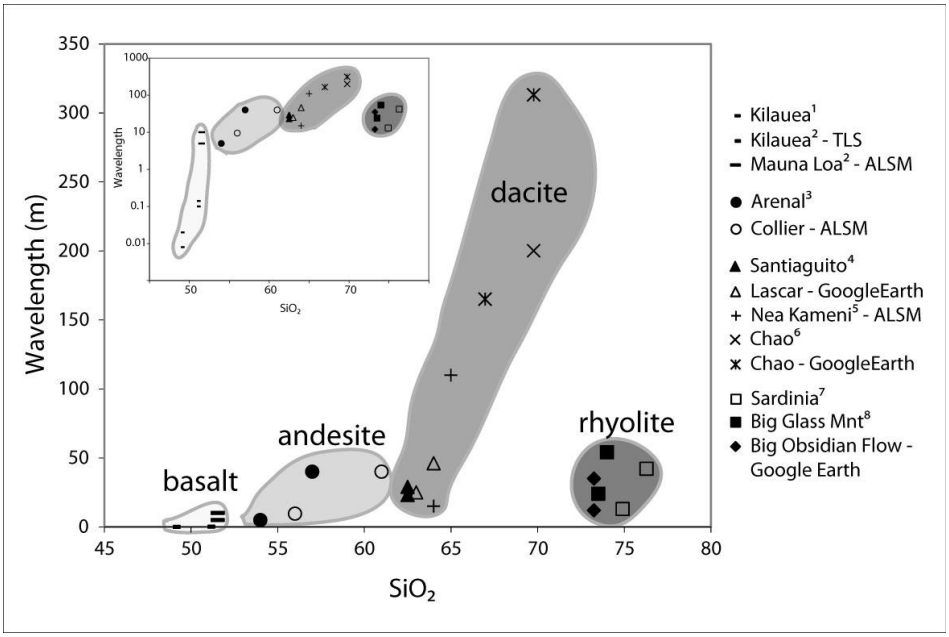

Fig. 4.13.- Measurements of surface fold wavelengths for lava compositions from basalt to rhyolite. Surface fold wavelength generally increases from basalt to rhyolite (inset-log plot). However, dacite fold wavelengths can be significantly larger than andesite and rhyolite folds; possibly due to increased effective viscosity from higher crystallinity. Therefore, wavelengths appear to increase with increased effective viscosity rather than composition. Measurements were collected from the literature, lidar measurements of Collier Cone lava, and GoogleEarth measurements (see Table 5). Literature references are numbered and listed in Table 5.

increases the silica content (and viscosity) of the remaining matrix melt. Thus andesitic lavas may have matrix glass compositions that approach low-Si rhyolite, while dacite lavas often have high-Si rhyolite matrix melt compositions (e.g., Cashman and Blundy, 2000). Therefore, we hypothesize that the large fold wavelengths shown, in particular, by the Chao dacite lava flow in the central Andes Altiplano-Puna Volcanic complex may reflect effective viscosities. This hypothesis is consistent with reports of lava crystallinities of 40-60%, flow front thicknesses of <400m, and apparent viscosities of 10^9 Pa s (de Silva et al., 1994- using method of Pinkerton and Stevenson, 1992).

Table 5- Methods for measuring wavelength and amplitude on lava surfaces

Location	Method	Lava type	reference
Kilauea, Hawaii	manual measurements- traced topographic profiles	Basalt-pahoehoe	[1]Fink and Fletcher, 1978
Kilauea, Hawaii	terrestrial lidar scanning (TLS)	Basalt-pahoehoe	[2]Cashman et al., submitted
Mauna Loa, Hawaii	1m airborne lidar DEM	Basalt- a'a	[2]Cashman et al., submitted
Arenal, Costa Rica	manual- field measurements	Andesite-blocky	[3]Linneman and Borgia, 1993
Collier Cone, OR	DFT analysis from 1m Lidar DEM	basaltic andesite-dacite	this study
Santiaguito, Guatemala	manual- field (and aerial photos?) measurements	dacite-blocky	[4]Harris et al., 2004
Lascar, Chile	GoogleEarth	dacite-blocky	this study
Nea Kameni Santorini, Greece	1m airborne lidar DEM	dacite	[5]Pyle and Elliot, 2006
Chao, Chile	aerial and satellite photos	dacite-blocky	[6]de Silva et al., 1994
Chao, Chile	GoogleEarth	dacite-blocky	this study
Sardinia, Italy	manual- field (and aerial photos?) measurements	rhyolite	[7]Cioni and Funedda, 2005
Big Glass Mountain, CA	field measurements and aerial photos	rhyolite-obsidian	[8]Fink, 1980
Big Obsidian Flow-Newberry, OR	GoogleEarth	rhyolite-obsidian	this study

In addition to increased surface fold wavelengths in more evolved lavas, we also expect wavelengths to increase with distance from the vent. In an along flow Fourier transform analysis of dacite lava, Pyle and Elliott (2006) found dominant wavelengths of ~20m close to the vent increased to 30-40m distally. This can be explained by cooling and thickening of the crust during emplacement; thicker crusts require longer wavelengths to accommodate strain (Fink and Fletcher, 1978). Considering this, the surface folds of the Collier Cone lavas are perplexing for two reasons. First, the fold wavelengths are relatively uniform between units of variable compositions. This is likely explained by similar effective viscosities (i.e. crystallinity and interstitial matrix glass compositions) producing lavas of equivalent flow morphologies. Second, the fold wavelengths do not increase with distance from the vent, suggesting there is limited crustal thickening during emplacement. This may be explained by blocky silicic lavas emerging with a solidified crust, reducing the amount of cooling and crystallization that is possible on the lava surface. The limited crustal thickening may also suggest the Collier lava flows were emplaced relatively quickly, further limiting cooling prior to emplacement. Therefore, surface folds provide further evidence for lava emplacement at high effusion rates ($<50 m^3/s$) and emplacement durations of weeks to months rather than years.

6.0. Conclusions

In this study, we presented a field and GIS-based analysis of the c. 1600 ybp Collier Cone, OR blocky lava flow field. The flow field is composed of three morphologically and geochemically distinct lava units, ranging from basaltic andesite to

dacite. We used Lidar-derived DEMs (gridded at 1m resolution) in a GIS-based analysis to extract morphologic measurements and analyze surface features. Morphologic measurements were used to calculate the flow volume and determine morphologic relationships, such as channel and flow widths are coupled and correlate positively with flow thickness and inversely with slope. Measurements of channel width, flow width and slope were also used with an existing numerical model (Kerr et al., 2006), and reasonable assumptions of lava rheology, to determine the range of effusion rates (~10-50m^3/s) and emplacement times (32-197days) for this prehistoric lava flow field. Very few blocky lava flows have been observed by geologists during emplacement. Therefore, from a hazards perspective it is important to understand that the eruption of a lava flow of similar dimensions (~13km long) and composition to the Collier flow field will require weeks to months for emplacement.

Surface folds from the Collier lava channels were analyzed with Discrete Fourier Transform spectrograms and periodograms. Spectrograms were used to visualize the spatial occurrence of surface folds along the channel of the western lava lobe and to determine the relationships between surface folds and lava morphology. Prominent folding appears to correlate with increasing channel width and decreasing velocity, inducing shear or drag on the base of the crust and inducing buckling. DFT periodograms remotely provided dominant wavelengths and amplitude estimates of surface folds. The periodograms displayed dominant wavelengths were similar in all parts of the flow field with multiple generations of folds. All sections analyzed had dominant wavelengths at 12-17m and 5-10m, while the largest dominant wavelength was bigger on average in the

western lobe (~40m) than the northwestern lobe (25-33m). Compilation of surface fold wavelength data from lava flows of various compositions around the world indicates wavelengths increase with SiO_2 concentrations from basalt to dacite. However, dacite has a significantly larger range in fold wavelength than rhyolite. We believe this is caused by high effective viscosities in dacite of high crystallinity, relative to crystal-poor rhyolite. Therefore, surface fold wavelengths may be dependent on crystallinity and effective viscosity.

CHAPTER V

CONCLUSIONS

This dissertation has focused on subaerial and submarine mafic eruptions in volcanic arcs. In particular, I have addressed the effect of volcanic eruption rates on the eruption style and deposition for both effusive and explosive eruptions. This study has included video observations and sampling from an actively erupting volcano and analysis of a c. 1600 ybp lava flow using both terrestrial field work and high resolution digital topography. In each case, the resulting depositional morphology was strongly influenced by the eruption rate and the environment of emplacement.

In Chapter II, I began with the analysis of explosive eruption plumes and tephra collected from the actively erupting submarine volcano, NW Rota-1, Mariana arc. The eruptions along the southern flank of NW Rota-1 are small, with relatively low mass eruption rates (MER) and are strongly effected by ambient seawater. Eruption into seawater produces increased drag, cooling, and hydrostatic pressure; all of which suppress the eruptive plume and limit clast deposition. NW Rota-1 is situated at a depth (summit at ~517m bsl) in which temporary steam expansion is possible, although limited. However, steam does not appear to strongly effect eruptions, which are primarily magmatically-driven. These observations are significant for two reasons: (1) they are the first direct observations of magmatically-driven submarine explosive eruptions and (2) they provide evidence that explosive eruptions at moderate depths below sea level

(>100m) do not require water-lava interactions, which in turn, suggests explosive activity can be expected at depths greater than 550m bsl.

The eruptions at NW Rota-1 are small, with relatively low MER but display a wide range of activity from slow lava effusion to strong intermittent explosive bursting to nearly continuous cyclic activity producing sustained plumes (Chapters II and III). Additionally, higher MER explosive activity has been inferred from microcrystalline textures and hydrophone acoustic data. The eruption styles (both observed and inferred) appear to be the result of eruption rate and/or magma ascent times. In Chapter III, I identify each eruptive phase through their characteristic microcrystallinities, which decrease with increased MER. Plume suppression and low MERs at NW Rota-1 provide an ideal environment for pyroclast recycling, as the low-level explosive bursts have insufficient strength to fully expel pyroclasts from the vent. I have found evidence for recycling of pyroclasts in the form of video observations of pyroclasts falling back into the vent and in collected tephra with NaCl-enriched microcrystalline inclusions in microlite-poor matrix (Chapters II and III). The Cl enrichment and additional crystallization provide evidence for seawater (or NaCl-rich brine or salts) entrainment and reheating of pyroclasts. This could only be accomplished by entraining cooled clasts, with the addition of a NaCl source, within juvenile melt in the vent. I have performed crystallization experiments by reheating pyroclasts and modeled Cl diffusion to constrain the timescales (minutes to 10s of minutes) required for pyroclast recycling (Chapter III). Microcrystalline textures, similar to those found at NW Rota-1, are observed in mafic tephra from subaerial volcanoes around the world. The commonality of microcrystalline

inclusions suggests recycling is not limited to the submarine environment, but is the result of low MER mafic eruptions. Recycling is likely more common in the submarine environment due to seawater suppression and is more easily identified through Cl enrichment.

In Chapter IV, I changed gears and moved to the subaerial environment where I mapped and analyzed the lava flow field of Collier Cone, OR. Contrary to our analysis of the NW Rota-1 eruptions, which was an observed actively erupting volcano, the objective for the Collier lava was to estimate the emplacement conditions for the previously emplaced lava flow. Analysis of the lava flow field included the extraction of morphologic measurements using GIS and Lidar-derived high resolution (1m) maps. The GIS-based analysis extracted simple measurements of channel and flow widths, slope, and flow thicknesses and could be used remotely on digital topographic data for any volcano, including planetary lava flows. I then used the extracted channel widths, flow widths and slopes with an existing numerical model by Kerr et al. (2006) to determine the range in effusion rates bracketing the measured widths. From this analysis I have determined a range in effusion rates of 10-50m^3/s, which in turn, provides emplacement times of 32-197days for the Collier lava flow field. Importantly, this analysis provides an estimated eruption duration of weeks to months for future lava flows of similar composition and volume for the sparsely populated, yet volcanically active, Oregon Central Cascades.

In Chapter IV, I also analyzed lava surface morphologies, specifically, the periodicity of surface folds, which are very common on lava flows on Earth, as well as

other planets and moons. Surface folds are common in lava of all compositions and emplacement conditions. Using profiles extracted from the Lidar data, I used discrete Fourier transform analysis to determine the dominant wavelengths and spatial distribution of periodic or pseudo-periodic lava surface features. From this analysis I determined the surface folds include three folding generations between 5-40m wavelengths. The dominant wavelengths are relatively consistent throughout the lava flow field, although Unit 3 (the northwest lobe) has slightly smaller long wavelength folds (<33m). I then compared the dominant wavelengths of the Collier lava to those of other lava flows, ranging from basalt to rhyolite in composition. From this, I found fold wavelengths generally increase with more evolved compositions, but more specifically with increased effective viscosity. Dacite, in particular can have exceptionally large fold wavelengths (>100m), likely due to large crystallinities and high effective viscosities. The surface fold analysis presented in this dissertation could be used remotely on digital topography for any lava flow, including extraterrestrial lava flows.

In summary, within this dissertation I have presented evidence and discussed the effects of effusion rate on eruption dynamics and deposits for mafic eruptions in arc environments. Volcanic arcs produce a large range of activity and eruption styles in both the subaerial and submarine environments. Through the analysis of active eruptions we can directly relate observed effusion rates with eruption style and resulting deposits, while detailed analyses of post-emplacement morphologies (along with numerical modeling) can be used to determine original emplacement conditions for unobserved eruptions. Additionally, advancements in both underwater exploration through remotely

operated vehicles (ROVs) and airborne laser swath mapping have enhanced the ability of volcanologists to observe, sample and quantify volcanic terrains, whether active or inactive.

APPENDIX A

CHLORINE DIFFUSION IN MICROCRYSTALLINE INCLUSIONS

Maximum timescales for recycling can be determined by estimating the time required to diffuse Cl from the pyroclast surface to its interior. To do this, we must make a few assumptions: (1) the recycled inclusions are spherical and of uniform internal Cl concentration before diffusion, (2) measured Cl concentrations of ~2wt% represent the exterior starting concentrations and are constant, and (3) the rate of diffusion is constant. Assuming these conditions we can model diffusion timescales using Crank's (1975) solution for diffusion into a sphere, which involves two dimensionless parameters: Dt/a^2 and r/a. Here D is the diffusion coefficient, t is time, a is the spherical radius, and r is the distance from the center at a given internal concentration (C). The solution for Crank's (1975) spherical diffusion is shown graphically in figure A1 (from Crank, 1975) in the form of $(C-C_1)/(C_0-C_1)$ as a function of r/a for a variety of Dt/a^2 values. C_1 is the initial concentration of the sphere interior and C_0 is the constant surface concentration. Using the curves from figure A1, as r goes to zero, and the diffusion coefficients for molten basalt at 1100°C and 1150°C (from Alletti et al., 2007) we can model the time required for Cl diffusion into spherical inclusions at NW Rota-1 (Fig. A2). For this model, we use an average host matrix glass concentration of C_0 = 0.2wt% and an exterior concentration C_1=2.0wt%, (representing some of the highest Cl values measured), and solve for the internal concentration (C) at a given time.

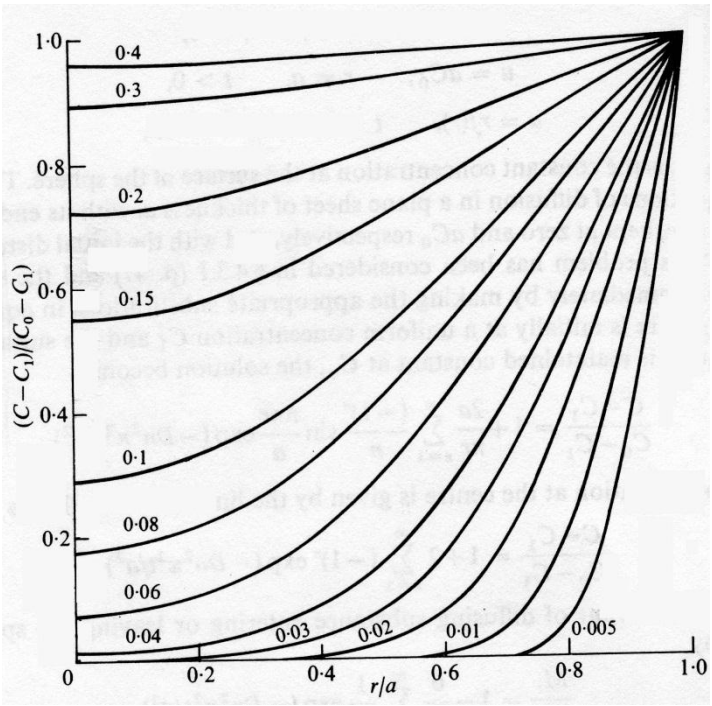

Fig. A1.- Crank (1975) Diffusion- curves showing concentration distributions at various times, from Crank (1975). Numbers on curves are Dt/a^2 values.

Microcrystalline inclusions in NW Rota-1 thin sections range from ≤1-3mm in diameter. However, many inclusions are ≤1mm in diameter and some of the largest inclusions do not have significant Cl enrichment within the interiors. Additionally, all inclusions show rapid increases in Cl concentration from the host matrix glass (~0.2wt%) to enriched concentrations (0.5 - ≤2.2wt%) within ≤50μm (Fig. 3.4). Therefore the smallest radii were chosen for the model.

Figure A2 shows the model is strongly dependent on the inclusion radius and temperature. Time required for diffusion over distances of 50, 100, 250, and 500μm ranges over three orders of magnitude from 10s to 10,000s of seconds. For a Cl enrichment of 0.5wt%, diffusion of 50μm at 1100°C will require ~7.5 minutes (or 500μm

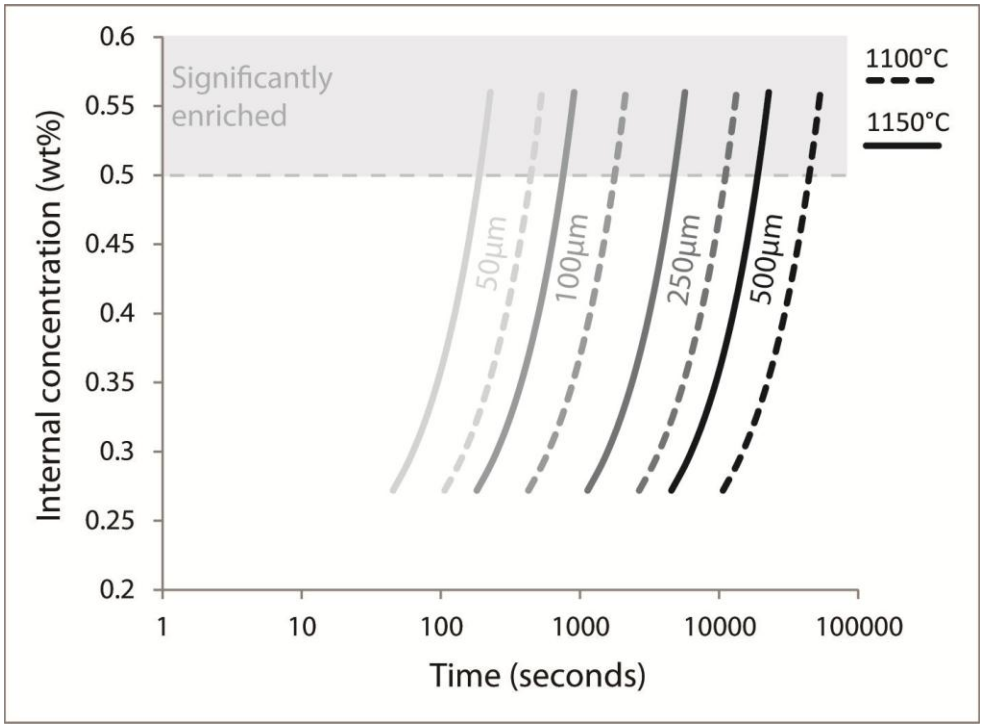

Fig. A2.- Cl diffusion model. Curves determined from Fig. A1 (Crank, 1975) for initial Cl concentrations (C_1) = 0.2wt% and surface concentration (C_0) = 2.0wt%. Lines represent internal concentrations for radii of 50-500µm diameter using diffusion coefficients for anhydrous basalt at 1100°C (dashed) and 1150°C (solid- Alletti et al., 2007). Shaded region represents enriched concentrations (>0.5wt% Cl) commonly observed in microcrystalline inclusions.

in 754 minutes), while at 1150°C the same distances require ~3 and 320min, respectively. If crystallization is occurring simultaneously with Cl diffusion, then the longer limes are not likely. In other words, timescales of minutes to tens of minutes requires very short diffusion distances (50-250 µm) and high temperatures to produce 0.5wt% Cl enrichment (at 1150°C: ~3-80 min) in anhydrous basalt. If there is a little water present in the glass these times will be reduced, as diffusivities increase in hydrous basalt (Alletti et al., 2007). Since microcrystalline inclusions have larger radii than 50-250µm, diffusion is likely being facilitated by vesicles and cracks within the recycled areas.

We have observed some unusual crack-like features in the NW Rota-1 thin sections that also contain recycled pyroclasts. The crack-like features are similar linear to thermal cracks (from rapid quenching of pyroclasts), however, they appear to be filled in or 'healed' rather than being empty cavities. These 'healed' cracks are found outside of microcrystalline inclusions within the surrounding matrix glass and appear as brown to dark brown lineations in plane polarized light; they can be sharp and distinct (Fig. A3) or wider and more diffuse (Fig. A4) where intersected obliquely. In BSE images the cracks are <5μm in diameter, brighter than surrounding matrix glass, and are often microcrystalline (Fig. A5). The matrix glass immediately adjacent to the 'cracks' is slightly darker than the rest of the surrounding matrix, particularly around the more crystalline 'cracks'. The cracks are accompanied by numerous augite and Fe-sulfide microlites that can extend into the surrounding matrix.

Compositionally, the cracks (including the adjacent dark glass) are similar to the surrounding matrix glass but are enriched in Cl (<1.5wt%) and depleted in Na_2O (0.35 to 3.1wt% - average for surrounding matrix: Fig. A6). Cl enrichment is easily observed using element x-ray mapping (Fig. A7). The healed cracks are shown as bright (high Cl counts) lineations while the thermal cracks have Cl concentrations similar to the surrounding matrix glass and are hard to see (Fig. A7b). Some of the vesicles also appear enriched in Cl, because of the epoxy (~2wt% Cl) used during the creation of the thin section. The epoxy does not appear to have effected the Cl concentrations of nearby glass or our microprobe results.

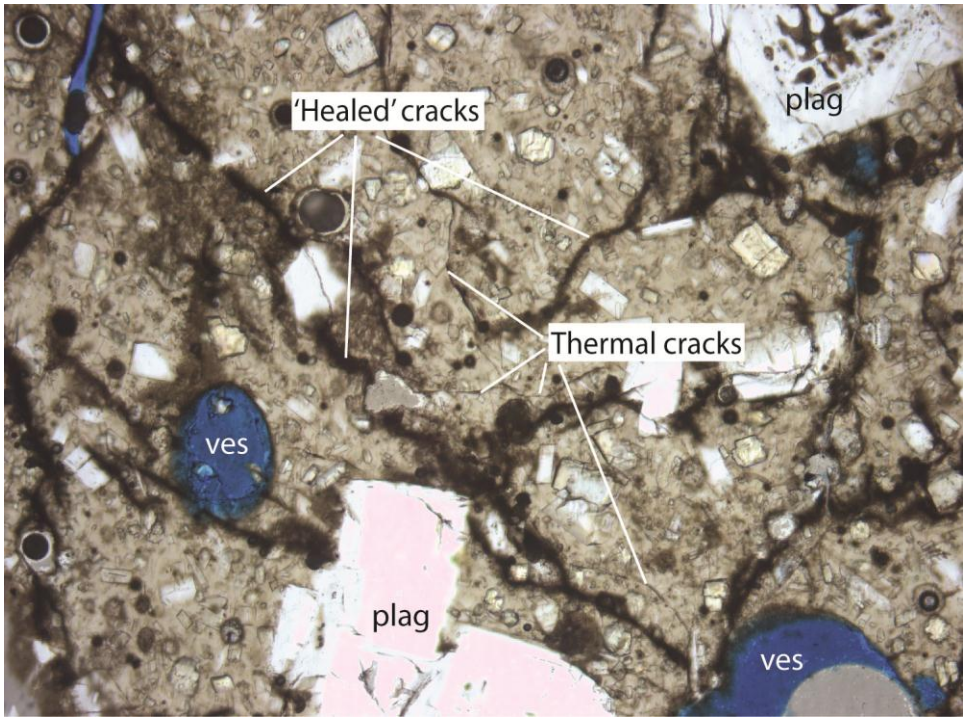

Fig. A3.- Plane polarized light image of 'healed' cracks taken from petrographic microscope. 'Healed' cracks are brown lineations that are finely microcrystalline relative to surrounding matrix glass (tan glass). 'Healed' cracks appear to have similar orientations as thermal cracks from rapid quenching of the glass. Plagioclase phenocrysts are labeled as 'plag'.

Another unusual feature associated with the healed cracks is an odd vesicle texture. In areas where the healed cracks are observed, and sometimes in contact with these cracks (Fig. A7a), this unusual vesicle texture is observed as glass bubbles within pre-existing vesicles. These odd vesicles appear to have grown inside of the pre-existing vesicles, like a balloon blown up inside of another balloon, to produce a 'secondary' vesiculation.

How the healed cracks and secondary vesicles are created is currently unknown. However, we speculate that they are linking to pyroclast recycling at NW-Rota-1. The healed cracks are mostly crystalline suggesting increased temperatures similar (>690°C)

to those involved in pyroclast recycling (Chapter III). Cl enrichment suggests the cracks were once infiltrated with seawater and deposited NaCl, possibly as high temperatures boiled the water to steam. The healed cracks are found within pyroclasts that also contain microcrystalline inclusions. However, the cracks do not appear to radiate outward from the inclusions, as might be expected if seawater, boiling off the included pyroclast, hydrofractured pathways through surrounding quenched glass. The healed cracks appear to reflect thermal cracking and subsequent infilling with microlites and possibly melt.

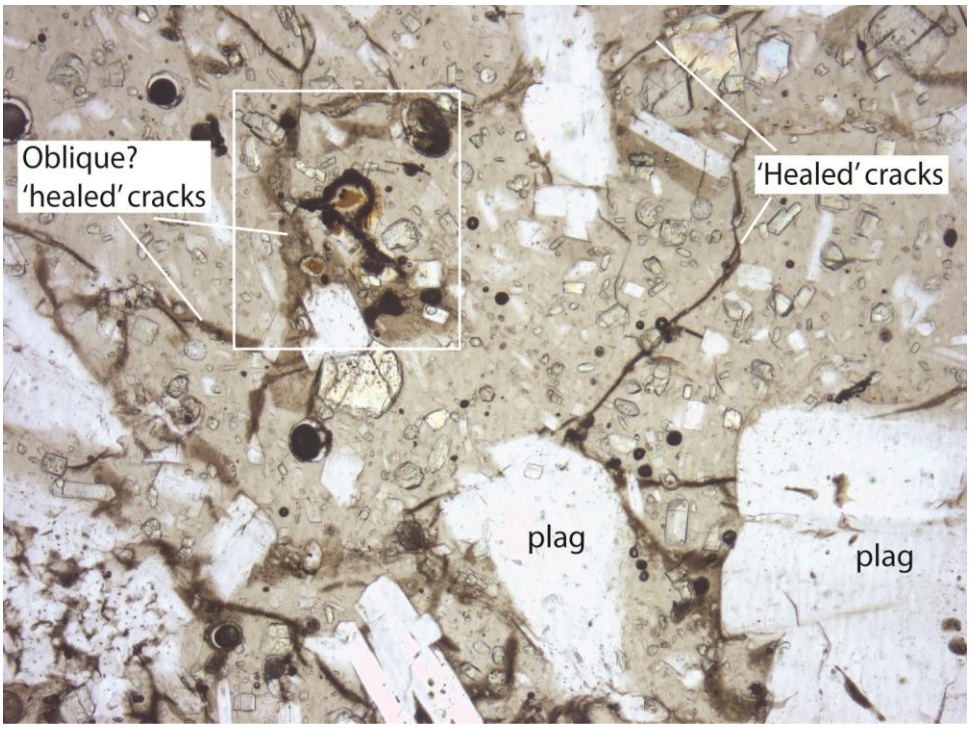

Fig. A4.- Plane polarized light image of 'healed' cracks and secondary vesicles(?). In PPL some of the 'healed' cracks look wider and more diffuse, suggesting they were cut at oblique angles when the thin section was created. Some very unusual vesicles are present in areas with 'healed' cracks (white box). Box is area of Fig. A5.

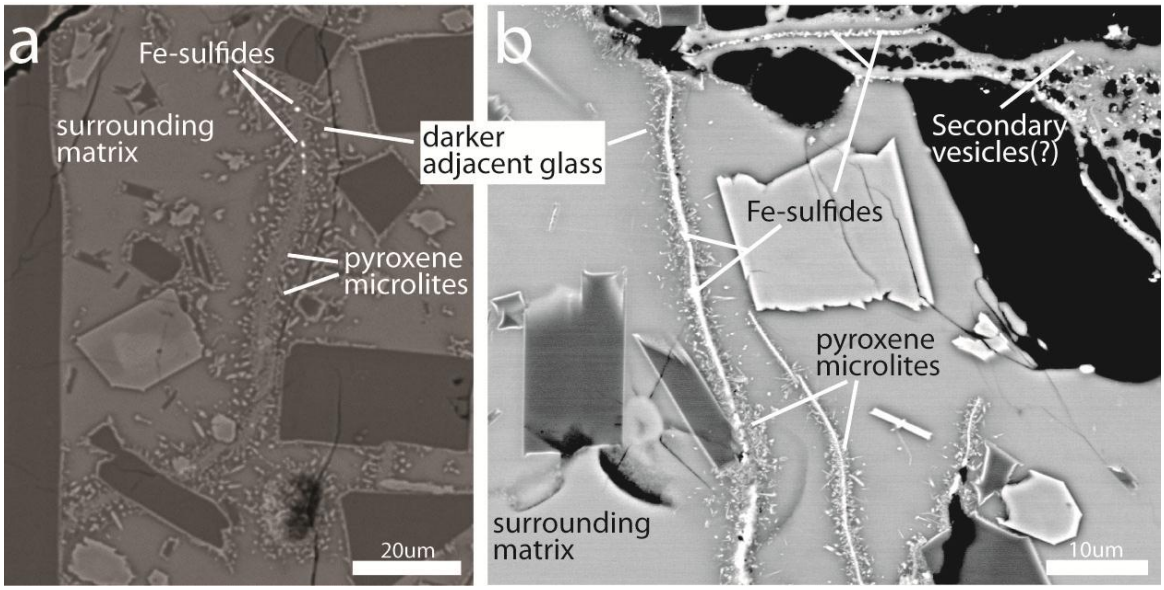

Fig. A5.- BSE images of 'healed' cracks. Cracks are microcrystalline along their edges with some microlites extending into surrounding matrix. Microlites are mostly pyroxenes with some Fe-oxides. Glass immediately adjacent to the cracks is darker, possibly due to leaching from additional crystallization.

We suggest that the healed cracks are created within the vent along the boundary between melt and seawater. This environment would likely have rapidly fluctuating temperatures and alternate between being inundated with seawater, seawater flashing to steam, and possible interaction with melt. NaCl could easily (and repeatedly) be deposited within pyroclast cavities and nearby melt would provide temperatures high enough for crystallization. This hydrothermal fluid fluxing in the cracks does not easily explain the secondary vesicles. The secondary vesicles appear to be composed of basaltic glass and may have entered the vesicles through thermal cracks, as the pyroclast porosity does not allow interconnected pathways. We hypothesize two possible origins for the secondary vesicles: (1) melt moves into cracks and vesicles, (2) hydrothermal fluid fluxing through a pyroclast reach sufficiently high temperatures to melt and incorporate glass along the

surfaces to be deposited along cracks and in vesicles. In (1) seawater flashing to steam could create a vacuum within its cavities (Cashman and Fiske, 1991) that may suck melt into cracks and vesicles. In Figure A7a the secondary vesicles appear to have inflated when entering the pre-existing vesicle as though it were at a much lower pressure.

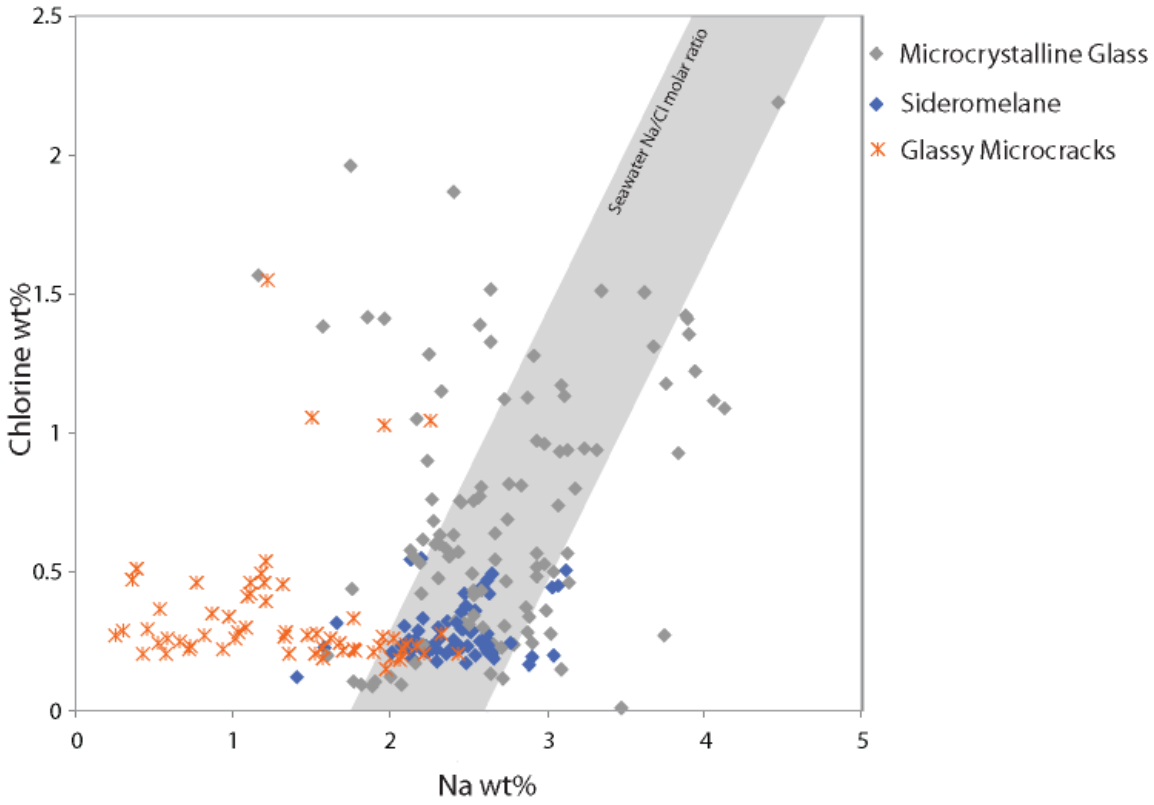

Fig. A6.- Microprobe Cl vs Na analysis of matrix glass including microcrystalline inclusions (grey diamonds), surrounding matrix (blue diamonds), and 'healed'/microcrystalline cracks (orange stars). Plot shows elevated Cl values for both microcrystalline inclusions and cracks, but depleted Na for 'healed' cracks.

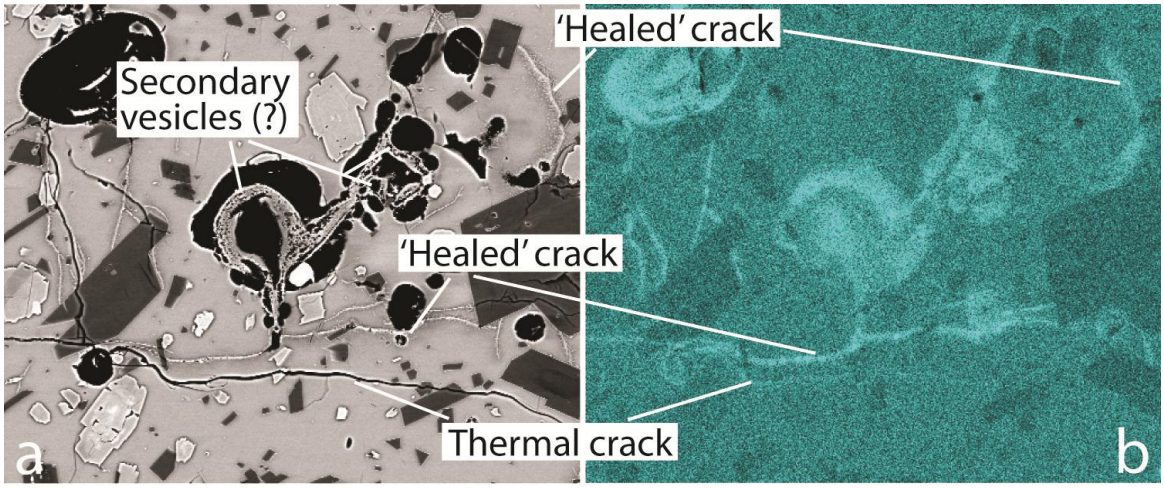

Fig. A7.- BSE of 'healed' cracks and EDS Cl x-ray map. (a) BSE images with 'healed' cracks (bright, almost white), thermal cracks (black), and odd vesicles that appear to have grown within pre-existing vesicles (secondary vesicles). (b) Cl x-ray map showing Cl enrichment in 'healed' cracks. Note the thermal cracks to not show up as Cl enriched. Also note some vesicles appear Cl enriched due to the Cl-rich epoxy used. Because of the epoxy, it is not possible to determine if the secondary vesicles are Cl-enriched.

Evidence for (2) may lie with the observed Na depletion, which may be caused by leaching from hydrothermal fluids (Seyfried, Jr., 1987). Additionally, numerous Fe-sulfides, which are commonly precipitated from hydrothermal fluids, line the very middle of the healed cracks. The unusual healed cracks and secondary vesicles may, therefore, be best explained by a combination of hydrothermal fluid fluxing and melt interaction.

APPENDIX B

LIDAR DATA COLLECTION SPECIFICATIONS

The Optech Gemini ALTM operates with specifications listed in Table A. The area scanned included 55.2km^2 consisting of 15 total passes running parallel swaths 614m wide with ~40% overlap, a target horizontal resolution of ~0.8m, pulse rate frequency of 70kHz and scan frequency of 40Hz. Three GPS reference stations (operating at 1Hz) were used during the survey; two temporary ground stations on location and one Continuously Operating Reference Station at the Redmond Airport.

Table A- Optech Gemini ALTM specifications

operating altitude	80-4000m
horizontal accuracy	1/11,000 x altitude (±1 σ)
elevation accuracy	5-10cm (±1 σ)
scan angle	≤25 degrees
scan frequency	variable to 100Hz
pulse rate frequency	33-167kHz
laser wavelength	1047nm

Optech Gemini ALTM operated by National Center for Airborne Laser Mapping

APPENDIX C

PROCEDURES FOR MORPHOLOGIC MEASUREMENT EXTRACTION FROM COLLIER FLOW FIELD DEM

Quantitative Measurements of lava flow from Airborne Lidar DEMs in GIS

The purpose of this document is to provide step by step instructions of extracting simple morphologic measurements using polygons from maps, or layers (elevation (DEMs), slope, roughness, etc.) in GIS.

The instructions below will begin with assuming the reader has a lidar dataset of elevation, a basic digital elevation model. I will also assume the reader knows how to make new layers such as hillshade, slope, aspect, and other maps.

1. Free Add-ons for ArcMap

In the following sections I will refer to two free add-ons from the web: **Hawths Tools** and **XTools Pro** that I would recommend downloading.

These could easily be found through a Google search but here are the websites:

http://www.spatialecology.com/htools/

http://www.xtoolspro.com/

2. Compartmentalize the Area of Interest (Swath Boxes)

To analyze the area of interest, in this case lava flows, create a simple polygon outlining the area and run a variety of statistical analyses on this feature (Fig. C1). This will be outlined in the next section.

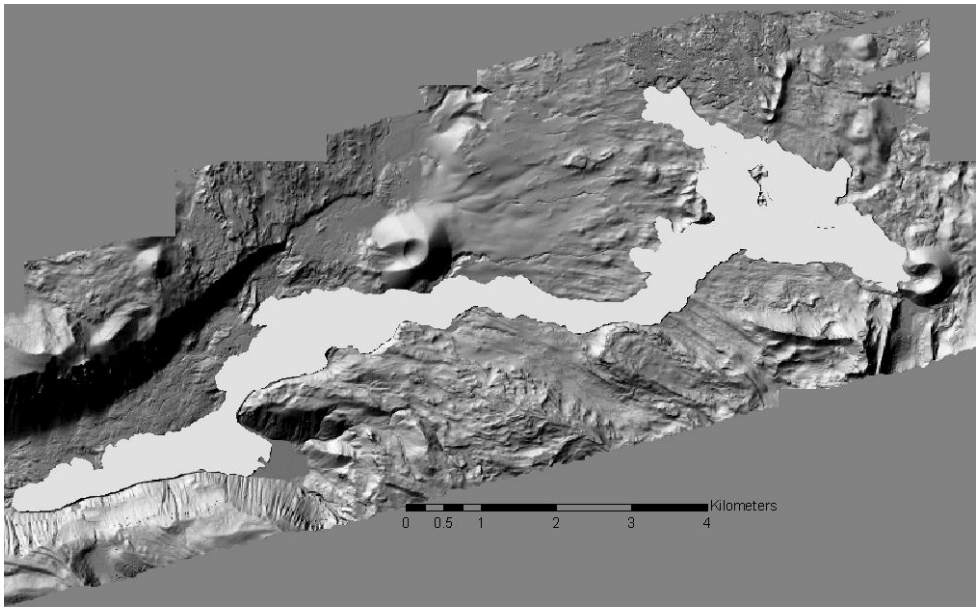

Fig. C1. Polygon of Collier flow field.

Alternatively, one could analyze the area of interest in sections by compartmentalizing it into an array of polygons (swath boxes) (Fig. C2). To do this, in ArcCatalog create a new Personal Geodatabase. Within this file, create a new feature dataset, name it, select a coordinate system and while doing this note the x/y domain. Within properties of the dataset, under the domain tab, change the min X value to zero and the max X value to 1000000, or something really large. Do the same for Y. Problems

may occur later on if this is not done. Ignore the Z and M domains. Within the dataset file in ArcCatalog, create a new feature class, name it, select Polygon Feaures under Type, and click the 'Coordinates include Z values' box. Click Next. Under Field Name add a field such as distance (or box #), to measure how far along the swath each strip is, and make the data type a short integer.

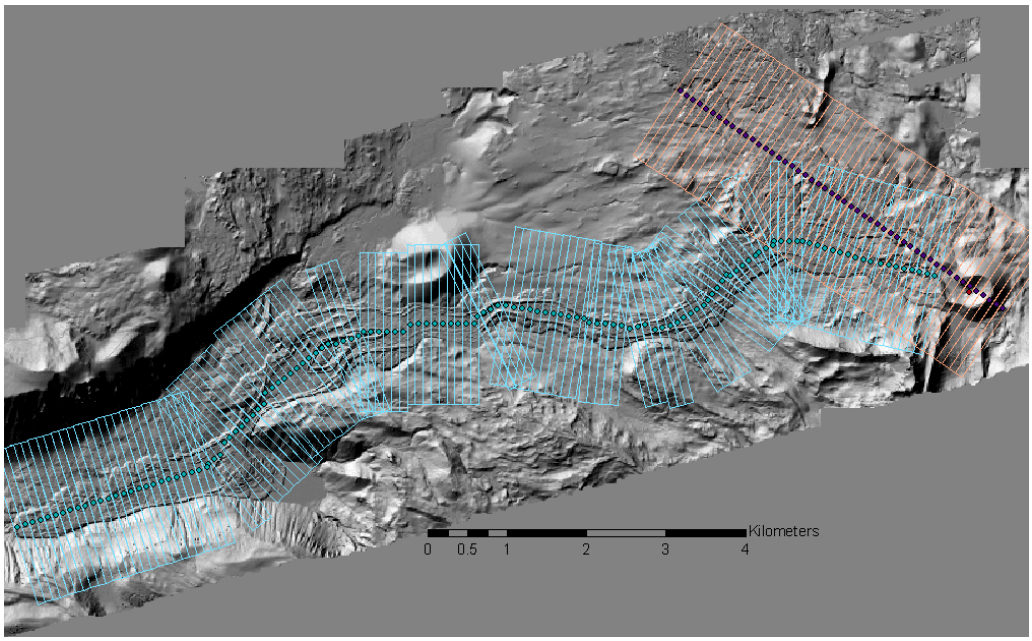

Fig. C2. Series of swath boxes of Collier flow field. Boxes are oriented normal to flow direction. Centers of boxes are symbolized by centroids (circles).

Then import the feature class using the Add data button. Again using the Editor, choose the appropriate database, and create a rectangular polygon (or whatever shape you desire). To make boxes of an exact length, make a rectangle of any size, then change the task to Modify Feature. Right click on one of the corners and choose properties. This will bring up a window with the coordinates of the polygon vertices. Change these to make the box exactly 100m by 2000m (or whatever you are shooting for). It doesn't matter

where on the map the box is located, it can be moved after the size is set. The highlighted box can be rotated with the rotate tool. Once the box is created then copy and paste as many as is required to cover the area intended for analysis. When a box is copied and pasted it is overlain exactly on top of the previous. Place the new box directly next to the previous box (to make a swath with no overlay) by moving it to the side. Go to Editor>>Move, a box will pop up allowing specific direction changes by X and Y units. Important point: to identify the order of the boxes, and later determine distances, right click on each box, go to Attributes, then change the distance field (created above) to 1 for the first box, then consecutive 2, 3, 4…etc. The first box made may have an objectID of 1 already but as more of these are made and are moved around it is important to distinguish the order of the boxes.

3. Creating Centroids for the Swath Boxes

Centroids will allow the distance to be determined from the starting point (first box) to the center of each swath box. This can be useful when comparing measurements from the swath boxes analyses with distance. For example, how slope changes with distance from the vent along the lava flow depicted above.

To create a centroid shapefile using XTools Pro, pull down the XTools Pro tab >> Feature Conversions >> Shapes to Centroids. In the window that pops up choose the Input feature layer (your swath boxes), output location and name, and keep Centroid location on Center Point.

4. Clipping Polygons from DEMs

To analyze a particular area of the DEM (i.e. lava flow, landslide, fault scarp, etc.) and exclude the surrounding topography, it seems easiest to simply make a new DEM of the area of interest. The swath boxes, described above, will analyze any DEM that falls within the area covered by the boxes. Therefore, while arranging the swath of boxes neatly over the area of interest, make sure to extend the area of the boxes past the area for analysis. A variety of clipped DEM polygons can then be created within the boxed area for analysis (Fig. C3).

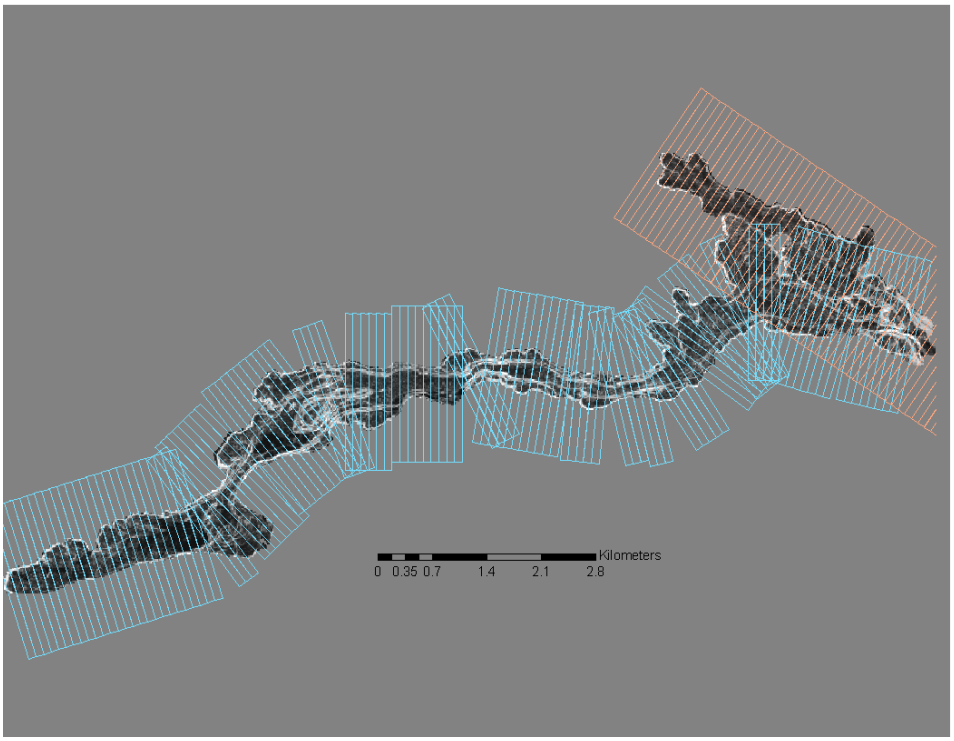

Fig. C3. Clipped slope layer of Collier lava with swath boxes.

To create a polygon layer, start by making a new shapefile in ArcCatalog. Name it accordingly, change the Feature Type to Polygon and Edit the Coordinate System to

which ever projection the dataset is in. Next import the shapefile (Add data button). Using the Editor, draw or alter the polygon to cover the desired area. Once the polygon is finished, stop editing and save changes.

Next, using the Hawths Tools add-on, pull down the Hawths Tools toolbar >> Raster Tools >> Clip Raster by Polygon. In the window that pops up choose the polygon layer just created, the unique ID field (ID) and then select the raster layer from which it is desired to clip a new raster. For example, if one wanted to pull out a new elevation layer, choose the original DEM, or if slope data is desired, choose a slope layer. Select the output folder and click OK. The raster usually takes only a few seconds to minutes to clip. Then add the new raster layer into the map.

5. Statistical Analysis

Once a raster is created with only the area intended for analysis and a feature class of segmented boxes oriented to cover the desired area everything is ready to extract data and make all the hassle of the setup outlined above worthwhile. This part is easy, just go to Spatial Analyst >> Zonal Statistics. In this window choose the swath boxes for the Zone dataset, this defines the area (or segmented area) where the statistics will be completed. The Zone field should be the field (i.e. Distance) created while creating the Feature Class. Value raster will be the base data used to pull data from, so the clipped DEM (can be slope, elevation, aspect, etc.). Make sure to check 'Ignore NoData in calculations' and choose a chart statistic to determine (mean, range, etc.).

Once run, this will create an output table of box statistics in order of distance labels (so 1 through the last box). Although only one statistic is chosen, such as mean, to analyze, the table produces several columns including area, min, max, range, mean, std, and sum. The field selected (Distance) comes up as Value. The table created is a dBase table of .dbf and can be opened in other programs, such as Excel or Jump and resaved in those formats. When opened in Excel, if some of the values do not come up, or rather come up as ############### values, do not panic. The values are there, but simply have too many integers and will appear if you widen the column.

I would like to note that the data output produced is representative of the base layer (clipped polygon) chosen for analysis. So if a slope map is chosen for the base layer the mean for each box will be the mean slope for the area covered. If an elevation base map is chosen mean elevation is received, etc. This may seem blatantly obvious at this point, but I wanted to point this out and note that the user should know how each of these layers (maps) are created if analyzing them quantitatively. There are potentially artifacts (from data point loss, gridding, etc.) in all lidar datasets and layers. A lidar user should think about the surfaces the data is representing, what the point spacing is and at what spatial resolution your maps are gridded. They should then consider what effects these factors may play on the analyses. Having said that, I have found the above technique to be quite versatile and, once the segmented boxes are set up, relatively quick in extracting usable morphological measurements.

APPENDIX D

MATLAB SCRIPTS

Below are three Matlab scripts. The first two are used for Fourier transform analyses on channel profiles. The full channel script includes only the spectrogram analysis while the representative segments script includes both spectrogram and periodogram analyses and plotting . The final script was used to fit a plane to raster data sets and determine the downslope gradient. Scripts were run in Matlab version 7.9.0 (R2009b).

1. Full west channel profile

```
% Fourier Transform analysis of collier lidar profiles.
% Profile is of the entire west channel.

% created by Nick Deardorff

close all
clear all
clc


load wchan_prof_XYZ.dat
load wchan_prof_norm_XYZ_cut.dat

data=wchan_prof_XYZ;
data2=wchan_prof_norm_XYZ_cut;

% parse data
xx = data(:,1); %distance from first point
yy = data(:,4);% elevation

figure;
L=plot(xx,yy,'.r'); % Plot the original data points
set(L,'Markersize',5) % Making the circle markers larger
set(L,'Markerfacecolor','r') % Filling in the markers
hold on
% xlim([600 1200]);
```

```
xlabel('Distance (m)');
ylabel('Elevation (m)');
title('Lava profile - Compression ridges');

[a,b]=size(data);
nfft=a; %number of points
ymax=max(xx); %data listed as y,x in data table
sampint=ymax/nfft; %sample iterval= avg spacing betwee pts
samprate = 1/sampint;

% detrend data to remove slope from analysis
z=detrend(yy);%removes best fit straight line
%z=detrend(yy,'constant');%removes mean value from each column-*Note*
                          %moves whole data set down, avg to zero
% z=detrend(yy,'linear',bp);%removes continuous, peicewise linear
trend-bp
%                            %is vector of breakpoints b/t segments
%

figure;
M=plot(xx,z,'.r'); % Plot the original x with detrended data points
set(M,'Markersize',5)
set(M,'Markerfacecolor','r')
hold on
% xlim([0 4610]);
% ylim([-40 40]);
xlabel('Distance (m)');
ylabel('Elevation change(m)');
title('Lava profile - Detrended');

%setting up taper
% [pwrdens, freqs] = pwelch(z,100,[],nfft,samprate);
%  or
[pwrdens, freqs] = pmtm(z,[],[],samprate);

figure;
loglog(freqs, pwrdens,'.r');
hold on;
xlabel('Frequency (m^-^1)');
ylabel('DFT Spectral Power (m^2)');

% figure;
% spectrogram(freqs);
% xlim([0 0.1]);

[S, F, T, P] = spectrogram(z,100,50,nfft,samprate);
% imagesc(T,F,log10(abs(S)));axis xy
% surf(T,F,log10(abs(S)));shading interp
figure;
pcolor(T,F,10*log10(abs(S)));shading interp
ylim([0 0.15]);
colorbar
```

2. Representative segments

```
% Fourier Transform analysis of collier lidar profiles.
%
% analyzing 1000m segments in representative areas with roughly
constant
% channel widths
%
% script includes analysis of both west lobe and northwest lobe
segments
% created by Nick Deardorff

close all
clear all
clc

load w_end_unit4_1441_2440.dat
load wchan_prof_2710_3709XYZ.dat
load w_seg_3865_4864.dat
load wchan_prof_4940_5939XYZ.dat
load nwchan_prof_520_1519XYZ.dat
load nw_flat_seg_1430_2429.dat
load nw_flat_seg_2857_3856.dat

% load four_in_one_prof.dat;

load prof_1000m_norm.dat;
% load prof1000m_norm.dat
% load prof_1000m_norm_lava.dat
% load prof_norm_1000m_false_surface.dat
% load prof_norm_603m_false_surface.dat

data=w_end_unit4_1441_2440;
data2=wchan_prof_2710_3709XYZ;
data3=w_seg_3865_4864;
data4=wchan_prof_4940_5939XYZ;
data5=nwchan_prof_520_1519XYZ;
data6=nw_flat_seg_1430_2429;
data7=nw_flat_seg_2857_3856;

% data_norm=prof1000m_norm;
% data_norm=prof_1000m_norm_lava;
data_norm=prof_1000m_norm;

% data_4in1=four_in_one_prof;

%% west lobe, end of unit 4, widening channel with extensional cracks,
cracks may
% not show up in profile
% starts at 1441m from the vent along the west lobe
% parse data
```

```
% data=w_end_unit4_1441_2440;

xx = data(:,1); %distance from first point
yy = data(:,4);% elevation

figure;
L=plot(xx,yy,'.k'); % Plot the original data points
set(L,'Markersize',5) % Making the circle markers larger
set(L,'Markerfacecolor','r') % Filling in the markers
hold on

[a,b]=size(data);
nfft=a; %number of points
ymax=max(xx); %data listed as y,x in data table
sampint=ymax/nfft; %sample iterval= avg spacing betwee pts
samprate = 1/sampint;

% detrend data to remove slope from analysis
z=detrend(yy);%removes best fit straight line

figure;
M=plot(xx,z,'.k'); % Plot the original x with detrended data points
set(M,'Markersize',5)
set(M,'Markerfacecolor','r')
hold on

%setting up taper
[pwrdens, freqs] = pwelch(z,200,[],nfft,samprate);
% [pwrdens, freqs] = pmtm(z,[],nfft,samprate);

figure;
loglog(freqs, pwrdens,'.r');
hold on;

[S, F, T, P] = spectrogram(z,100,50,nfft,samprate);
% imagesc(T,F,log10(abs(S)));axis xy
% surf(T,F,log10(abs(S)));shading interp
figure;
pcolor(T,F,10*log10(abs(S)));shading interp

% ylim([0 0.15]);
colorbar

%% west lobe, unit 3, relatively wide channel, right after unit 4
terminus
% starts at 2710m from the vent along the west lobe
% parse data
% data2=wchan_prof_2710_3709XYZ;

xx2 = data2(:,1); %distance from first point
yy2 = data2(:,4);% elevation
```

```
figure;
L2=plot(xx2,yy2,'.k'); % Plot the original data points
set(L2,'Markersize',5) % Making the circle markers larger
set(L2,'Markerfacecolor','b') % Filling in the markers
hold on

[c,d]=size(data2);
nfft2=c; %number of points
ymax2=max(xx2); %data listed as y,x in data table
sampint2=ymax2/nfft2; %sample iterval= avg spacing betwee pts
samprate2 = 1/sampint2;

% detrend data to remove slope from analysis
z2=detrend(yy2);%removes best fit straight line
%
datadetrended2=[xx2,z2];
figure;
M2=plot(xx2,z2,'.k'); % Plot the original data points
set(M2,'Markersize',5) % Making the circle markers larger
set(M2,'Markerfacecolor','b') % Filling in the markers
hold on

[pwrdens2, freqs2] = pwelch(z2,200,[],nfft2,samprate2);
%  or
% [pwrdens2, freqs2] = pmtm(z2,[],nfft2,samprate2);

figure;
loglog(freqs2, pwrdens2,'.b');
hold on;

[S, F, T, P] = spectrogram(z2,100,50,nfft2,samprate2);
% imagesc(T,F,log10(abs(S)));axis xy
% surf(T,F,log10(abs(S)));shading interp
figure;
pcolor(T,F,10*log10(abs(S)));shading interp
% ylim([0 0.15]);
colorbar

%%  west lobe, unit 3, narrow channel next to obsidian cliffs
% starts at 3865m from the vent along the west lobe
% parse data
% data3=w_seg_3865_4864;

xx3 = data3(:,1); %distance from first point
yy3 = data3(:,4);% elevation

figure;
L3=plot(xx3,yy3,'.k'); % Plot the original data points
set(L3,'Markersize',5) % Making the circle markers larger
set(L3,'Markerfacecolor','g') % Filling in the markers
hold on
```

```
[e,f]=size(data3);
nfft3=e; %number of points
ymax3=max(xx3); %data listed as y,x in data table
sampint3=ymax3/nfft3; %sample iterval= avg spacing betwee pts
samprate3 = 1/sampint3;

z3=detrend(yy3);%removes best fit straight line
datadetrended3=[xx3,z3];

figure;
M3=plot(xx3,z3,'.k'); % Plot the original data points
set(M3,'Markersize',5) % Making the circle markers larger
set(M3,'Markerfacecolor','g') % Filling in the markers
hold on

[pwrdens3, freqs3] = pwelch(z3,200,[],nfft3,samprate3);
%  or
% [pwrdens3, freqs3] = pmtm(z3,[],nfft3,samprate3);

figure;
loglog(freqs3,pwrdens3,'.g');
hold on;


[S, F, T, P] = spectrogram(z3,100,50,nfft3,samprate3);
% imagesc(T,F,log10(abs(S)));axis xy
% surf(T,F,log10(abs(S)));shading interp
figure;
pcolor(T,F,10*log10(abs(S)));shading interp
% ylim([0 0.15]);

%%  west lobe, unit 3, narrow channel just past obsidian cliffs
% starts at 4940m from the vent along the west lobe
% parse data
% data4=wchan_prof_4940_5939XYZ
xx4 = data4(:,1); %distance from first point
yy4 = data4(:,4);% elevation

figure;
L4=plot(xx4,yy4,'.k'); % Plot the original data points
set(L4,'Markersize',5) % Making the circle markers larger
set(L4,'Markerfacecolor','m') % Filling in the markers
hold on

[e,f]=size(data4);
nfft4=e; %number of points
ymax4=max(xx4); %data listed as y,x in data table
sampint4=ymax4/nfft4; %sample iterval= avg spacing betwee pts
samprate4 = 1/sampint4;

z4=detrend(yy4);%removes best fit straight line
```

```
datadetrended4=[xx4,z4];

figure;
M4=plot(xx4,z4,'.k'); % Plot the original data points
set(M4,'Markersize',5) % Making the circle markers larger
set(M4,'Markerfacecolor','m') % Filling in the markers
hold on

[pwrdens4, freqs4] = pwelch(z4,200,[],nfft4,samprate4);
%  or
% [pwrdens4, freqs4] = pmtm(z4,[],nfft4,samprate4);

figure;
loglog(freqs4,pwrdens4,'.m');
hold on;

%
[S, F, T, P] = spectrogram(z4,100,50,nfft4,samprate4);
% imagesc(T,F,log10(abs(S)));axis xy
% surf(T,F,log10(abs(S)));shading interp
figure;
pcolor(T,F,10*log10(abs(S)));shading interp
% ylim([0 0.15]);

figure;
loglog(freqs,pwrdens,'.r');
hold on; loglog(freqs2,pwrdens2,'.b');
hold on; loglog(freqs3,pwrdens3,'.g');
hold on; loglog(freqs4,pwrdens4,'.m');

%% northwest lobe, unit 4, very narrow channel, just outside of the
vent
% starts at 520m from the vent along the northwest lobe
% parse data
% data5=nwchan_prof_520_1519XYZ;
xx5 = data5(:,1); %distance from first point
yy5 = data5(:,4);% elevation

figure;
L5=plot(xx5,yy5,'.k'); % Plot the original data points
set(L5,'Markersize',5) % Making the circle markers larger
set(L5,'Markerfacecolor','r') % Filling in the markers
xlabel('Distance (m)');
ylabel('Elevation (m)');
hold on

[e,f]=size(data5);
nfft5=e; %number of points
ymax5=max(xx5); %data listed as y,x in data table
sampint5=ymax5/nfft5; %sample iterval= avg spacing betwee pts
samprate5 = 1/sampint5;
```

```
z5=detrend(yy5);%removes best fit straight line
datadetrended5=[xx5,z5];

figure;
M5=plot(xx5,z5,'.k'); % Plot the original data points
set(M5,'Markersize',5) % Making the circle markers larger
set(M5,'Markerfacecolor','r') % Filling in the markers
hold on

[pwrdens5, freqs5] = pwelch(z5,100,[],nfft5,samprate5);
%  or
% [pwrdens5, freqs5] = pmtm(z5,[],nfft5,samprate5);

figure;
loglog(freqs5,pwrdens5,'.r');
hold on;

%
[S, F, T, P] = spectrogram(z5,200,50,nfft5,samprate5);
% imagesc(T,F,log10(abs(S)));axis xy
% surf(T,F,log10(abs(S)));shading interp
figure;
pcolor(T,F,10*log10(abs(S)));shading interp
% ylim([0 0.15]);
% xlabel('Distance (m)');
% ylabel('Frequency (m^-^1)');
colorbar

%% northwest lobe, unit 4, after very narrow channel, when flow widens
% starts at 1430m from the vent along the northwest lobe
% parse data
%data6=nw_flat_seg_1430_2429;
xx6 = data6(:,1); %distance from first point
yy6 = data6(:,4);% elevation

figure;
L6=plot(xx6,yy6,'.k'); % Plot the original data points
set(L6,'Markersize',5) % Making the circle markers larger
set(L6,'Markerfacecolor','b') % Filling in the markers
xlabel('Distance (m)');
ylabel('Elevation (m)');
hold on

[e,f]=size(data6);
nfft6=e; %number of points
ymax6=max(xx6); %data listed as y,x in data table
sampint6=ymax6/nfft6; %sample iterval= avg spacing betwee pts
samprate6 = 1/sampint6;

z6=detrend(yy6);%removes best fit straight line
datadetrended6=[xx6,z6];
```

```
figure;
M6=plot(xx6,z6,'.k'); % Plot the original data points
set(M6,'Markersize',6) % Making the circle markers larger
set(M6,'Markerfacecolor','b') % Filling in the markers
hold on

[pwrdens6, freqs6] = pwelch(z6,200,[],nfft6,samprate6);
%  or
% [pwrdens6, freqs6] = pmtm(z6,[],nfft6,samprate6);

figure;
loglog(freqs6,pwrdens6,'.b');
hold on;

%
[S, F, T, P] = spectrogram(z6,100,50,nfft6,samprate6);
% imagesc(T,F,log10(abs(S)));axis xy
% surf(T,F,log10(abs(S)));shading interp
figure;
pcolor(T,F,10*log10(abs(S)));shading interp
% ylim([0 0.15]);
xlabel('Distance (m)');
ylabel('Frequency (m^-^1)');
colorbar

%% northwest lobe, unit 4, last segement, relatively smooth

% data7=nw_flat_seg_2857_3856;
xx7 = data7(:,1); %distance from first point
yy7 = data7(:,4);% elevation

figure;
L7=plot(xx7,yy7,'.k'); % Plot the original data points
set(L7,'Markersize',5) % Making the circle markers larger
set(L7,'Markerfacecolor','g') % Filling in the markers
xlabel('Distance (m)');
ylabel('Elevation (m)');
hold on

[e,f]=size(data7);
nfft7=e; %number of points
ymax7=max(xx7); %data listed as y,x in data table
sampint7=ymax7/nfft7; %sample iterval= avg spacing betwee pts
samprate7 = 1/sampint7;

z7=detrend(yy7);%removes best fit straight line
datadetrended7=[xx7,z7];

figure;
M7=plot(xx7,z7,'.k'); % Plot the original data points
set(M7,'Markersize',7) % Making the circle markers larger
set(M7,'Markerfacecolor','g') % Filling in the markers
```

```
hold on

[pwrdens7, freqs7] = pwelch(z7,200,[],nfft7,samprate7);
%  or
% [pwrdens7, freqs7] = pmtm(z7,[],nfft7,samprate7);

figure;
loglog(freqs7,pwrdens7,'.g');
hold on;
%
[S, F, T, P] = spectrogram(z7,100,50,nfft7,samprate7);
% imagesc(T,F,log10(abs(S)));axis xy
% surf(T,F,log10(abs(S)));shading interp
figure;
pcolor(T,F,10*log10(abs(S)));shading interp
% ylim([0 0.15]);
% xlabel('Distance (m)');
% ylabel('Frequency (m^-^1)');
colorbar
%
figure;
loglog(freqs5,pwrdens5,'.r');
hold on; loglog(freqs6,pwrdens6,'.b');
hold on; loglog(freqs7,pwrdens7,'.g');

%%
% attempt to normalize power density spectra to determine dominant
% wavelenght.

%% normalization profile
% parse data

xx_norm = data_norm(:,1); %distance from first point
yy_norm = data_norm(:,4);% elevation

figure;
L_norm=plot(xx_norm,yy_norm,'.k'); % Plot the original data points
set(L_norm,'Markersize',5) % Making the circle markers larger
set(L_norm,'Markerfacecolor','r') % Filling in the markers
hold on
% xlim([0 500]);
xlabel('Distance (m)');
ylabel('Elevation (m)');
% title('Off flow profile');
% ylim([1870 1905]);

[l,m]=size(data_norm);
nfft_norm=l; %number of points
ymax_norm=max(xx_norm); %data listed as y,x in data table
sampint_norm=ymax_norm/nfft_norm; %sample iterval= avg spacing betwee
pts
samprate_norm = 1/sampint_norm;
```

```
% detrend data to remove slope from analysis
z_norm=detrend(yy_norm);%removes best fit straight line
%
datadetrended_norm=[xx_norm,z_norm];
figure;
M_norm=plot(xx_norm,z_norm,'.k'); % Plot the original data points
set(M_norm,'Markersize',5) % Making the circle markers larger
set(M_norm,'Markerfacecolor','r') % Filling in the markers
hold on
% xlim([0 500]);
% ylim([-10 10]);
xlabel('Distance (m)');
ylabel('Elevation (m)');


[pwrdens_norm, freqs_norm] =
pwelch(z_norm,200,[],nfft_norm,samprate_norm);
% [pwrdens_norm, freqs_norm] = pmtm(z_norm,[],nfft_norm,samprate_norm);

figure;
loglog(freqs_norm, pwrdens_norm,'.k');
hold on;
xlabel('Frequency (m^-^1)');
ylabel('DFT Spectral Power (m^2)');

[S, F, T, P] = spectrogram(z_norm,50,25,nfft_norm,samprate_norm);
% imagesc(T,F,log10(abs(S)));axis xy
% surf(T,F,log10(abs(S)));shading interp
figure;
pcolor(T,F,10*log10(abs(S)));shading interp
% ylim([0 0.15]);
% xlabel('Distance (m)');
% ylabel('Frequency (m^-^1)');
colorbar

figure;
loglog(freqs,pwrdens,'.r');
hold on; loglog(freqs2, pwrdens2,'.b');
hold on; loglog(freqs3,pwrdens3,'.g');
hold on; loglog(freqs4, pwrdens4,'.m');
hold on; loglog(freqs5,pwrdens5,'.r');
hold on; loglog(freqs6, pwrdens6,'.b');
hold on; loglog(freqs7,pwrdens7,'.g');
hold on; loglog(freqs_norm,pwrdens_norm,'.k');
xlabel('Frequency (m^-^1)');
ylabel('DFT Spectral Power (m^2)');

figure;
loglog(freqs,pwrdens,'.r');
hold on; loglog(freqs2, pwrdens2,'.b');
hold on; loglog(freqs3,pwrdens3,'.g');
```

```
hold on; loglog(freqs4, pwrdens4,'.m');
hold on; loglog(freqs_norm,pwrdens_norm,'.k');
xlabel('Frequency (m^-^1)');
ylabel('DFT Spectral Power (m^2)');

figure;
loglog(freqs5,pwrdens5,'.r');
hold on; loglog(freqs6, pwrdens6,'.b');
hold on; loglog(freqs7,pwrdens7,'.g');
hold on; loglog(freqs_norm,pwrdens_norm,'.k');
xlabel('Frequency (m^-^1)');
ylabel('DFT Spectral Power (m^2)');

%%
% attempt to normalize power density spectra to determine dominant
% wavelength.

pwrnorm=pwrdens./pwrdens_norm; %matrix dimensions must agree-same # of
points
pwrnorm2=pwrdens2./pwrdens_norm;
pwrnorm3=pwrdens3./pwrdens_norm;
pwrnorm4=pwrdens4./pwrdens_norm;
pwrnorm5=pwrdens5./pwrdens_norm;
pwrnorm6=pwrdens6./pwrdens_norm;
pwrnorm7=pwrdens7./pwrdens_norm;

%Amplitude vs Frequency plots- west channel 1441-2440m
figure;subplot(2,1,1);
loglog(freqs,pwrdens,'.r');
hold on; loglog(freqs_norm,pwrdens_norm,'.k');
ylabel('DFT Spectral Power (m^2)');
subplot(2,1,2);
semilogx(freqs,pwrnorm,'.k');
hold on;
% title('Normalized Power Spectra');
ylabel('Normalized Power (DFT)');
xlabel('Frequency (m^-^1)');
% ylim([0 75]);

amp=sqrt(pwrnorm);
figure;
semilogx(freqs, amp, '.k');
ylabel('Amplitude (m)');
xlabel('Frequency (m^-^1)');

wave=1./freqs;
amp=sqrt(pwrnorm);
figure;
semilogx(wave, amp, '.k');
ylabel('Amplitude (m)');
xlabel('Wavelength (m)');
```

```
%Amplitude vs Frequency plots- west channel 2710-3709m
figure;subplot(2,1,1);
loglog(freqs2,pwrdens2,'.b');
hold on; loglog(freqs_norm,pwrdens_norm,'.k');
ylabel('DFT Spectral Power (m^2)');
subplot(2,1,2);
semilogx(freqs2,pwrnorm2,'.k');
hold on;
% title('Normalized Power Spectra');
ylabel('Normalized Power (DFT)');
xlabel('Frequency (m^-^1)');
% ylim([0 75]);

amp2=sqrt(pwrnorm2);
figure;
semilogx(freqs2, amp2, '.k');
ylabel('Amplitude (m)');
xlabel('Frequency (m^-^1)');

wave2=1./freqs2;
amp2=sqrt(pwrnorm2);
figure;
semilogx(wave2, amp2, '.k');
ylabel('Amplitude (m)');
xlabel('Wavelength (m)');

%Amplitude vs Frequency plots- west channel 3865-4864m
figure;subplot(2,1,1);
loglog(freqs3,pwrdens3,'.g');
hold on; loglog(freqs_norm,pwrdens_norm,'.k');
ylabel('DFT Spectral Power (m^2)');
subplot(2,1,2);
semilogx(freqs3,pwrnorm3,'.k');
hold on;
% title('Normalized Power Spectra');
ylabel('Normalized Power (DFT)');
xlabel('Frequency (m^-^1)');
% ylim([0 75]);

amp3=sqrt(pwrnorm3);
figure;
semilogx(freqs3, amp3, '.k');
ylabel('Amplitude (m)');
xlabel('Frequency (m^-^1)');

wave3=1./freqs3;
amp3=sqrt(pwrnorm3);
figure;
semilogx(wave3, amp3, '.k');
ylabel('Amplitude (m)');
xlabel('Wavelength (m)');
```

```
%Amplitude vs Frequency plots- west channel 4940-5939m
figure;subplot(2,1,1);
loglog(freqs4,pwrdens4,'.m');
hold on; loglog(freqs_norm,pwrdens_norm,'.k');
ylabel('DFT Spectral Power (m^2)');
subplot(2,1,2);
semilogx(freqs4,pwrnorm4,'.k');
hold on;
% title('Normalized Power Spectra');
ylabel('Normalized Power (DFT)');
xlabel('Frequency (m^-^1)');
% ylim([0 75]);

amp4=sqrt(pwrnorm4);
figure;
semilogx(freqs4, amp4, '.k');
ylabel('Amplitude (m)');
xlabel('Frequency (m^-^1)');

wave4=1./freqs4;
amp4=sqrt(pwrnorm4);
figure;
semilogx(wave4, amp4, '.k');
ylabel('Amplitude (m)');
xlabel('Wavelength (m)');

%Amplitude vs Frequency plots- northwest channel 520-1519m
figure;subplot(2,1,1);
loglog(freqs5,pwrdens5,'.r');
hold on; loglog(freqs_norm,pwrdens_norm,'.k');
ylabel('DFT Spectral Power (m^2)');
subplot(2,1,2);
semilogx(freqs5,pwrnorm5,'.k');
hold on;
% title('Normalized Power Spectra');
ylabel('Normalized Power (DFT)');
xlabel('Frequency (m^-^1)');
% ylim([0 75]);

amp5=sqrt(pwrnorm5);
figure;
semilogx(freqs5, amp5, '.k');
ylabel('Amplitude (m)');
xlabel('Frequency (m^-^1)');

wave5=1./freqs5;
amp5=sqrt(pwrnorm5);
figure;
semilogx(wave5, amp5, '.k');
ylabel('Amplitude (m)');
xlabel('Wavelength (m)');
```

```
%Amplitude vs Frequency plots- northwest channel 1430-2429m
figure;subplot(2,1,1);
loglog(freqs6,pwrdens6,'.b');
hold on; loglog(freqs_norm,pwrdens_norm,'.k');
ylabel('DFT Spectral Power (m^2)');
subplot(2,1,2);
semilogx(freqs6,pwrnorm6,'.k');
hold on;
% title('Normalized Power Spectra');
ylabel('Normalized Power (DFT)');
xlabel('Frequency (m^-^1)');
% ylim([0 75]);

amp6=sqrt(pwrnorm6);
figure;
semilogx(freqs6, amp6, '.k');
ylabel('Amplitude (m)');
xlabel('Frequency (m^-^1)');

wave6=1./freqs6;
amp6=sqrt(pwrnorm6);
figure;
semilogx(wave6, amp6, '.k');
ylabel('Amplitude (m)');
xlabel('Wavelength (m)');

%Amplitude vs Frequency plots- northwest channel 2857-3856m
figure;subplot(2,1,1);
loglog(freqs7,pwrdens7,'.g');
hold on; loglog(freqs_norm,pwrdens_norm,'.k');
ylabel('DFT Spectral Power (m^2)');
subplot(2,1,2);
semilogx(freqs7,pwrnorm7,'.k');
hold on;
% title('Normalized Power Spectra');
ylabel('Normalized Power (DFT)');
xlabel('Frequency (m^-^1)');
% ylim([0 75]);

amp7=sqrt(pwrnorm7);
figure;
semilogx(freqs7, amp7, '.k');
ylabel('Amplitude (m)');
xlabel('Frequency (m^-^1)');

wave7=1./freqs7;
amp7=sqrt(pwrnorm7);
figure;
semilogx(wave7, amp7, '.k');
ylabel('Amplitude (m)');
xlabel('Wavelength (m)');
```

3. Determining slope in swath boxes

```
%% Nick Deardorff
%
%using raster (Ascii) dataset to determine slope
%First ran box3_grid.asc through convert_ArcASC_to_xyz.m script
(included below); now data is in 3 columns.

clear all
close all
clc

% load box3_grid.xyz;
load nwbox46.xyz;

%need to clip off non-data points (i.e. elevation=0)

M=nwbox46;
% parse box b
x = M(:,1);
y = M(:,2);
z = M(:,3);

% figure
% H= plot3(x,y,z,'.k')
% set(H,'Markersize',4)
% xlabel('x-axis')
% ylabel('y-axis')
% zlabel('z-axis')
%
% figure
% hist(z,50);

%trimming z-dir
cutoff_lz = 50;
cutoff_hz = 5000;
b1z = find(z > cutoff_lz & z < cutoff_hz);

cut_x = x(b1z); cut_y = y(b1z);
cut_z = z(b1z);

% %trimming y-dir
% cutoff_ly = 4895800;
% cutoff_hy = 4900000;
% b1y = find(cut_y > cutoff_ly & cut_y < cutoff_hy);
%
% cut2_x = cut_x(b1y); cut2_y = cut_y(b1y);
% cut2_z = cut_z(b1y);
%
% cut_x=cut2_x; %so I don't have to change script below
% cut_y=cut2_y;
```

```
% cut_z=cut2_z;

figure
plot3(cut_x,cut_y,cut_z,'.k','MarkerSize',3)
xlabel('x-axis')
ylabel('y-axis')
zlabel('z-axis')
axis equal

%save as .txt for statistical analsis in Surfer
x=cut_x; %so I don't have to change script below
y=cut_y;
z=cut_z;

% xyz=[x,y,z];

%% To create .txt output file

% outfile = 'box3_grid.txt';
%
% fid=fopen(outfile, 'w');
% for i = 1:length(x)
% fprintf(fid,'%f, %f, %f\n',...
%     x(i),y(i),z(i));
% end
%
% fclose('all');

%%
%From J. Roering


% location of centroid; 596,266.437  4,893,735.031 Meters
% m=596266.437;
% n=4893735.031;
% o=2053;

% figure
% plot3(x,y,z,'.k','MarkerSize',3)
% xlabel('x-axis')
% ylabel('y-axis')
% zlabel('z-axis')
% axis equal
% hold on
% plot3(m,n,o,'.r','Markersize',5)

k=length(x);
% xloc=reshape(x,k,1); % reshapes sample dataset to vertical
% yloc=reshape(y,k,1); % so we don't need it for xyz array
% zloc=reshape(z,k,1);
A(1:k,1)=1;
```

```
A(1:k,2)=x;
A(1:k,3)=y;
p=A\z;
elev=p(1);
gradx=-1*p(2);
grady=-1*p(3);
totgrad=sqrt(p(2)^2+p(3)^2);
%the p matrix it creates is the coefficients for the equation
%z=a + bx + cy and the b and c values are the gradient vector
%(i.e., they point in the maximum 'upslope' direction for that
plane)...this
%is which the gradx and grady lines multiply by negative to get them
%pointed downslope.  The totgrad function is the magnitude of the
gradient
%vector. To define the elevation of the plane, just plug in the x,y
values
%of for the center of your swath of data and calculate it.

%% Used in above script
% Arc ASC to xyz
% Only works for a raster ASC file converted from ArcMap


% Courtesy of J. Roering

clear all
close all

fn = 'nwbox46.asc';
fid = fopen(fn);

% open output file
fidw = fopen(sprintf('%s.xyz',fn(1:end-4)),'wt');
%% read header
S = textscan(fid,'%*s %f',6);
ncols = S{1}(1);
nrows = S{1}(2);
xcor = S{1}(3);
ycor = S{1}(4);
dxy = S{1}(5);
NoData = S{1}(6);

%% read raster data
ffmt = repmat('%f',1,ncols);

for n = nrows:-1:1
   C = textscan(fid,ffmt,1);
   temp = cell2mat(C);

   id = find(temp~=-9999);
   if isempty(id)
       continue
```

```
    end
    xcoord = id.*dxy - dxy/2 + xcor;
    ycoord = zeros(1,length(xcoord)) + dxy*n - dxy/2 + ycor;
    zcoord = temp(id);

    fprintf(fidw,'%.1f %.1f %.2f\n',[xcoord' ycoord' zcoord']');
    clear C

    if mod(n,10) ==0
        if ~isempty(id)
            display(sprintf('%3.2f %% Done - %d points
extracted',(nrows-n)/nrows*100,length(id)))
        else
            display(sprintf('%3.2f %% Done',(nrows-n)/nrows*100))
        end
    end

end

fclose('all');
```

APPENDIX E

MAPPING AND GEOCHEMISTRY OF COLLIER LAVAS

162 rock samples were collected over the flow field for hand specimen, thin section, and geochemical analysis. Our sampling methods included traversing across the lava units, in transects normal to flow direction, in areas where multiple lava units were present. Samples were collected within the channel, on top of the levees, and along each unit margin identified. Transects were completed both proximally and distally to the vent (Fig. E1). In addition, transects were completed in areas of flow complexity, such as areas with multiple channels or lava lobes, within the cone, and around the breached cone material.

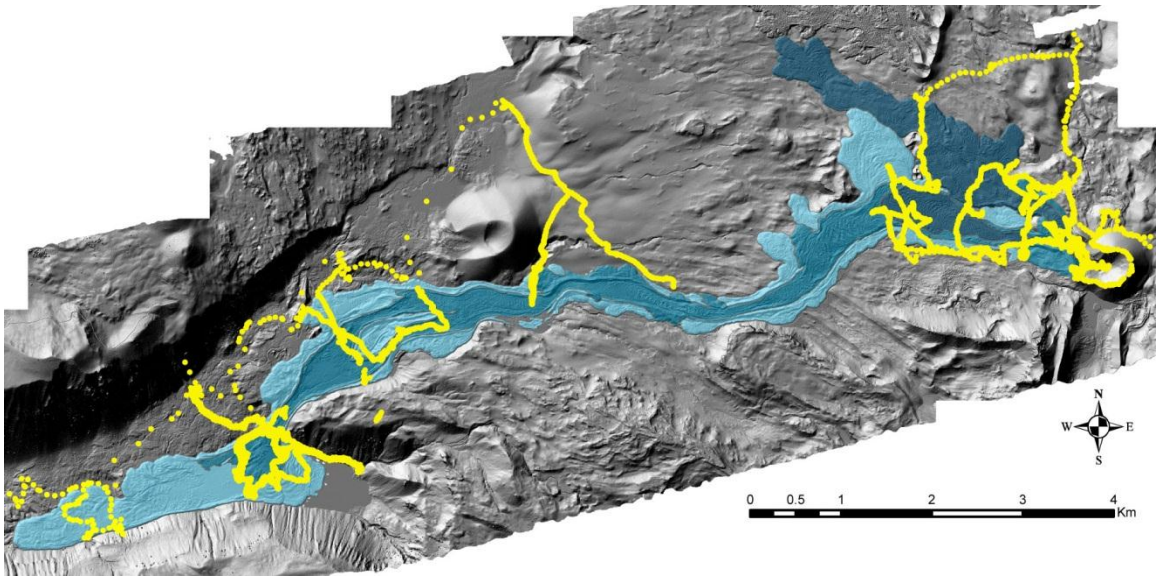

Fig. E1. Tracklogs of Collier field work. Yellow dots indicated area traversed over and around the Collier Cone lava flow field during field seasons 2008-2010.

We have analyzed 50 samples (field seasons 2008-2010) for major and trace elements, together with 47 bulk compositions from J. Schick's master's thesis (1994), to constrain the geochemical differences between lava units and to assist in mapping complex areas. Sample locations are located in Fig. E2. Lava composition fluctuated between flow units and within individual units (Fig. E2a,b).

Each lava unit is heterogeneous with variations in SiO_2 and crystallinity, creating fluctuations in major and trace (notably MgO and Ni, Cr, respectively) elements. Compositions range from basaltic andesite to dacite (55-65wt% SiO_2) throughout the flow field, and the amount of silica does not steadily increase with relative age. Silica values of Unit 2, while overlapping the range of Unit 1 (57.5-60.3wt%), have the lowest SiO_2 values, 55.4wt%. Unit 2 SiO_2 values range from 55.4-58.9wt%. Unit 3 has a more evolved composition (SiO_2- 59.0-61.3wt%), with low SiO_2 values similar to the highest measured in both Units 1 and 2. Unit 4 is the smallest lava unit and the most evolved (SiO_2- 63.3-65.1wt%). Considering only Units 1, 3 and 4 many elements have a linear dependency with SiO_2, either increasing (e.g. Na_2O, K_2O, Ba, Rb) or decreasing (e.g. Al_2O_3, FeO, MgO, Sr), as the rock composition becomes more siliceous, consistent with magma evolution through fractional crystallization and/or assimilation. Unit 2, however, deviates from any crystallization or assimilation trend with abnormally high MgO, Ni, and Cr values and slightly depleted Na_2O. MgO values for Unit 2 range from 3.4 to 6.0 wt% while all values for Units 1, 3 and 4 are <4 wt% (Fig. E3). Ni concentrations in Unit 2 lavas can exceed 180 ppm, while Ni values in Units 1 and 4 are <35 ppm and Unit 3 Ni ranges from 10-70 ppm (Fig. E4). The elevated Cr in Unit 2 follows closely with elevated

Ni; higher Cr values ranging from 65 to ~125 ppm in Unit 2, <44 ppm in Unit 1, <69 ppm in Unit 3, and <29ppm in Unit 4 (Fig. E5).

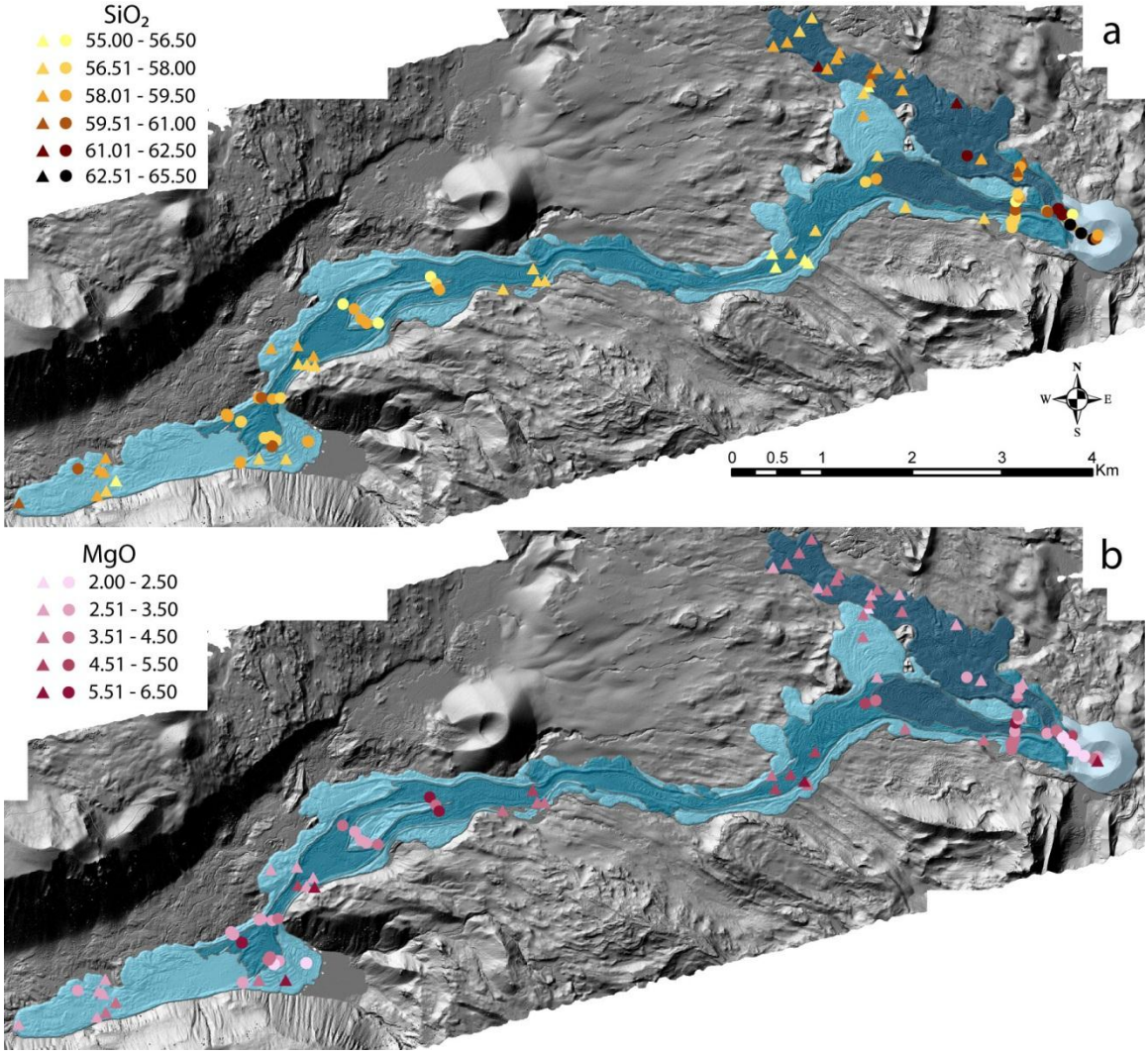

Fig. E2. Sample locations and heterogeneity of Collier lava flow field. Flow field composition is heterogeneous with fluctuations within and between each lava unit. Samples are designated, with graduated symbols, as those from this study (circles) or from Schick 1994 (triangles). (a) SiO_2 range is lowest in Unit 2 (medium blue) and highest within the cone. (b) MgO values are highest within the channel of Unit 2 (medium blue).

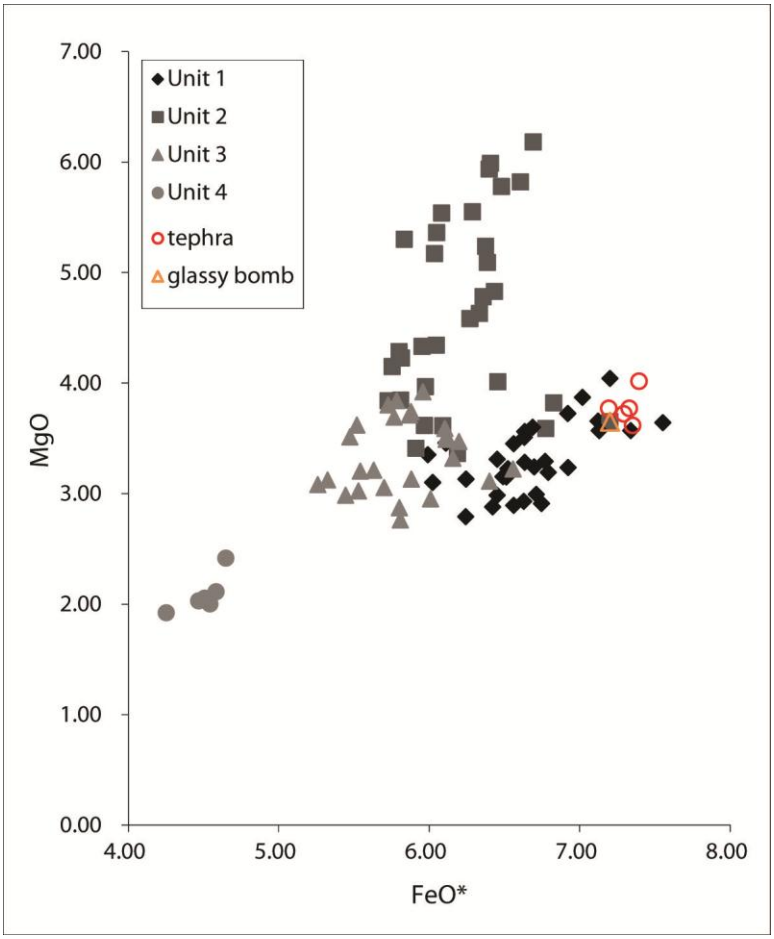

Fig. E3. Plot of MgO vs FeO*, bulk compositional analyses. Unit 2 (squares) shows elevated MgO relative to the other units. Unit 4 (closed circles) is the most evolved with the lowest MgO and FeO values. Tephra (open circles) and an ejected bomb (open triangle) analyzed show limited evolution, suggesting explosive phases preceded the lava effusion.

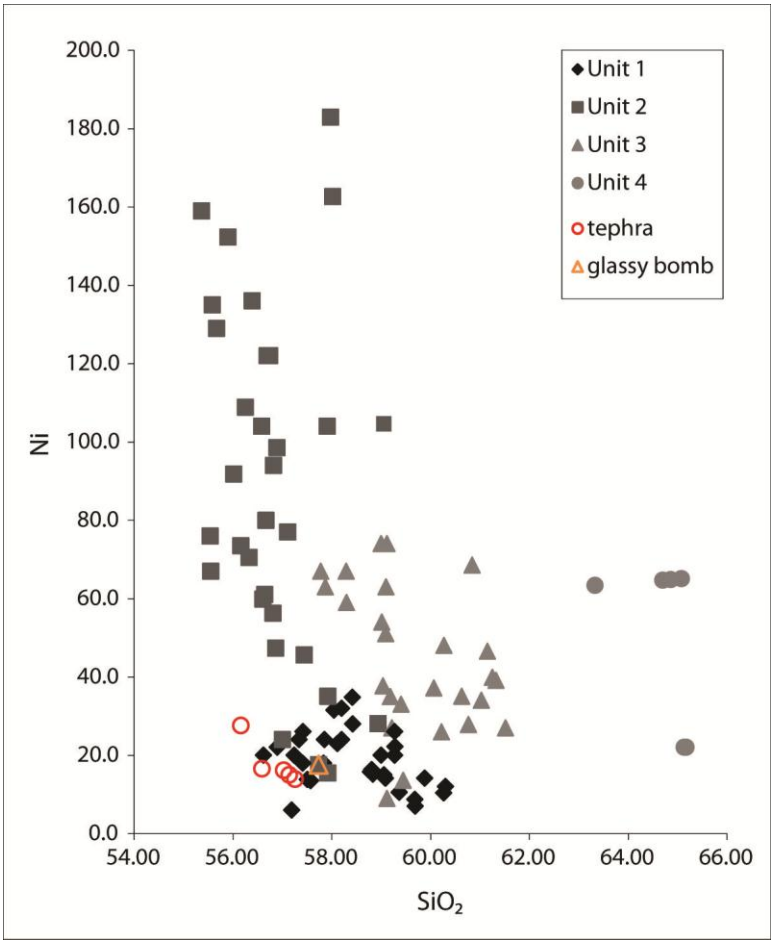

Fig. E4. Plot of Ni vs SiO_2, bulk compositional analyses. Unit 2 (squares) has elevated Ni relative to the other units. Unit 2 also has the lowest range in SiO_2. Unit 4 (closed circles) is dacite in composition, separating this unit from the others with high SiO_2.

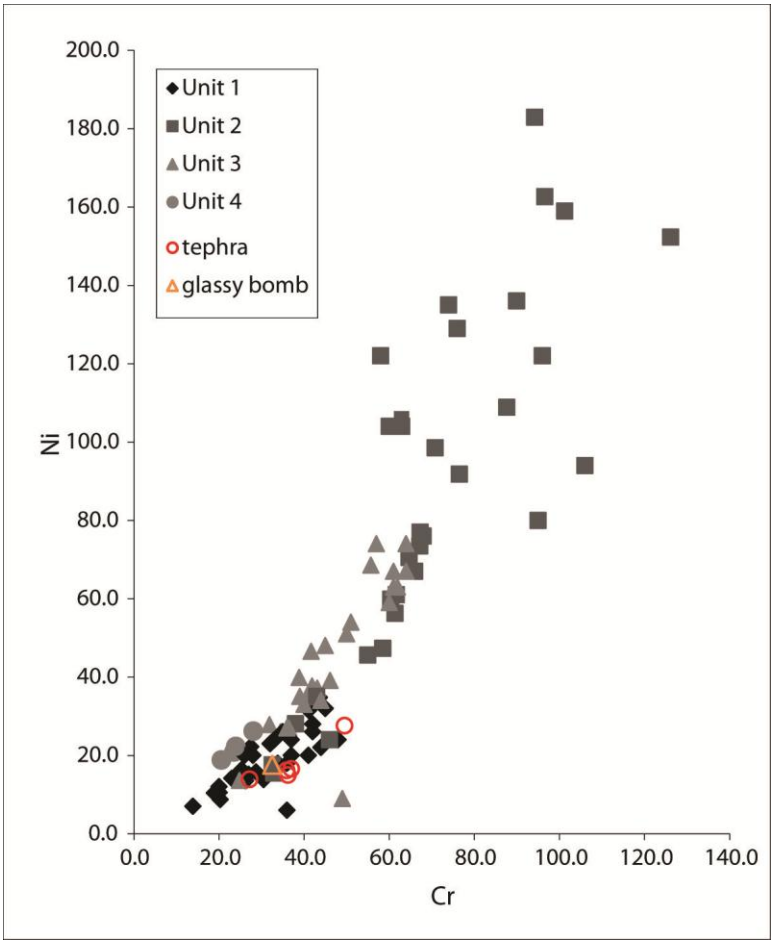

Fig. E5. Plot of Ni vs Cr, bulk compositional analyses. Unit 2 (squares) has elevated Ni and Cr due to the addition of olivine cumulate crystals.

Tephra collected east of Collier Cone (courtesy of D. Ruscitto) and one glassy bomb collected off of the lava, north of the cone were also analyzed for bulk compositions. Both the tephra and bomb plot within Unit 1 lava as some of the least evolved samples, with relatively low SiO_2, Ni and Cr, and high MgO and FeO. The ejecta compositions suggest explosive activity occurred before or during the effusion of Unit 1 lava. The tephra analyzed do not represent the entire explosive sequence.

The large range in composition over the Collier lava flow field is likely the result of eruption from a zoned magma chamber (Schick, 1994). Zoned magma chambers are believed to be layered, with more evolved compositions on top due to lower density. Upon rupture of the magma chamber, the less viscous, more mafic lava is drawn upward at a faster rate to erupt first, followed by the more silicic cap. In the case of Collier Cone, the magma chamber was likely composed of basaltic andesite magma with a dacite cap (Schick, 1994). The eruption initiated with the rupture of the dacite cap and expulsion of Unit 1 lava from the magma chamber. Unit 2 was likely of similar melt composition to Unit 1, but entrained olivine cumulates from along the walls or floor of the magma chamber, reducing SiO_2 and increasing MgO, Ni, and Cr. Unit 3 tapped more evolved magma, likely produced from mixing between Unit1 (basaltic andesite) and Unit 4 (dacite) magma (Schick, 1994). The most evolved dacite magma was last to erupt, which contained inclusions of mafic magma of similar composition to Unit 1.

APPENDIX F

COLLIER LAVA SAMPLES BULK GEOCHEMISTRY

Normalized geochemical data for Collier Cone lava samples.

Sample # CCND	Lava Unit	SiO_2	TiO_2	Al_2O_3	FeO*	MnO	MgO	CaO	Na_2O	K_2O	P_2O_5
01-002	unit 1	59.06	1.03	17.74	6.64	0.12	3.28	6.49	4.38	1.13	0.14
02-004	unit 1	59.68	1.03	17.54	6.45	0.12	2.98	6.22	4.61	1.24	0.14
03-05b	unit 2	58.94	0.94	18.05	6.19	0.11	3.36	6.70	4.42	1.15	0.13
04-006	unit 2	56.60	0.82	19.84	5.73	0.10	3.84	8.10	3.93	0.92	0.11
19-010	unit 3	60.22	0.86	17.92	5.70	0.11	3.05	6.26	4.43	1.32	0.12
20-011	unit 3	59.45	1.01	17.65	6.40	0.12	3.11	6.38	4.56	1.19	0.14
22-015	unit 3	60.77	0.85	17.67	5.53	0.11	3.02	5.99	4.55	1.38	0.13
23-014	unit 2	57.11	0.88	18.54	6.27	0.11	4.58	7.39	4.08	0.92	0.12
25-017	unit 2	56.25	0.85	18.58	6.38	0.11	5.24	7.67	3.96	0.85	0.11
26-018	unit 1	57.50	1.09	17.96	6.92	0.13	3.72	7.16	4.45	0.92	0.14
28-019	unit 1	57.83	1.00	18.29	6.63	0.12	3.51	7.14	4.35	1.00	0.13
29-020	unit 2	56.65	0.84	19.51	5.97	0.11	3.97	7.94	3.99	0.92	0.11
31-022	unit 2	57.92	1.04	17.94	6.78	0.12	3.59	7.02	4.46	0.99	0.14
33-025	unit 3	60.07	0.84	18.02	5.54	0.11	3.20	6.36	4.42	1.31	0.12
34-026	unit 2	55.90	0.82	18.36	6.41	0.12	5.99	7.60	3.87	0.83	0.11
36-029	unit 1	59.36	1.03	17.57	6.49	0.12	3.15	6.37	4.59	1.17	0.14
37-030	unit 1	57.57	1.10	17.82	7.12	0.13	3.66	7.04	4.48	0.93	0.14
42-037	unit 3	61.33	0.75	17.60	5.26	0.10	3.08	5.81	4.47	1.48	0.11
51-054	unit 4	63.33	0.70	17.23	4.65	0.10	2.41	5.11	4.64	1.72	0.11

Sample # CCND	Lava Unit	SiO_2	TiO_2	Al_2O_3	FeO*	MnO	MgO	CaO	Na_2O	K_2O	P_2O_5
54-057	unit 2	56.02	0.87	19.07	6.36	0.11	4.78	7.91	3.95	0.83	0.11
72-084	unit 2	56.89	0.88	18.39	6.43	0.11	4.83	7.33	4.07	0.94	0.12
74-085	unit 3	59.22	0.92	17.96	6.16	0.11	3.32	6.55	4.45	1.20	0.13
79-091	unit 3	59.18	0.92	17.87	6.11	0.11	3.49	6.57	4.43	1.18	0.13
80-093	unit 3	59.04	0.92	17.97	6.10	0.11	3.59	6.63	4.35	1.16	0.13
82a-102	unit 2	55.36	0.82	18.83	6.40	0.11	5.94	7.90	3.76	0.78	0.11
83-103	unit 2	56.81	0.83	19.62	5.81	0.11	3.85	7.95	3.98	0.93	0.11
84-104	unit 2	58.02	0.78	17.57	6.08	0.11	5.54	6.60	4.08	1.10	0.11
85-116	unit 2	56.33	0.84	19.42	6.05	0.11	4.34	7.99	3.94	0.86	0.11
86-118	unit 1	59.09	1.03	17.73	6.52	0.12	3.22	6.44	4.54	1.15	0.14
87-119	unit 1	58.83	1.01	17.93	6.45	0.12	3.31	6.71	4.41	1.08	0.14
88-121	unit 1	58.05	0.94	18.73	6.11	0.11	3.45	7.16	4.27	1.05	0.13
89-124	unit 2	56.16	0.81	19.78	5.80	0.11	4.28	8.22	3.89	0.85	0.11
123-127	unit 1	59.69	1.08	17.42	6.63	0.12	2.93	6.14	4.62	1.23	0.15
126-039	unit 2	57.74	1.06	17.69	7.20	0.12	3.65	7.01	4.44	0.95	0.14
127-040	unit 3	61.15	0.74	17.65	5.32	0.10	3.12	5.95	4.39	1.46	0.11
128-041	unit 3	61.25	0.77	17.52	5.44	0.10	2.98	5.92	4.43	1.46	0.12
129-042	unit 4	65.08	0.67	16.44	4.47	0.10	2.03	4.38	4.80	1.92	0.11
130-043	unit 4	64.86	0.65	16.56	4.51	0.10	2.05	4.48	4.76	1.91	0.11
131-044	unit 4	64.70	0.68	16.57	4.58	0.10	2.11	4.50	4.77	1.88	0.11
132-045	unit 3	60.84	0.74	17.47	5.47	0.10	3.51	6.00	4.34	1.41	0.11
138-131	unit 1	59.88	1.00	17.26	6.71	0.12	2.99	6.06	4.57	1.26	0.15
139-132	unit 1	58.78	1.01	17.67	6.77	0.12	3.29	6.66	4.45	1.12	0.14

Sample # CCND	Lava Unit	SiO_2	TiO_2	Al_2O_3	FeO*	MnO	MgO	CaO	Na_2O	K_2O	P_2O_5
140-134	unit 2	57.44	0.86	19.10	5.97	0.11	3.62	7.72	4.08	0.98	0.12
146-148	unit 1	58.42	0.90	18.39	6.18	0.11	3.42	7.09	4.27	1.10	0.13
150-155	unit 1	60.27	1.02	17.14	6.56	0.12	2.89	5.97	4.61	1.28	0.14
152-157	unit 2	56.87	0.86	19.44	6.09	0.10	3.61	7.97	4.00	0.94	0.11
159-167	unit 2	57.98	0.78	17.22	6.48	0.11	5.78	6.42	4.02	1.11	0.11
161-170	unit 1	59.28	0.97	17.75	6.51	0.11	3.15	6.48	4.43	1.18	0.13
162-171	unit 1	58.81	1.03	17.55	6.92	0.12	3.23	6.59	4.51	1.10	0.14

APPENDIX G

COLLIER LAVA SAMPLES TRACE ELEMENT GEOCHEMISTRY

Bulk composition, unnormalized trace elements (values in weight %) for Collier Cone lava samples

Sample # CCND	Ni	Cr	Ba	Rb	Sr
01-002	15.03	25.70	358.00	19.50	490.20
02-004	8.72	20.30	379.60	21.50	475.70
03-05b	28.07	38.00	355.80	21.00	493.80
04-006	59.86	60.40	285.60	15.90	558.80
19-010	25.92	34.50	391.80	24.30	467.00
20-011	13.62	24.80	370.80	20.30	483.40
22-015	27.80	31.90	412.70	25.20	455.60
23-014	76.99	67.30	293.00	15.80	517.50
25-017	108.87	87.70	266.20	14.10	519.80
26-018	13.79	30.50	299.00	14.10	511.50
28-019	17.98	33.80	313.80	16.30	511.70
29-020	61.00	61.70	282.30	15.80	539.70
31-022	15.44	32.90	316.60	16.10	505.90
33-025	37.12	43.10	382.00	23.50	464.60
34-026	152.27	126.20	261.40	14.00	515.70
36-029	10.52	20.10	358.30	20.00	478.10
37-030	13.53	26.30	303.90	15.40	508.80
42-037	39.06	46.10	416.60	27.60	431.30
51-054	26.22	28.10	481.20	32.90	404.00
54-057	91.77	76.50	262.40	13.70	542.50
72-084	98.49	70.80	291.00	16.20	507.20
74-085	27.00	36.40	356.00	21.20	478.80
79-091	34.96	41.00	355.20	20.70	481.70
80-093	37.71	41.90	347.10	20.30	481.00
82a-102	158.96	101.30	248.10	12.40	530.00
83-103	56.27	61.40	285.80	16.30	543.70
84-104	162.65	96.60	330.90	19.90	471.40
85-116	70.52	64.70	268.00	14.80	546.30
86-118	14.15	23.40	351.50	19.70	483.20

Sample # CCND	Ni	Cr	Ba	Rb	Sr
87-119	15.15	27.00	342.20	19.00	495.70
88-121	31.54	41.10	320.10	18.00	511.10
89-124	73.50	67.20	265.60	14.80	552.60
123-127	7.03	13.90	383.10	21.70	472.90
126-039	17.60	32.50	313.90	16.40	517.70
127-040	46.50	41.70	419.20	28.20	445.50
128-041	39.90	38.90	424.90	28.60	446.80
129-042	18.80	20.60	532.20	38.10	364.20
130-043	22.30	24.00	531.30	37.50	373.10
131-044	20.90	23.50	526.30	37.40	374.50
132-045	68.50	55.70	408.50	27.30	446.00
138-131	14.10	23.00	386.00	23.60	471.70
139-132	15.80	28.70	350.40	18.80	496.30
140-134	45.60	55.00	305.00	17.90	538.70
146-148	34.80	43.60	334.80	19.60	512.20
150-155	10.40	18.90	384.70	24.10	462.80
152-157	47.30	58.50	295.40	17.30	553.60
159-167	182.90	94.20	334.80	20.80	469.60
161-170	22.20	27.50	363.00	21.40	490.50
162-171	16.30	25.30	356.60	20.10	498.30

REFERENCES CITED

Alletti M., Baker D. R., Freda C. (2007) Halogen diffusion in a basaltic melt. Geochimica et Cosmochimica Acta. 71: 3570–3580.

Applegarth L. J., Pinkerton, H., James, M. R., Calvari, S. (2010) Lava flow superposition: The reactivation of flow units in compound 'a'a flows. J. Volcanol. Geotherm. Res.194:100–106.

Baker B. H., McBirney A. R. (1986) Liquid Fractionation. Part III: Geochemistry of Zoned Magmas and the Compositional Effects of Liquid Fractionation. J. Volcanol. Geotherm. Res. 91(B6): 6091-6112.

Baker, E. T., Embley, R. W., Walker, S. L., Resing, J. A., Lupton, J. E., Nakamura, K.-I., de Ronde, C. E. J., Massoth, G. J. (2008) Hydrothermal activity and volcano distribution along the Mariana arc, J. Geophys. Res., 113, B08S09, doi:10.1029/2007JB005423.

Biot, M. A. (1961) Theory of folding of stratified viscoelastic media and its implication in tectonics and orogenesis. Geol. Soc. Amer. Bul. 72: 1595-1620.

Booth, A. M., Roering, J. J., Perron, J. T. (2009) Automated landslide mapping using spectral analysis and high-resolution topographic data: Puget Sound lowlands, Washington, and Porland Hills, Oregon. Geomorphology. 109: 132-147. doi:10.1016/j.geomorph.2009.02.027.

Boudreau, B., Algar, C., Johnson, B., Croudace, I., Reed, A., Furukawa, Y., Dorgan, K. M., Jumars, P. A., Grader, A. S. (2005) Bubble Growth and rise in soft sediments. *Geology*, 33: 517-520, doi: 10.1130/G21259.1.

Borgia, A., Linneman, S., Spencer, D., Morales, L. D., Andre, J. B. (1983) Dynamics of lava fronts, Arenal Volcano, Costa Rica. J. Volcanol. Geotherm. Res. 19: 303-329.

Borgia, A., Linneman, S. R. (1990) On the evolution of lava flows and the growth of volcanoes. In: Fink JH (ed) Lava flows and domes. Springer, Berlin Heidelberg New York, pp 208–243.

Burkhard, D. J. (2001) Crystallization and Oxidation of Kilauea Basalt Glass: Processes during Reheating Experiments. Journal of Petrology. 42(3):507-527.

Butterfield, D. A., Resing, J. A., Chadwick, W. W., Embley, R. W., Lupton, J. E., Nakamura, K., Lilley, M. D., Huder, J. A. (2007) Sulfur Lakes and Sulfur-rich Volcanic Hydrothermal Systems on the Mariana Arc. Eos Trans. AGU, 88(52), Fall Meet. Suppl., Abstract V34B-03.

Butterfield, D. A., Resing, J. A., Roe, K. K., Christensen, M., Embley, R. W., Lupton, J. E., Chadwick, W. (2009) Chemical properties and hydrothermal processes on the first two directly sampled deep-sea eruptions. Eos Trans. AGU, 90(52), Fall Meet. Suppl., Abstract V431-06.

Büttner, R., Dellino, P., La Volpe, L., Lorenz, V., Zimanowski, B. (2002) J. Geophys. Res., 107(B11): 2277, doi:10.1029/2001JB000511.

Calvari, S., Neri, M., Pinkerton, H. (2002) Effusion rate estimations during the 1999 summit eruption on Mount Etna, and growth of two distinct lava flow fields. J. Volcanol. Geotherm. Res. 119: 107-123.

Cas, R. A. F. (1992) Submarine Volcanism: Eruption Styles, Products, and Relevance to Understanding the Hot-Rock Successions to Volcanic-Hosted Massive Sulfide Deposits. Economic Geology, 87: 511-541.

Cashman, K. V., Fiske, R. S. (1991) Fallout of Pyroclastic Debris from Submarine Volcanic Eruptions. Science. 253(5017): 275-280.

Cashman, K. V., Blundy, J. (2000) Degassing and crystallization of ascending andesite and dacite. Phil. Trans. R. Soc. Lond. A. 358: 1487-1513.

Cashman, K. V. (2004) Volatile controls on magma ascent and eruption. AGU Monogr 150:109–124

Cashman, K. V., Kerr, R. C., Griffiths R. W. (2006) A laboratory model of surface crust formation and disruption on lava flows through non-uniform channels. Bull. Volcanol. 68: 753-770.

Cashman, K. V., Soule, S. A., Deligne, N. I., Dietterich, H. R., Deardorff, N. D., Mackey, B. (submitted) Lidar - A New Tool for Studying Lava Flows. In review with Geosphere.

Castro, J., Cashman, K. V. (1999) Constraints on rheology of obsidian lavas based on mesoscopic folds. J. of Struct. Geol. 21:807-819.

Chadwick, W. W., Jr., Cashman, K. V., Embley, R. W., Matsumoto, H., Dziak, R. P., de Ronde, C. E. J., Lau, T. K., Deardorff, N. D., Merle, S. G. (2008) Direct video and hydrophone observations of submarine explosive eruptions at NW Rota-1 volcano, Mariana arc, J. Geophys. Res. 113, B08S10, doi:10.1029/2007JB005215.

Chadwick, W. W., Dziak, R. P., Baker, E. T., Cashman, K. V., Embley R. W., Ferrini, V., de Ronde, C. E., Butterfield, D. A., Deardorff, N., Haxel, J. H., Matsumoto, H., Fowler, M. J., Walker, S. L., Bobbitt, A. M, Merle, S. G. (2009) Continuous, Long-term, Cyclic, Varied Eruptive Activity Observed at NW Rota-1 Submarine Volcano, Mariana Arc. Eos Trans. AGU. 90(52), Fall Meet. Suppl., Abstract V44B-03

Chadwick, W. W., Jr., Dziak, R. P., Haxel, J. H., Embley, R. W., Matsumoto, H. (submitted), Submarine landslide triggered by volcanic eruption recorded by in-situ hydrophone. In review with Nature Geoscience.

Cigolini, C., Borgia, A., Casertano, L. (1984) Inter crater activity, aa blocklava, viscosity and flow dynamics: Arenal volcano, Costa Rica. J Volcanol Geotherm Res. 20:155–176.

Cioni, R., Funedda, A. (2005) Structural geology of crystal-rich, silicic lava flows: A case study from San Pietro Island (Sardinia, Italy) In Manga M, Venture G (eds) Kinematics and dynamics of lava flows. Geological Society of America Special Paper 396:1-14.

Clague, D. A., Batiza, R., Head III, J. W., Davis, A. S. (2003a) Pyroclastic and Hydroclastic Deposits on Loihi Seamount, Hawaii. In: White, J., Smellie, J., Clague, D. (ed) Explosive Subaqueous Volcanism, Geophysical Monograph 140, AGU, Washington, DC, pp 73-95.

Clague, D. A., Davis, A. S. (2003b) Submarine Strombolian Eruptions on the Gorda Mid-Ocean Ridge. In: White, J., Smellie, J., Clague, D. (ed) Explosive Subaqueous Volcanism, Geophysical Monograph 140, AGU, Washington, DC, pp 111-127.

Clague, D. A., Paduan, J. B., Davis, A. S. (2009a) Widespread strombolian eruptions of mid-ocean ridge basalt. J Volcanol Geotherm Res. 180: 171–188.

Clague, D. A., Rubin, K. H., Keller, N. S. (2009b) Products of Submarine Fountains and Bubble-burst Eruptive Activity at 1200m on West Mata Volcano, Lau Basin. Eos Trans. AGU, 90(52), Fall Meet. Suppl., Abstract V43I-02

Coltelli, M., Proietti, C., Branca, S., Marsella, M., Andronico, D., Lodato, L. (2007) Analysis of the 2001 lava flow eruption of Mt. Etna from three-dimensional mapping Journal of Geophysical Research. 112: F02029, doi:10.1029/2006JF000598.

Costa, A. (2005), Viscosity of high crystal content melts: Dependence on solid fraction, Geophys. Res. Lett. 32: L22308. doi:10.1029/2005GL024303.

Crisci, G. M., Iovine, G., Di Gregoria, S., Lupiano, V. (2008) Lava-flow hazard on the SE flank of Mt Etna (Southern Italy). J Volcanol Geotherm Res. 177(4): 778-796.

de Silva, S. L., Self, S., Francis, P. W., Drake, R. E., Ramirez, C. R. (1994) Effusive silicic volcanism in the Central Andes: the Chao dacite and other young lavas of the Altiplano-Puno volcanic Complex. J. Geophys. Res. 99(B9):17,805-17,825.

Dimroth, E., Yamagishi, H. (1987) Criteria for the recognition of ancient subaqueous pyroclastic rocks. Report of the Goelogical Survey of Hokkaido. 58: 55-58.

D'Oriano, C., Cioni, R., Bertagnini, A., Andronico, D., Cole, P. D. (2011) Dynamics of ash-dominated eruptions at Vesuvius: the post-512 AD AS1a event. Bull Volcanol DOI: 10.1007/s00445-010-0432-1.

Dziak, R. P., Embley, R. W., Baker, E. T., Chadwick, Jr., W. W., Resing, J. A., Matsumoto, H., Haxel, J. H. Walker, S. L., Bohnenstiehl, D. R. (2009), Long-term explosion records from two erupting submarine volcanoes in the Mariana and Tonga island-arcs, Eos Trans. AGU, 90(52), Fall Meet. Suppl., Abstract V44B-02

Embley, R. W., et al., (2006) Long-term eruptive activity at a submarine arc volcano. Nature. 441: 494-497, doi:10.1038/nature04762.

Erlund, E., Cashman, K., Wallace, P., Pioli, L., Rosi, M., Johnson, E., Delgado Granados, H. (2010) Compositional evolution of magma from Parícutin Volcano, Mexico: The tephra record. J. Volcanol. Geotherm. Res. 197: 167–187.

Favalli, M., Tarquini, S., Fornaciai, A., Boscki, E. (2009a) A new approach to risk assessment of lava flow at Mount Etna. Geology. 37:1111-1114. doi: 10.1130/G30187A.1.

Favalli, M., Mazzarini, F., Pareschi, M. T., Boscki, E. (2009b) Topographic control on lava flow paths at Mount Etna, Italy: Implications for hazard assessment J. Geophys. Res. 114: F01019. doi:10.1029/2007JF000918.

Favalli, M., Harris, A. J. L., Fornaciai, A., Pareschi, M. T., Mazzarini, F. (2010a) The distal segment of Etna's 2001 basaltic lava flow. Bull Volcanol. 72: 119-127. doi: 10.1007/s00445-009-0300-z.

Favalli, M., Fornaciai, A., Mazzarini, F., Harris, A., Neri, M., Behncke, B., Parescki. M. T., Tarquini, S., Boschi, E. (2010b) Evolution of an active lava flow field using mutitemporoal LIDAR acquisition. J. Geophys. Res. 115: B11203. doi:10.1029/2010JB007463.

Fink, J. H., Fletcher, R. C. (1978) Ropy pahoehoe: surface folding of a viscous fluid. J. Volcanol. Geotherm. Res. 4:151-170.

Fink, J. H. (1980) Surface folding and viscosity of rhyolite flows. Geology. 8: 250-254.

Fink, J. H., Griffiths, R. W. (1990) Radial spreading of viscous-gravity currents with solidifying crust. J. Fluid Mech. 221: 485– 509.

Fiske, R. S., Naka, J., Iizasa, K., Yuasa, M., Klaus, A. (2001) Submarine silicic caldera at the front of the Izu-Bonin arc, Japan: Voluminous seafloor eruptions of ryholite pumice. Geological Society of America Bulletin.113: 813-824.

Fornaciai, A., Behncke, B., Favalli, M., Neri, M., Tarquini, S., Boschi, E. (2010) Detecting short-term evolution of Etnean scoria cones: a LIDAR-based approach. Bull Volcanol. 72:1209–1222. DOI 10.1007/s00445-010-0394-3.

Giordano, D., Nichols, A. R. L., Dingwell, D. B. (2005) Glass transition temperatures of natural hydrous melts: a relationship with shear velocity and implications for welding process. J. Volcanol. Geotherm. Res. 142: 105-118.

Gregg, T. K. P., Fink, J. H., Griffiths, R. W. (1998) Formation of multiple fold generations on lava flow surfaces: Influence of strain rate, cooling rate, and lava composition. J. Volcanol. Geotherm. Res. 80: 281-292.

Gregg, T. K. P., Fink, J. H. (2000) A laboratory investigation into the effects of slope on morphology. J. Volcanol. Geotherm. Res. 96: 145-159.

Griffiths, R. W., Fink, J. H. (1993) Effects of surface cooling on the spreading of lava flows and domes. J. Fluid Mech. 252: 667–702.

Griffiths, R. W., Fink, J. H. (1997) Solidifying Bingham extrusions: A model for the growth of silicic lava domes. J. Fluid Mech. 347: 13– 36.

Griffiths, R. W., Kerr, R. C., Cashman, K. V. (2003), Patterns of solidification in channel flows with surface cooling. J. Fluid Mech. 496: 33–62.

Guest, J. E., Kilburn, C. R. J., Pinkerton, H., Duncan, A. M. (1987) The evolution of lava flow fields: observations of the 1981 and 1983 eruptions of Mount Etna, Sicily. Bull. Volcanol. 49: 527-540.

Harris, A. J. L., Flynn, L. P., Matias, O., Rose, W. I., Cornejo, J. (2004) The evolution of an active silicic lava flow field: an ETM+ perspective. J. Volcanol. Geotherm. Res. 135:147– 168.

Harris, A. J. L., J. Dehn, and S. Calvari (2007), Lava effusion rate definition and measurement: A review, Bull. Volcanol. 70: 1–22, doi:10.1007/s00445-007-0120-y.

Harris, A., Ripepe, M. (2007a). Synergy of multiple geophysical approaches to unravel explosive eruption conduit and source dynamics – A case study from Stromboli. Chemie der Erde. 67: 1-35.

Harris, A., Ripepe, M. (2007b) Temperature and dynamics of degassing at Stromboli. J. Geophys. Res. 112, B03205, doi:10.1029/2006JB004393,

Head III, J. W., Wilson, L. (2003) Deep submarine pyroclastic eruptions: theory and predicted landforms and deposits. J. Volcanol. Geotherm. Res. 121: 155-193.

Heiken, G. H (1972) Morphology and petrography of volcanic ashes. Geological Society of America Bulletin, 83: 1961-1988.

Heiken, G. (1978) Characteristics of Tephra from Cinder Cone, Lassen Volcanic National Park, California. Bulletin of Volcanology. 41(2): 119-130.

Hofton, M. A., Malavassi, E., Blair, J. B. (2006) Quantifying recent pyroclastic and lava flows at Arenal Volcano, Costa Rica, using medium-footprint lidar. J. Geophys. Res. 33: L21306. doi:10.1029/2006GL027822.

Hon, K., Kauahikaua, J., Denlinger, R., Mackay, K. (1994) Emplacement and inflation of pahoehoe sheet flows: Observations and measurements of active lava flows on Kilauea Volcano, Hawaii. Geol. Soc. Am. Bull. 106: 351-370.

Hulme, G. (1974) The interpretation of lava flow morphology. Geophys. J. R. Astron. Soc. 39: 361-383.

Kauahikaua, J., Cashman, K. V., Mattox, T. N., Heliker, C. C., Hon, K. A., Mangan, M. T., Thornber, C. R. (1998) Observations on basaltic lava streams in tubes from Kilauea Volcano, island of Hawai'i. J. Geophys. Res. 103: 27303-27323.

Kauahikaua, J., Sherrod, D. R., Cashman, K. V., Heliker, C., Hon, K., Mattox, T. N., Johnson, J. A. (2003) Hawaiian lava-flow dynamics during the Pu'u'O'o-Kupaianaha eruption: A tale of two decades. U.S. Geological Survey Professional Paper. 1676: 63-88.

Kerr, R. C., Griffish, R. W., Cashman, K. V. (2006) Formation of channelized lava flows on an unconfined slope. J. Geophys. Res. 111: B10206. doi:10.1029/2005JB004225.

Kerr, R. C., Lyman, A. W. (2007) Importance of surface crust strength during the flow of the 1988-1990 andesite lava of Lonquimay Volcano, Chile. J. Geophys. Res. 112:B03209. doi: 10.1029/2006JB004522.

Kieffer, S. W., Sturtevant, B. (1984) Laboratory Studies of Volcanic Jets. J. Geophys. Res. 89(B10): 8253-8268.

Kilburn, C. R. J., Lopes, R. M. C. (1988) The growth of aa lava flow fields on mount Etna, Sicily. J. Geophys. Res. 93:14759-14771.

Kokelaar, B. P. (1983) The mechanism of Surtseyan volcanism. J. geol. Soc. London. 140: 939-944.

Kokelaar, P. (1986) Magma-water interactions in subaqueous and emergent basaltic volcanism. Bull Volcanol. 48: 275-289.

Kokelaar, P., Busby, C. (1992) Subaqueous Explosive Eruption and Welding of Pyroclastic Deposits. Science. 257(5067): 196-201.

Kokelaar, B. P., Durant, G. P. (1983) The submarine eruption and erosion of Surtla (Surtsey), Iceland. J. Volcanol. Geotherm. Res. 19: 239-246.

Landi, P., Metrich, N., Bertagnini, A., Rosi, M. (2008) Dynamics of magma mixing and degassing recorded in plagioclase at Stromboli (Aelian Archipelago, Italy). Contrib. Mineral. Petrol. 147: 213-227. DOI 10.1007/s00410-004-0555-5.

Lautze, N. C., Houghton, B. (2005) Physical mingling of magma and complex eruption dynamics in the shallow conduit at Stromboli volcano, Italy. Geology. 33(5): 425–428. doi: 10.1130/G21325.1

Lautze, N. C., Houghton, B. (2007), Linking variable explosion style and magma textures during 2002 at Stromboli volcano, Italy. Bull. Volcanol. 69:445-460.

Linneman, S. R., Borgia, A. (1993) The blocky andesitic lava flows of Arenal Volcano, Costa Rica. In: Kilburn CRJ, Luongo G (eds) Active lavas. University College London, London, pp 25–72

Lipman, P. W., Banks, N. G. (1987) Aa flow dynamics, Mauna Loa, 1984. US Geol Surv Prof Pap 1350: 1527–1567

Lupton, J., M. Lilley, D. Butterfield, L. Evans, R. Embley, G. Massoth, B. Christenson, K. Nakamura, and M. Schmidt (2008) Venting of a separate CO_2-rich gas phase from submarine arc volcanoes: Examples from the Mariana and Tonga-Kermadec arcs, J. Geophys. Res. 113, B08S12, doi:10.1029/2007JB005467.

Lyman, A. W., Koenig, E., Fink, J. H. (2004) Predicting yield strengths and effusion rates of lava domes from morphology and underlying topography. J. Volcanol. Geotherm. Res. 129: 125-138.

Lyman, A. W., Kerr, R. C. (2006) Effect of surface solidification on the emplacement of lava flows on a slope. J. Geophys. Res. 111: B05206. doi:10.1029/2005JB004133.

Maicher, D., White, J. (2001) The formation of deep-sea Limu o Pele. Bull. Volcanol. 63: 482-496. doi 10.1007/s004450100165.

Marsella, M., Proietti, C., Sonnessa, A., Coltelli, M., Tommasi, P., Bernardo, E. (2009) The evolution of the Sciara del Fuoco subaerial slope during the 2007 Stromboli eruption: Relation between deformation processes and effusive activity. J. Volcanol. Geotherm. Res., 182: 201–213. doi:10.1016/j.jvolgeores.2009.02.002.

Mastin, L. G. (2007) Generation of fine hydromagmatic ash by growth and disintegration of glassy rinds. J. Geophys. Res., 112, B02203, doi:10.1029/2005JB003883.

Mazzarini, F. M. T., Pareschi, M. T., Favalli, M., Isola, I., Tarquini, S., Boschi, E. (2005) Morphology of basaltic lava channels during the Mt. Etna September 2004 eruption from airborne laser altimeter data. Geophys. Res. Lett. 32: L04305, doi:10.1029/2004GL021815.

Mazzarini, F., Pareschi, M. T., Favalli, M., Isola, I., Tarquini, S., Boschi, E. (2007) Lava flow identification and aging by means of Lidar intensity: The Mt. Etna case. J. Geophys. Res. 112: B02201. doi:10.1029/2005JB004166.

McGetchin, T. R., Settle, M., Chouet, A. (1974) Cinder Cone Growth Modeled After Northeast Crater, Mount Etna, Sicily. J. Geophys. Res. 79(23): 3257-3272.

Mckay, D., Donnelly-Nolan, J. M., Jensen, R. A., Champion, D. E. (2009) The post-Mazama northwest rift zone eruption at Newberry Volcano, Oregon in Volcanoes to vineyards: geologic field trips through the dynamic landscape. (eds) O'Connor JE, Dorsey RJ, Madin I. Geological Society of America, Inc. USA Field Guide 15: 91-110.

McKean, J., Roering, J. (2004) Objective landslide detection and surface morphology mapping using high-resolution airborne laser altimetry Geomorphology 57: 331–351

Metrich, N., Bertagnini, A., Landi, P., Rosi, M. (2001) Crystallization Driven by Decompression and Water Loss at Stromboli Volcano (Aeolian Islands, Italy). J. Petrol. 42(8): 1471-1490.

Moore, G., Carmichael, L. S. (1998) The hydrous phase equilibria (to 3kbar) of an andesite and basaltic andesite from western Mexico; constraints on water content and conditions of phenocryst growth. Contrib Mineral Petrol. 130: 304-319.

Morton, B. R. (1959) Forced Plumes. J. Fluid Mech. 5(1): 151-163.

Naranjo, J. A., Sparks, R. S. J., Stasiuk, M. V., Moreno, M. V., Ablay, G. J. (1992) Morphological, structural and textural variations in the 1988-1990 andesite lava of Lonquimay Volcano, Chile. Geol. Mag. 129(6): 657-678.

Ogden, J., Basher, L., McGlone, M. (1998) Fire, forest regeneration and links with early human habitation: evidence from New Zealand. Annals of Botany. 81: 687-396.

Patrick, M. (2007a) Dynamics of Strombolian ash plumes from thermal video: Motion morphology, and air entrainment. J. Geophys. Res. 112: B06202, doi:10.1029/2006JB004387.

Patrick, M., Harris, A. J. L., Ripepe, M., Dehn, J., Rothery, D. A., Calvari, S. (2007b) Strombolian explosive styles and source conditions: insights from thermal (FLIR) video. Bull. Volcanol. 69: 769-784, doi 10.1007/s00445-006-0107-0.

Perron, J. T., Kirchner, J. W., Dietrich, W. E. (2008) Spectral signatures of characteristic spatial scales and nonfractal structure in landscapes. J. Geophys. Res. 113: F04003. doi: 10.1029/2007JF000866.

Pinkerton, H., Sparks, R. S. J. (1976) The 1975 subterminal lavas, Mount Etna: A case history of the formation of a compound lava field. J. Volcanol. Geotherm. Res. 1: 167-182.

Pinkenon, H., Stevenson, R. J. (1992) Methods of determining the theological properties of magmas at sub-liquidus temperatures. J. Volcanol. Geotherm. Res. 53: 47-66.

Pinkerton, H., Wilson, L. (1994) Factors controlling the lengths of channel-fed lava flows. Bull. Volcanol. 56: 108-120.

Pioli, L., Erlund, E., Johnson, E., Cashman, K., Wallace, P., Rosi, M., Delgado Granados, H. (2008) Explosive dynamics of violent Strombolian eruptions: The eruption of Paricutin Volcano 1943-1952. Earth and Planetary Science Letters. 271: 359–368.

Pyle, D. M., Elliott, J. R. (2006) Quantitative morphology, recent evolution, and future activity of the Kemeni Islands volcano, Santorini, Greece. Geosphere. 2(5): 253-268.

Resing, J. A., Lebon, G., Baker, E. T., Lupton, J. E., Embley, R. E., Massoth, G. J., Chadwick Jr., W. W., de Ronde, C. E. (2007) Venting of Acid-Sulfate Fluids in a High-Sulfidation Setting at NW Rota-1 Submarine Volcano on the Mariana Arc. Economic Geology, 102: 1047-1061.

Roering, J. J., Gerber, M. (2005) Fire and the evolution of steep, soil-mantled landscapes Geology. 33(5): 349–352. doi: 10.1130/G21260.1

Schick, J. D. (1994) Origin of compositional variability of the lavas at Collier Cone, High Cascades, Oregon. Masters Thesis. University of Oregon.

Shaw, A. M., Hauri, E., Tamura, Y., Ishizuka, O., Stern, R., Embley, R. (2006) Volatile Contents of NW Rota Melt Inclusions: Insight to Explosive Submarine Arc Volcanism. Eos Trans. AGU. 87(52), Fall Meet. Suppl., Abstract V52B-05.

Sherrod, D. R., Taylor, E. M., Ferns, M. L., Scott, W. E., Conrey, R. M., Smith, G. A. (2004) Geologic Map of the Bend 30-x 60- Minute Quadrangle, Central Oregon. In Geologic Investigations Series I-2683. USGS. (http://pubs.usgs.gov/imap/i2683/).

Shrestha, R., Carter, W., Slatton, C., Dietrich, W. (2007) "Research-Quality" Airborne Laser Swath Mapping: The Defining Factors. A white paper issued by NCALM. http://www.ncalm.cive.uh.edu/assets/publication_pdf/NCALM_WhitePaper_v1.2.pdf

Slim, A. C., Balmforth, N. J., Craster, R. V., Miller, J. C. (2009) Surface wrinkling of a channelized flow. Proc. R. Soc. A. 465: 123-142. doi:10.1098/rspa.2008.0142.

Smith, J. V., Houston, E. C. (1994) Folds produced by gravity spreading of a banded rhyolite lava flow. J. Volcanol. Geotherm. Res. 63(1-2):89-94.

Taddeucci, J., Pompilio, M., Scarlato, P. (2004) Conduit processes during the July-August 2001 explosive activity of Mt. Etna (Italy): inferences from glass chemistry and crystal size distribution of ash particles. J. Volcanol. Geotherm. Res. 137: 33– 54.

Thorarinsson, S. (1979) On the damage caused by volcanic eruptions with special reference to tephra and gases. In Sheets PD, Grayson DK (eds), Volcanic activity and human ecology. Academic Press, Inc. 125-136.

Valentine, G. A., Gregg, T. K. P. (2008) Continental basaltic volcanoes- Processes and problems. J. Volcanol. Geotherm. Res.177: 857–873.

Venture, G., Vilardo, G. (2008) Emplacement mechanism of gravity flows inferred from high resolution Lidar data: The 1944 Somma-Vesuvius lava flow (Italy). Geomorphology. 95: 223-235.

Wadge, G., Walker, G. P. L., Guest, J. E. (1975) The output of the Etna volcano. Nature 255: 385-387.

Walker, G. P. L. (1971) Compound and simple lava flows and flood basalts. Bull. Volcanol. 35: 579-590.

Walker, G. P., Croasdale, R. (1971) Characteristics of Some Basaltic Pyroclastics. Bull. Volcanol. 35: 303-317.

Walker, G. P. (1973) Explosive volcanic eruptions- a new classification scheme. Geologische Rundschau. 62(2): 431-446.

Walker, G. P. L. (1973) Lengths of lava flows. Philosophical Transactions of the Royal Society, ser. A, 274: 107-118.

Walker, S. L., E. T. Baker, J. A. Resing, W. W. Chadwick Jr., G. T. Lebon, J. E. Lupton, and S. G. Merle (2008), Eruption-fed particle plumes and volcaniclastic deposits at a submarine volcano: NW Rota-1, Mariana Arc, J. Geophys. Res. 113: B08S11, doi:10.1029/2007JB005441.

Webster, J. D., Kinzler, R. J., Mathez, E. A. (1999) Chloride and water solubility in basalt and andesite melts and implicationsfor magmatic degassing. Geochimica et Cosmochimica Acta. 63(5): 729–738.

White, J. D. L. (2001) Eruption and reshaping of Pahvant Butte volcano in Pleistocene Lake Bonneville. Spec. Publs. Int. Ass. Sediment. 30: 61-80.

Wilson, L., Self, S. (1980) Volcanic explosion clouds: Density, temperature and particle content estimates from cloud motion. J. Geophys. Res. 85: 2567-2572.

Wohletz, K. (1983) Mechanisms of hydrovolcanic pyroclast formation: grain-size, scanning electron microscopy, and experimental studies. 1983. J. Volcanol. Geotherm. Res. 17: 31-63.

Wohletz, K., McQueen, R. (1984) Experimental Studies of Hydromagmatic Volcanism. In Explosive Volcanism: Inception, Evolution, and Hazards. 158-169.

Wohletz, K. (1986) Explosive magma-water interactions: Thermodynamics, explosion mechanisms, and field studies. Bull. Volcanol. 48: 245-264.

Woods, A. W., (1998) Observations and models of volcanic eruption columns. In: Gilbert, J., Sparks, R. (ed) The Physics of Explosive Volcanic Eruptions, The Geological Society, London, Special Publictions, pp 91-114.

Woolard, J. W., Colby, J. D. (2002) Spatial characterization, resolution, and volumetric change of coastal dunes using airborne LIDAR: Cape Hatteras, North Carolina Geomorphology 48:269–287.

Yuasa, M., Kano, K. (2003) Submarine Silicic Calderas on the Northern Shichito-Iwojima Ridge, Izu-Ogasawara (Bonin) Arc, Western Pacific. In: White, J., Smellie, J., Clague, D. (ed) Explosive Subaqueous Volcanism, Geophysical Monograph 140, AGU, Washington, DC, pp 231-243.